University of Alberta

Drag Reduction in Vertical Annular Air-Water Flow

by

Maria Gabriela Rodriguez

A thesis submitted to the Faculty of Graduate Studies and Research in partial fulfillment of the requirements for the degree of Master of Science

Department of Mechanical Engineering

Edmonton, Alberta
Fall 2004

In compliance with the
Canadian Privacy Legislation
some supporting forms
may have been removed from
this dissertation.

While these forms may be included
in the document page count,
their removal does not represent
any loss of content from the dissertation.

0-612-95843-8

To my Parents.

ACKNOWLEDGEMENTS

I would like to note my appreciation to those people who stand out most notably in my mind as I write these lines.

There is a special mentor that I want to acknowledge due to his importance in my work. Thank you Dr. Brian Fleck for your untiring support and seemingly unlimited belief in me.

To Dr. Richard Fernandes, I will always be grateful to you and your inspiring research and ideas.

I would also like to thank Dr. Theodore Heidrick, for your helpful suggestions and continuing support.

Special thanks to the Mechanical Engineering machinists and technicians for their priceless assistance, especially to Bernie Faulkner, Ian Buttar, Andrew Coward, Rick Bubenko, Terry Nord and Tuula Hilvo.

Finally, to my family and friends, whose steadfast love and support encouraged me to lift my spirit in the hardest of times. I will forever be indebted to you.

CONTENTS

1 Introduction **1**

1.1 Annular Dispersed Flow 1

1.2 Drag Reduction 2

1.2.1 Proposed Mechanisms for Drag Reduction 4

1.2.2 DRA Applications 6

1.2.3 Previous research work on drag reduction with additives in annular gas-liquid flow 8

1.3 Objectives of the Research Work 11

2 Equipment and Procedure **14**

2.1 Vertical Two-Phase Flow Facility 14

2.2 Systems and Test Conditions 18

2.3 Air-Water System 19

2.3.1 Pressure Measurements 19

2.3.2 Holdup Measurement 21

2.4 Air-Water-Polymer System 22

2.4.1 Solution Preparation 23

2.4.2 Viscosity Measurements 23

3 Implementation of an Annular Dispersed Flow Model **26**

3.1 Two-Phase Flow Parameters 26

3.1.1 Superficial Velocities 27

3.1.2 Volume Fraction 28
3.1.3 Holdup and Actual Phase Velocities 29
3.1.4 Friction Factor 30
3.1.5 Reynolds and Densimetric Froude Numbers 31
3.2 Assumptions 32
3.3 The Pressure Gradient in the Model 34
3.4 Model Equations 37
3.4.1 Film and Core Velocities 38
3.4.2 Holdup 38
3.4.3 Core Holdup 39
3.4.4 Core Density and Viscosity 40
3.4.5 Wall Shear Stress 40
3.5 Calculation Methodology 42
4 Model Results **46**
4.1 Effect of Polymer Concentration on the Drag Reduction 46
4.2 Effect of System Parameters on the Flow Characteristics 52
4.2.1 Effect on Liquid Distribution 52
4.2.2 Effect on the Holdup 60
4.2.3 Effect on the Pressure Gradient 65
4.2.4 Friction Factors 80
4.3 Uncertainty Considerations 84
4.4 Repeatability Tests 86
4.5 DRA Polymer Degradation 91

5 Conclusion **95**

5.1 Conclusions 95

5.2 Recommendations 97

Bibliography **99**

A. Appendix: Data Analysis **103**

A.1 Spectral Analysis 103

A.2 Calculation of the Air Flow Rate 106

A.3 Calculation of the Liquid Flow Rate 112

A.4 Single Phase Test 114

B. Appendix: Equipment and Instrumentation **117**

C. Appendix: Test Conditions and Fluid Properties **121**

C.1 Test Conditions 121

C.2 Physical Properties of the Fluid Systems 121

C.2.1 Density 122

C.2.2 Surface Tension 123

C.2.3 Viscosity 124

D. Appendix: Uncertainty Analysis **131**

D.1 Equations 140

LIST OF TABLES

Table 4.1: Summary of the results obtained at gas and liquid flow rates of 43.3 g/s and 145 g/s respectively and various polymer concentrations 50

Table 4.2: Summary of the results obtained at gas and liquid flow rates of 33.8 g/s and 145 g/s respectively and various polymer concentrations 51

Table 4.3: Uncertainty in the drag reduction by perturbation of the liquid holdup and pressure gradient for gas and liquid flow rates of 17.3 g/s and 148 g/s respectively 85

Table 4.4: Uncertainty in the drag reduction by perturbation of the liquid holdup and pressure gradient for gas and liquid flow rates of 42.9 g/s and 148 g/s respectively 85

Table 4.5: Summary of the repeatability tests for a polymer concentration of 100 ppm 88

Table 4.6: Summary of the repeatability tests for a polymer concentration of 120 ppm 89

Table A.1: Sample data and calculated flow rate for an air test at the maximum upstream pressure 111

Table A.2: Annubar calibration data 112

Table B.1: Equipment specifications 117

Table B.2: Range of viscosities for a spindle CP-40 119

Table C.1: Experimental conditions..... 121

Table C.2: Properties of the fluids used at 20°C 122

Table C.3: Surface tension of the polymer solution at standard conditions..... 124

Table D.1: Uncertainty in the calculated parameters by perturbation of the liquid holdup for air and water at flow rates of 17.3 g/s and 148 g/s respectively 132

Table D.2: Uncertainty in the calculated parameters by perturbation of the liquid holdup for air and polymer solution at flow rates of 17.3 g/s and 148 g/s respectively 133

Table D.3: Uncertainty in the calculated parameters by perturbation of the pressure gradient for air and water at flow rates of 17.3 g/s and 148 g/s respectively 134

Table D.4: Uncertainty in the calculated parameters by perturbation of the pressure gradient for air and polymer solution at flow rates of 17.3 g/s and 148 g/s respectively 135

Table D.5: Uncertainty in the calculated parameters by perturbation of the liquid holdup for air and water at flow rates of 42.9 g/s and 148 g/s respectively 136

Table D.6: Uncertainty in the calculated parameters by perturbation of the liquid holdup for air and polymer solution at flow rates of 42.9 g/s and 148 g/s respectively 137

Table D.7: Uncertainty in the calculated parameters by perturbation of the pressure gradient for air and water at flow rates of 42.9 g/s and 148 g/s respectively 138

Table D.8: Uncertainty in the calculated parameters by perturbation of the pressure gradient for air and polymer solution at flow rates of 42.9 g/s and 148 g/s respectively 139

LIST OF FIGURES

Figure 1.1: The flow of a gas and a liquid in an Annular Dispersed Flow Pattern 1

Figure 2.1: Schematic of the Test Facility 17

Figure 2.2: Viscosity μ as a function of the shear rate γ for polymer concentrations of 30 to 140 ppm 25

Figure 3.1: Flow regime map for +90° co-current vertical air/water flow in a 0.026 m I.D. pipe (Spedding et al., 2001) 28

Figure 3.2: Physical Model for Annular Flow 34

Figure 3.3: Schematic of calculation procedure to estimate drag reduction 45

Figure 4.1: Variation of drag reduction with polymer concentration at a liquid mass flow rate of 145 g/s 47

Figure 4.2: Liquid entrained fraction E as a function of superficial gas Reynolds number Re_{sg} and superficial liquid velocity U_{sl} for air-water only 54

Figure 4.3: A comparison between entrained fraction estimated by the present approach and the predicted values using the correlations of Wallis (1969) and Ishii and Mishima (1989) 56

Figure 4.4: Film thickness d as a function of superficial gas Reynolds number Re_{sg} at various gas and liquid superficial velocities 59

Figure 4.5: Measured values of liquid holdup α_l as a function of the superficial gas Reynolds number Re_{sg} at various gas and liquid superficial velocities 62

Figure 4.6: A comparison between the measured values of liquid holdup α_{exp} and the calculated values using Spedding's correlation $\alpha_{Spedding}$, for air-water only 64

Figure 4.7: Two-phase pressure drop for air-water vertical flow at a superficial liquid velocity of 0.294 m/s and various superficial gas velocities 65

Figure 4.8: Two-phase pressure drop for air-water vertical flow at a superficial liquid velocity of 0.417 m/s and various superficial gas velocities 66

Figure 4.9: Two-phase pressure drop for air-water vertical flow at a superficial liquid velocity of 0.552 m/s and various superficial gas velocities 67

Figure 4.10: Two-phase pressure drop for air-water-polymer system at a superficial liquid velocity of 0.294 m/s and various superficial gas velocities 70

Figure 4.11: Two-phase pressure drop for air-water-polymer system at a superficial liquid velocity of 0.417 m/s and various superficial gas velocities 71

Figure 4.12: Two-phase pressure drop for air-water-polymer system at a superficial liquid velocity of 0.552 m/s and various superficial gas velocities 72

Figure 4.13: Effect of DRA on the frictional pressure gradient at various gas and liquid flow rates 74

Figure 4.14: Effect of DRA on the hydrostatic pressure gradient at various gas and liquid flow rates 75

Figure 4.15: Variation of the measured pressure P_6 with the gas flow rate 77

Figure 4.16: Variation of the measured pressures with the gas flow rate at a superficial liquid velocity of 0.294 m/s 78

Figure 4.17: Variation of the measured pressures with the gas flow rate at a superficial liquid velocity of 0.552 m/s 79

Figure 4.18: Comparison of friction factors obtained for the air-water system and air-water-polymer system 82

Figure 4.19: Effectiveness of DRA at various gas and liquid flow rates 83

Figure 4.20: Schematic of the gas-liquid separator 90

Figure 4.21: Ratio of the overall pressure gradients with and without DRA as a function of time for a polymer concentration of 60 ppm 92
Figure 4.22: Mechanism of operation of a rotary vane pump 94
Figure A.1: Power spectrum corresponding to the recorded pressure signal P_1 when only air was flowing along the pipe at a rate of 122 g/s 105
Figure A.2: Power spectrum corresponding to the recorded pressure signal P_1 at static conditions 106
Figure A.3: Calibration curve of the liquid flow meter 113
Figure A.4: Pressure as a function of the position along the pipe 115
Figure B.1: Detailed drawing of the gas-liquid separator provided the manufacturer 120
Figure C.1: Viscosity μ as a function of the shear rate γ for two samples taken from different batches of polymer solution at a concentration of 30 ppm 125
Figure C.2: Viscosity μ as a function of the shear rate γ for two samples taken from different batches of polymer solution at a concentration of 50 ppm 126
Figure C.3: Viscosity μ as a function of the shear rate γ for two samples taken from different batches of polymer solution at a concentration of 75 ppm 127

Figure C.4: Viscosity μ as a function of the shear rate γ for two samples taken from different batches of polymer solution at a concentration of 100 ppm 128

Figure C.5: Viscosity μ as a function of the shear rate γ for two samples taken from different batches of polymer solution at a concentration of 120 ppm 129

Figure C.6: Viscosity μ as a function of the shear rate γ for two samples taken from different batches of polymer solution at a concentration of 140 ppm 130

NOMENCLATURE

Latin Symbols

A ..... Pipe cross-sectional area

a ..... Coefficient in Churchill correlation of Fanning friction factor

A_c ..... Cross-sectional area of the core

Acc ..... Acceleration component of the pressure gradient

A_f ..... Cross-sectional area of the film

A_g ..... Cross-sectional area occupied by the gas phase

a_k ..... Set of complex coefficients in Discrete Fourier Transform Equation

A_l ..... Cross-sectional area occupied by the liquid phase

A_t ..... Cross-sectional area of the throat in a Bernoulli obstruction meter

b ..... Coefficient in Churchill correlation of Fanning friction factor

C_d ..... Dimensionless discharge coefficient of a Bernoulli obstruction meter

D ..... Pipe diameter

d ..... Film thickness

D_f ..... Film hydraulic diameter

dP/dx ..... Pressure gradient

$(dP/dx)_{withDRA}$ ..... Frictional pressure gradient with DRA

$(dP/dx)_{withoutDRA}$ ..... Frictional pressure gradient without DRA

dS ..... Surface differential

d_t ..... Throat diameter in a Bernoulli obstruction meter

dV ..... Volume differential

E ..... Entrainment fraction

f ..... Fanning friction factor

f_f ..... Film Fanning friction factor

F_g ..... Densimetric gas Froude number

F_i ..... Body force per unit mass in the i-direction Momentum Equation

F_l ..... Densimetric liquid Froude number

Fr ..... Frictional component of the pressure gradient

f_s ..... Sample frequency in Discrete Fourier Transform Equation

$f_{withDRA}$ ..... Fanning friction factor with DRA

$f_{withoutDRA}$ ..... Fanning friction factor without DRA

F_1 ..... Constant in the Discharge Coefficient Equation

F_2 ..... Constant in the Discharge Coefficient Equation

g ..... Gravitational acceleration

Hyd ..... Hydrostatic component of the pressure gradient

j ..... Imaginary number

k ..... Index counter in Discrete Fourier Transform Equation

L ..... Pipe length

$\dot{m}_g$ ..... Gas mass flow rate

$\dot{m}_l$ ..... Liquid mass flow rate

N ..... Total number of samples in Discrete Fourier Transform

n_j ..... Unit normal vector

P ..... Pressure

P_{diff} ..... Differential pressure across the orifice plate

P_{down} ..... Pressure downstream the orifice plate

P_t ..... Thermodynamic pressure

P_{up} ..... Pressure upstream the orifice plate

P_1 ..... Pressure measured by the first pressure transducer located at the bottom of the test section

P_2 ..... Pressure measured by the second pressure transducer

P_3 ..... Pressure measured by the third pressure transducer

P_4 ..... Pressure measured by the fourth pressure transducer.

P_5 ..... Pressure measured by the fifth pressure transducer

P_6 ..... Pressure measured by the sixth pressure transducer located at the top of the test section

Q ..... Volumetric Flow Rate

Q_g ..... Volumetric Gas Flow Rate

Q_l ..... Volumetric Liquid Flow Rate

R ..... Gas Constant

Re ..... Reynolds number

Re_f ..... Film Reynolds number

R_i ..... Surface force per unit area in the i-direction Momentum Equation

Re_{sg} ..... Superficial gas Reynolds number

Re_{sl} ..... Superficial liquid Reynolds number

S ..... Pipe perimeter

S_f ..... Film perimeter

T ..... Temperature

T_{ji} ..... Stress tensor

U ..... Fluid velocity

U_f ..... Average film velocity

U_g ..... Actual gas velocity

U_i ..... Average velocity in the i-direction

U_j ..... Average velocity in the j-direction

U_l ..... Actual liquid velocity

U_s ..... Superficial velocity

U_{sc} ..... Superficial core velocity

U_{sf} ..... Superficial film velocity

U_{sg} ..... Superficial gas velocity

U_{sl} ..... Superficial liquid velocity

U_{sle} ..... Superficial velocity of the liquid entrained

We_g ..... Gas Weber number

Greek Symbols

α_c ..... Core Holdup

α_f ..... Film holdup

α_g ..... Gas Holdup

α_l ..... Liquid Holdup

β ..... Ratio of diameters for a Bernoulli obstruction meter

$\Delta\rho$ ..... Density difference between liquid and gas

δ_{ji} ..... Kronecker delta, also know as substitution tensor or identity tensor

ε ..... Pipe roughness

γ ..... Shear rate

λ_c ..... Core volume fraction

λ_g ..... Gas volume fraction

λ_l ..... Liquid volume fraction

μ ..... Dynamic fluid viscosity

μ_c ..... Dynamic core viscosity

μ_g ..... Dynamic gas Viscosity

μ_l ..... Dynamic liquid viscosity

ρ ..... Fluid density

ρ_c ..... Core density

ρ_g ..... Gas density

ρ_l ..... Liquid density

σ ..... Surface tension

τ_i ..... Shear stress at the gas-liquid interface

τ_{ji} ..... Viscous stress tensor

τ_w ..... Wall shear stress

Acronyms

CDR ..... Conoco Drag Reducer

CS ..... Control surface

CV ..... Control volume

DR ..... Drag Reduction

DRA ..... Drag Reducing Additive

DRAs ..... Drag Reducing Additives

I.D. ..... Inside diameter

ppm..... Parts per million

TAPS..... Trans Alaska Pipeline System

1 Introduction

1.1 Annular Dispersed Flow

Annular dispersed flow is a two-phase flow regime in which the liquid flows partly in a film along the inner wall of the pipe and partly as droplets carried by the gas flowing in the center of the pipe. A sketch of this type of flow is shown in Figure 1.1.

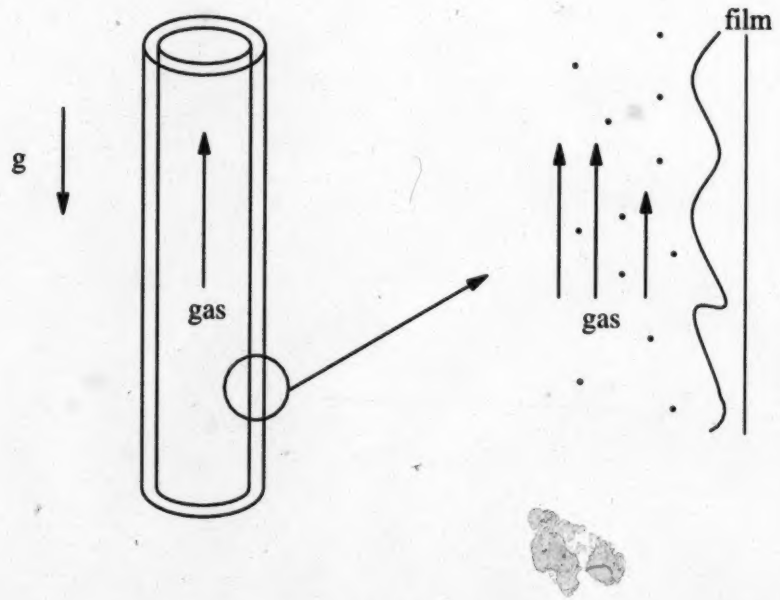

Figure 1.1: The flow of a gas and a liquid in an Annular Dispersed Flow pattern.

This two-phase flow pattern is of importance in the production as well as transportation of gas/condensate and gas/oil systems. It is frequently encountered in risers connected to horizontal flow lines and in gas wells where condensation occurs as a combination of high pressure and low temperature along the well tubing.

In an annular dispersed flow, droplets are continuously being entrained into the core of the flow from the liquid film. The entrained droplets are accelerated by the gas and after some time are deposited onto the liquid film again. This accelerating process leads to a net transport of momentum from the gas to the liquid and therefore results in an additional source of pressure drop. As it will be shown in Section 3, this is generally the most important mechanism of pressure drop in an annular dispersed flow.

1.2 Drag Reduction

Drag reduction (DR) can be defined as a decrease in the frictional pressure drop in a given system at a given flow rate. It is usually produced by the addition of a high molecular weight polymer (approximately $10^6 - 10^7$ kg/kmol) to the fluid in a system.

Potential use of Drag Reducing Additives (DRAs) in multiphase pipelines has a considerable interest in the oil and gas industry. In multiphase production systems, the distance from the wellhead to the gas-liquid separator is typically about 10 – 30 km, but can be as much as 100 km. The pressure drop in these pipelines increases significantly with the presence of condensate; as a result, a significant back pressure is often imposed on the wells and their production rate decreases. Consequently, there is a considerable interest in the possibility of increasing the capacity of new and existing pipeline systems without the need to replace sections of pipe or provide additional pumping power.

Particularly problematic are gas-condensate production systems that operate in the annular dispersed flow regime. Due to high gas velocities associated with annular dispersed flows, such systems generally have very high pressure drops. Pressure gradients are typically in the range of 0.5 – 4 bar/km, resulting in pressure drops typically between 20 – 80 bars.

The effect of DRAs has been widely investigated in single phase systems and many experimental data have been published; in contrast, the effect of DRAs in multiphase systems has received relatively little attention. Until the mid 1990s only a small number of minor investigations into the use of DRAs in multiphase flow were published. However several recent, large-scale studies of DRAs in multiphase oil-gas pipelines have demonstrated significant drag reduction effects,

so that these applications are likely to be increasingly common in the hydrocarbon industry.

1.2.1 Proposed Mechanisms for Drag Reduction

Although the drag reduction effect of polymers has been known for almost half a century, a generally accepted explanation of the mechanism that causes this drag reduction is still not available.

Manfield et al. (1999) presented a survey of the published literature concerning drag reduction with additives. In this review some proposed mechanisms for the drag reduction phenomenon in single phase flow were cited.

Lumley's work was mentioned as one of the most thorough literature reviews of the dynamics of polymer molecules in turbulent flows. In this work it was reported that drag reducing polymer molecules in turbulent boundary layers are stretched by the flow, resulting in an increase in the total increase in the local fluid viscosity.

Little et al. proposed that the DRA molecules are most active in the "buffer zone" located between the viscous sublayer near to the pipe wall and the turbulent core at its centre.

Manfield et al. (1999) also referred to other authors who have suggested explanations for the drag reduction phenomenon based on the elasticity of the DRA macromolecules. Sellin et al. and Wilson support the view that the DRA molecules become extended in turbulent flow, in regions of high elongational strain. According to Sellin et al., this explains why the drag reduction phenomenon is not observed in laminar flow, which has none of these regions and where the flow is wholly rotational.

In addition, in this literature review (Manfield et al., 1999) it was mentioned that, according to recent works on turbulence, turbulent eddies begin in the near wall region as "streaks", which periodically rise up through the buffer zone and are eventually ejected as "bursts" into the turbulent core. It is this bursting process which wastes energy in the flowing system. It is suggested that DRA molecules somehow interfere with the bursting process and reduce the degree of turbulent transfer to the core. Promotional literature for a commercial DRA suggests that as the DRA molecules are elongated in the buffer zone, they somehow absorb energy from the streaks and thereby reduce the frequency of bursts into the turbulent core.

Most recently, Xueming and Janzhong (2002) claimed that polymer additives do not simply suppress the turbulent fluctuation. From measurements of turbulent intensities and Reynolds stresses, they found that the axial turbulence intensity

increased while the radial turbulence intensity decreased. They concluded that the turbulence structures are changed rather than suppressed.

1.2.2 DRA applications

The use of drag reducers in the oil industry has been primarily limited to hydraulic fracturing operations. These fracturing processes are facilitated by pumping a fracturing fluid into a well and applying a high pressure in order to fracture the surrounding rock, thus stimulating the flow of the petroleum product. Sand grains or other granular substances, called proppants, are also injected into the formation to bridge the gap formed by fracturing and to keep it open when the pressure on the fracturing fluid is reduced. The fracturing fluid contains also a number of additives to maintain stability and to allow for easy recovery of the fluid for clean up. These additives include friction reducers which are usually water soluble polymers of high molecular weight that have been proved to be effective in reducing hydraulic horsepower requirements and/or increasing pump rates during fracturing treatments. Many water gels used to improve the sand-carrying capacity of the fracturing fluid have excellent drag reduction properties. Oil-soluble polymers have been used to a lesser extent in hydraulic fracturing with oil-base fluids.

Drag reducers have not been routinely used in standard crude oil pipeline operations. The first large-scale application of a DRA in an oil pipeline began during 1979 in the Trans Alaska Pipeline System (TAPS). The Conoco drag reducer CDR proved to be effective at low concentrations in operating pipelines with diameters of 8, 12 and 48 inches. By 1980 flow through the TAPS line had increased to the 1.5 million bbl/day level. Approximately 200,000 bbl/day of this throughput was a direct result of injecting a drag reducing additive. Drag reduction was found to be an excellent temporary alternative to constructing pump stations for increasing the flow rate in TAPS.

The application of DRAs in the field involves some technical and economic aspects. Burger et al. (1980) pointed out three special requirements a drag reducer must meet in commercial operations:

1. The drag reducing additive must be effective at low concentrations. Continuous use in pipeline operations requires that the polymer be injected continuously. Relatively large amounts of chemical additives are required even at low concentrations.

2. The drag reducer must be relatively shear stable during the flow. DRAs are easily degraded by shear stresses raised from centrifugal pumps and most positive displacement pumps. To avoid degradation, the polymer

should be injected in a concentrated form downstream of the pipeline booster pumps. The drag reducer must also maintain its effectiveness as the fluid moves down the pipeline between booster pump stations.

3. The treated crude must not cause downstream refining problems.

1.2.3 Previous research work on drag reduction with additives in annular gas-liquid flow

Although there have been numerous studies of drag reduction in pipe flow of polymer solutions, only few of them have been done in two-phase gas-liquid annular flow.

The first study of drag reduction in the annular mist regime was carried out by Sylvester and Brill (1976). Pressure drop data were taken for horizontal flow of air and water in a 1.27 cm diameter pipe and a length of 6.1 m, at a system pressure of approximately 6.895×10^5 Pa. The liquid-gas ratio was varied from 56.2 to 5620 m^3 of liquid per million standard cubic meter of gas. A polymer solution with 100 ppm of polyethylene oxide contained in a holding tank was pumped to a tee where it was mixed with the gas. The existence of drag reduction in two-phase, annular-mist flow was demonstrated. Pressure gradient

reductions up to 37% were obtained. However, no explanation for these changes was given.

Al-Sarkhi and Hanratty (2001a) examined the influence of Percol 727 (a co-polymer of polyacrylamide and sodium-acrylate) on an annular flow of air and water in a horizontal pipe with a diameter of 9.53 cm. Unlike previous studies, the polymer solution was not circulated with a pump. Instead, a concentrated solution contained in a pressurized container was injected into the system. Gas and liquid superficial velocities of 30 – 43 m/s and 0.03 – 0.09 m/s were used. It was found that the annular flow regime changed to a stratified pattern at large drag reductions. A drag reduction as high as 48% was achieved with a concentration in the liquid in the pipe of only 10 ppm. In general, the drag reduction increased with increasing the superficial liquid velocity and decreased with increasing the superficial gas velocity. It was also noted that drag reduction increases with increasing concentration and eventually reaches a plateau. Lower concentrations were needed to initiate drag reduction and to reach maximum effectiveness.

From the results of visual observations, the previous authors (Al-Sarkhi and Hanratty, 2001a) argued that the polymers destroyed the turbulent disturbance waves which were the cause of drop formation. At maximum drag reductions the

friction factor was found to be roughly equal to that which would characterize gas flowing alone in the pipe.

In a subsequent study (Al-Sarkhi and Hanratty, 2001b), they investigated the effect of scaling by using a horizontal pipe with a smaller diameter of 2.54 cm. Higher drag reductions of up to 63% were realized. A larger concentration of polymer of about 30 ppm was also needed to obtain maximum drag reduction. The flow pattern at maximum drag reduction was usually a stratified flow. However, an unexpected finding was that at higher gas velocities the top wall remained wetted with a thin film that has capillary waves. This was described by Al-Sarkhi and Hanratty as a stratified-annular flow or as an annular flow with no disturbance waves.

Measurements of droplet concentrations in the gas phase and of the thickness of the wall liquid layer were also presented. An entrainment, E, defined as the ratio of the flow rate of liquid drops to the total liquid flow, was obtained to be 0.36, 0.39 and 0.39 for superficial liquid velocities of 0.041, 0.62 and 0.125 m/s, respectively, and a superficial gas velocity of 52 m/s. After the addition of polymer, the measured flow of the wall film was roughly equal to the liquid flow into pipe. The differences were within the experimental error. Since the addition of polymers greatly reduced entrainment, film thickness was larger than for the annular flow of gas and water only.

1.3 Objectives of the Research Work

The main purpose of this research work was to experimentally test a commercially available drag reducing polymer for application in vertical annular air-water flows.

Published work on drag reduction with additives in two-phase flow has been almost exclusively confined to horizontal pipe flow. Attention to vertical upward flow is required in order to step forwards the feasibility of applying drag reducing polymers in multiphase systems such as gas-condensate vertical wells and vertical flowlines.

Based on prior work with drag reducing additives and, particularly, with Percol 727 drag reducer, the specific objectives of this study include the following:

1. To investigate the effects of polymer concentration on drag reduction, experiments of drag reduction were performed at various concentrations. The results were used to determine the optimum concentration of polymer for reducing drag under the flow conditions considered in this particular study.

2. This study was carried out with the aim of not only presenting the results of proof-of-concept laboratory experiments, but also identifying the influence of the polymer on the characteristics of the flow. To achieve this, drag reduction experiments were carried out over a range of gas and liquid flow rates observed to produce annular flow. The results of these tests were then analyzed and compared to give further insight into the drag reduction phenomenon.

3. Another important objective of this study was to examine the key features of drag reduction quantitatively and attempt to ascertain the relative contributions of the two-phase flow mechanisms to the overall drag reduction. To obtain this, a model developed for annular flow was considered and used to calculate the magnitude of the hydrostatic, frictional and acceleration contributions to the pressure gradient.

4. In addition, some tests were conducted closed-loop in order to get a sense of the time dependent effectiveness of the drag reducing polymer.

Detailed description of the apparatus used and the experimental procedure employed are presented in Section 2. The model equations for annular dispersed flow are introduced in Section 3. Experimental and model results are then

presented in Section 4. Finally, in Section 5 conclusions are drawn and suggestions for further work are made.

2 Equipment and Procedure

2.1 Vertical Two-Phase Flow Facility

The experimental apparatus is shown schematically in Figure 2.1. This apparatus was constructed in an open shaft at the Mechanical Engineering Building of the University of Alberta. The system was designed such that the variables that were controlled would be the air and water flow rates.

The air was supplied by a central compressed air source at the experimental site. The air feed line contained an orifice plate and a pressure regulator which allowed adjustment of the inlet pressure in order to obtain the desired air flow rate. The orifice meter monitored the upstream and the differential pressure across the plate to provide an accurate and continuous air flow measurement. The maximum upstream pressure was generally 552 kPa.

Water was pumped from a storage tank by a moving vane positive displacement pump. The pump was driven by a variable speed motor which allowed the water flow rate control. An Annubar DNT/10S was used to measure the liquid flow rate within the water line. This device has Pitot tubes that sense the impact or stagnation and the static pressure; hence, the liquid flow rate was calculated from the difference between the stagnation pressure and the static pressure of the fluid.

The calibration curve of the liquid flow meter is given in Appendix A; the maximum water delivery was 0.25 kg/s.

The pressure taps of the flow meters were connected to Validyne pressure transducers which were wired to individual Validyne demodulators and their outputs were recorded on a PC-based data acquisition system.

The air and water were combined in a tee section. All tubing following the mixing tee was constructed of clear polycarbonate with an inside diameter of 2.54 cm and mounted vertically. A flow development section of approximately 390 tube diameters was provided between the mixing tee and the test section in order for the flow to fully develop. The test section was 12.2 m long and contained six pressure transducers placed 2.44 m apart. These were Omega PX603 gauge pressure transducers with a full scale range of 690 kPa. The signals were monitored and recorded on the PC-based data acquisition system.

Each section of the riser was flanged, gasketted and bolted together so as to ensure minimal interference to the internal flow. At the end of the test section the gas and liquid were separated by means of a gas-liquid separator.

Specifications of the experimental equipment and instrumentation can be found in Appendix B. The apparatus was evaluated by measuring pressure drop data

for single phase air flow. The friction factor calculated from pressure drop measurements was compared to the value obtained from the Moody chart for smooth pipes. The comparison was good with an average deviation of 5%. Calculations are given in Appendix A.

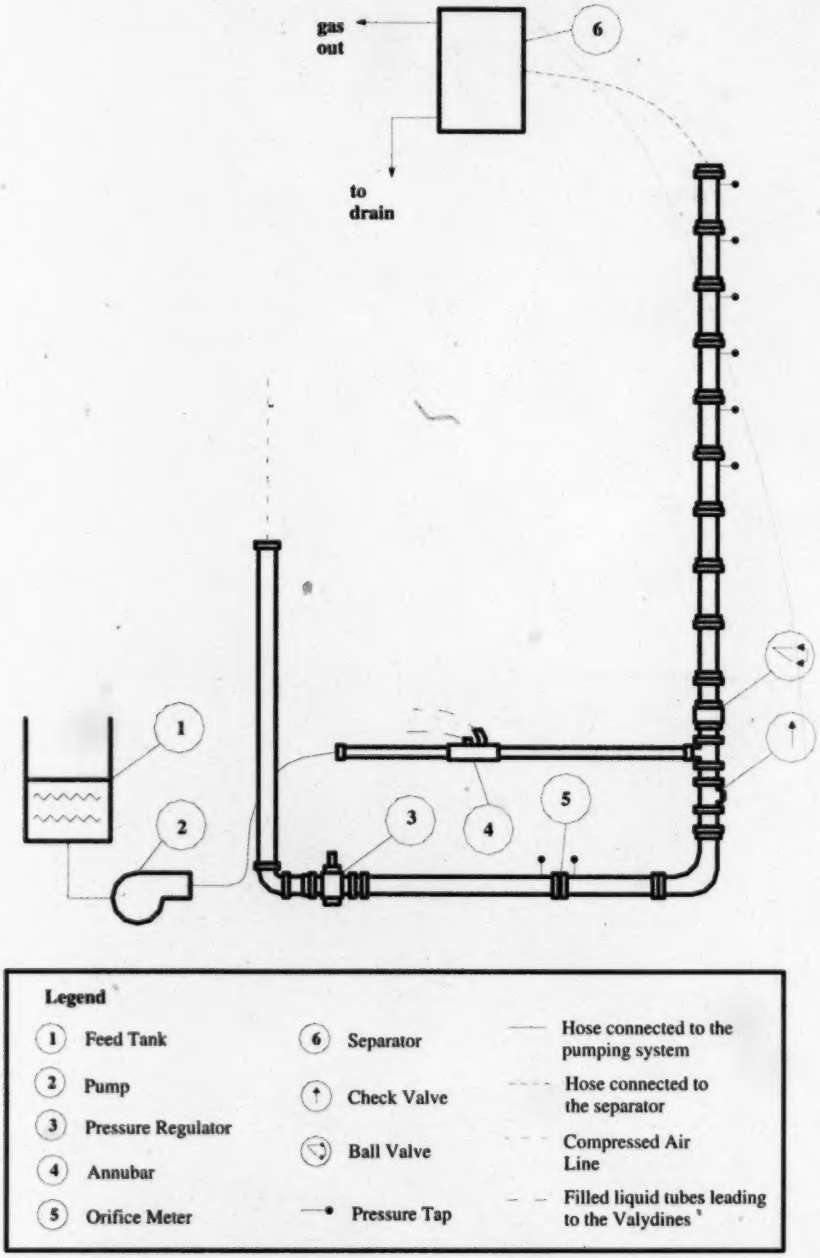

Figure 2.1: Schematic of the Test Facility (not to scale)

2.2 Systems and Test Conditions

Experiments were carried out with an air-water and air-polymer solution system flowing through the vertical pipe. Liquid mass flow rates of 148 g/s, 210 g/s, 278 g/s and air flow rates ranging from 14.2 g/s to 46.3 g/s were used.

The liquid mass flow rates correspond to superficial liquid velocities of 0.294 m/s, 0.417 m/s and 0.552 m/s. Similarly, the experiments covered a range of superficial gas velocities from 8.58 m/s to 20.1 m/s. All the measurements were taken in the annular flow regime.

The experiments were conducted using line pressures (upstream in the test section) between 200 kPa – 576 kPa. The inlet temperature was 20°C ± 2°C. The air density was calculated by using the ideal gas law. Since the dynamic viscosity of a fluid varies only weakly with pressure, the viscosities of the air and water were taken as the tabulated values at standard pressure and temperature. Similarly, the surface tension for the air-water system was not measured but taken to be the tabulated value at standard conditions. In contrast, for the air-polymer solution system, the use of the polymer solution viscosity was complicated because polyacrylamide solutions are non-Newtonian and are sensitive to ionic strength. Polymer solutions are pseudoplastic which means that the viscosity of a polymer solution decreases with increasing stress. Indications

of a pseudoplastic behavior were obtained by simple measurements of viscosity at different shear rates. The rheological behavior of the polymer solution is given in Figure 2.2. The experimental conditions and properties of the fluid systems are also summarized in Appendix C. The viscosity of all the solutions showed shear thinning behavior up to a shear rate of 90 sec^{-1}; no sudden decrease in viscosity was observed beyond 90 sec^{-1} where the viscosity of the polymer solution remained similar to that one of water ($1x10^{-3}$ Ns/m^2) for solutions with 30 and 50 ppm. For larger concentrations, the viscosity for a given shear rate increased with increasing polymer concentration.

2.3 Air-Water System

Measurements with air and water were used to select the flow rates for the tests with the polymer solution and as a baseline to estimate later the relative reduction in the drag.

2.3.1 Pressure Measurements

An experimental run was started by passing a given flow rate of dry air through the system to check for the proper operation of the six pressure transducers. Water at a given flow rate was then admitted to the system and the inlet pressure was adjusted to obtain the desired air flow rate. All pressure and flow rate

measurements were then made. Enough time was given for the system to reach steady state; the initial unsteady set-up time for the flow was approximately 6 min. Steady state was defined to be reached when changes in flow parameters varied by less than 0.5% over 25 min approximately.

The measured pressure signals contained some random and periodic variations or random error observed in the time domain. A spectral analysis, using discrete Fourier transform, was first performed in order to detect the possible characteristic frequency of the noise not evident in time domain. The signal was expressed as a sum of sine and cosine waves, as follows:

$$P(t_n)=\frac{1}{N}\sum_{k=0}^{N-1} a_k e^{\frac{2\pi k f_s t_n}{N} j} \tag{2.1}$$

where:

$P(t_n)$ is the set of regularly spaced pressure samples taken at times t_n (real numbers).

N is the total number of samples (chosen such that $N=2^m$ where m is some positive integer, thus allowing for "fast" transformation).

k is the index counter where $k = 0, 1, 2, \ldots N\text{-}1$

a_k is the set of complex coefficients.

f_s is the sample frequency (Hz)

$j = \sqrt{-1}$

The spectrum was then constructed using the norm of the complex coefficients. A 9 Hz peak was the evidence of noise emanating from a mechanical source or due to building vibrations. Subsequent analysis of data recorded at static conditions showed once again a low frequency peak of approximately 9 Hz. It was then concluded that the compressor of the building was not the source of the noise. Consequently, to improve the signal, the pressures were logged at 100 Hz for 20 – 40 second intervals (180 – 360 periods of the 9 Hz fluctuation) and averaged over this duration. Details regarding the Fourier analysis are given in Appendix A. The magnitude of the spectral coefficient associated with the 9 Hz peak was 8×10^{-2} % of the zero mode coefficient, and thus considered to have a negligible dynamic effect (flow acceleration) on flow behavior.

2.3.2 Holdup Measurement

The liquid volume fraction measured under two-phase flow conditions is known as holdup. Liquid holdup becomes an increasingly important factor when two-phase flow occurs in inclined or vertical pipes.

In order to quantify this two-phase parameter, at the end of each test run measurements of liquid holdup were performed by quickly closing a ball valve located at the bottom of the vertical pipe. The liquid trapped in the pipe accumulated by gravity in the bottom of the line. The holdup was then

determined based on the height of the liquid column compared to the total length of the pipe. This method is one of the most simple and convenient ways of measuring the liquid holdup; however, it is inherently prone to a slight underprediction since after the valve closure there is still some flow out of the line as it depressurizes after the valve.

The sudden shut-off the flow caused an impulsive rise in pressure upstream through the air and water lines. The pump had a relief valve set a pressure of 170 Psi to ensure no damage when a rise in pressure occurred.

2.4 Air-Water-Polymer System

Flow measurements with the polymer solution were obtained in a similar fashion. The pressure and holdup measurements with the air-water-polymer system followed the procedure described above. They only differed from the experiments with air and water in that a master polymer solution had to be prepared approximately 16 hours before an experiment was performed. A solution of a co-polymer of polyacrylamide and sodium-acrylate (Percol 727) in water was used. This polymer was provided by Ciba Chemicals with the name of Magnafloc 1011.

2.4.1 Solution Preparation

A batch of polymer solution at the required concentration was prepared in the 0.34 m^3 feed tank. Percol 727, in the form of a white powder was gently mixed with tap water by a method described in Foshee et al. (1976). A stirrer was completely assembled at the facility with the motor, gear box and impeller aligned and mounted at the top of the tank. The agitator was designed to stir slowly at a speed of 75 rpm in order to avoid mechanical degradation of the polymer. With the stirrer on, the dry polymer was sprinkled uniformly onto the water within 60 seconds. The solution was agitated for a period of 2 or 3 hours, allowed to stand overnight and stirred again about 20 minutes before using.

2.4.2 Viscosity measurements

Polymer degradation produced by an agitator is a function of the volume in the container, the polymer concentration, the shaker speed and amplitude as well as the mixing time. Degraded polymer solutions may exhibit lower activity than non-degraded solutions at the same concentration.

Viscosity is very sensitive to degradation and change in concentration. To ensure reproducibility of solution properties for every batch of polymer solution prepared at a certain concentration, the viscosity of the polymer solution was

measured at different shear rates. A range of shear rates from 2.25 sec^{-1} to 450 sec^{-1} was considered as well as polymer concentrations from 30 to 140 ppm (weight basis).

A Brookfield Cone/Plate LVT Viscometer was satisfactory for use at shear rates of about 45 to 450 sec^{-1} for 75 – 140 ppm hydrolyzed polymer solutions in fresh water. This instrument was not sensitive enough for low polymer concentrations in water. The measured viscosities as a function of shear rate for samples taken from different batches of polymer solution at the same concentration are given in Appendix C. Figure 2.2 shows the measured viscosities as a function of shear rate over the range of polymer concentrations studied. Solutions at all concentrations show significant shear thinning; the fluid decreases resistance with increasing stress. In contrast, the viscosity for a given shear rate increases with increasing polymer concentration across the entire range of shear rates used.

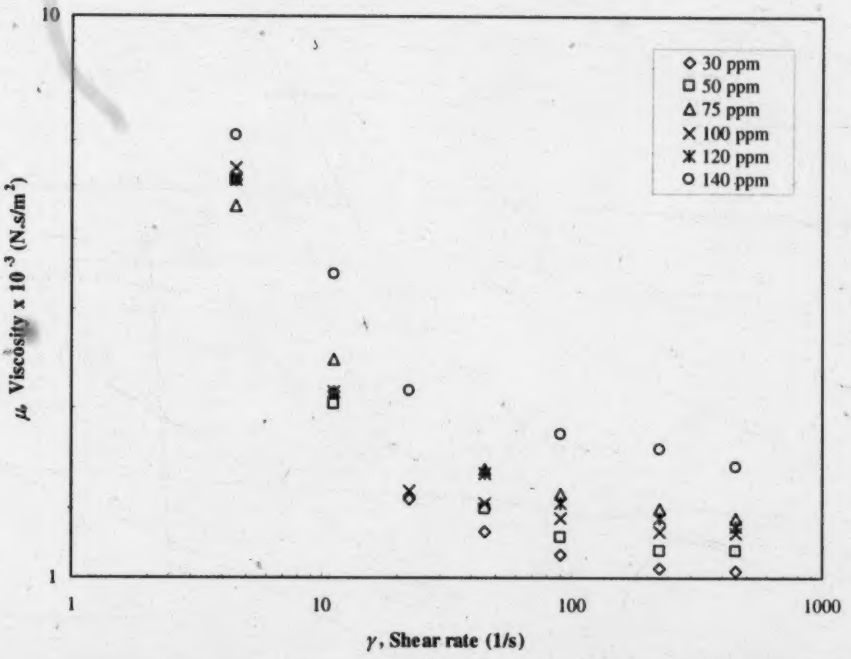

Figure 2.2: Viscosity μ as a function of the shear rate γ for polymer concentrations of 30 to 140 ppm. The viscosity of pure water is $1x10^{-3}$ Ns/m^2.

3 Implementation of an Annular Dispersed Flow Model

Motivated by the observation of the suppression of wave height and droplet entrainment with the injection of DRA (Al-Sarkhi and Hanratty, 2001a), a mechanistic model was adopted to quantify the effect of these phenomena on the pressure gradient. Film thickness, liquid entrainment and other two-phase flow parameters could be predicted by a model for vertical annular dispersed flow. The model was proposed by Oliemans et al. (1986) and based on the well-known two-fluid (separated flow) concept.

The measurements obtained in the experiments do not allow the direct determination of the relative contributions of the two-phase flow mechanisms to the overall drag reduction. To do so would require the measurement of quantities such as the entrainment rate, the entrained fraction and the film thickness. These quantities are difficult to obtain experimentally, and were not measured in the present experimental work.

3.1 Two-Phase Flow Parameters

Some parameters have been defined in two-phase flows to characterize flow patterns. These flow parameters play an important role in the two-phase flow calculation methods.

3.1.1 Superficial Velocities

The superficial velocity U_s is defined as the velocity a phase would obtain when flowing alone in a pipe of cross-sectional area A:

$$U_{sg} = \frac{\dot{m}_g}{\rho_g A} \tag{3.1}$$

$$U_{sl} = \frac{\dot{m}_l}{\rho_l A} \tag{3.2}$$

where $\dot{m}_g$ and $\dot{m}_l$ are the gas and liquid mass flow rates respectively.

Two-phase flow regimes often are presented as plots, or maps, with the phase superficial velocities or functions of them on each axis. One of the most recent significant works on two-phase flow through vertical tubes (Spedding et al., 2001) showed a flow regime map for vertical co-current air-water upflow in a 0.026 m I.D. pipe. Annular flow was obtained at superficial gas velocities ranging from 10 to 30 m/s and superficial liquid velocities up to 0.4 m/s. In the transition from slug to annular flow, an annular roll wave regime was also found at superficial gas velocities between 8 and 10 m/s and superficial liquid velocities from 0.15 to 0.3 m/s. This is shown in Figure 3.1. Some of the superficial velocities reported in the present investigation are indicated with a "+" sign in the annular regime. The rest of the experiments were performed outside the range of superficial liquid velocities used by Spedding et al. (2001).

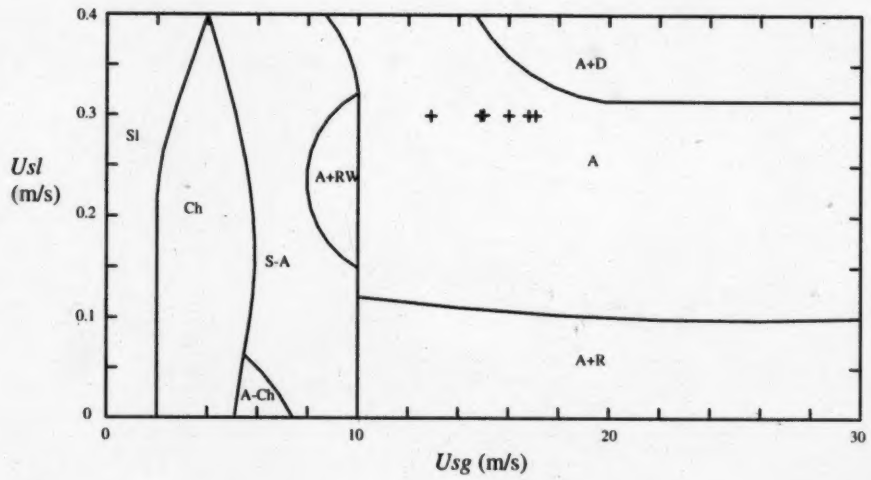

Figure 3.1: Flow regime map for +90° co-current vertical air/water flow in a 0.026 m I.D pipe (Spedding et al., 2001). *Sl* = Slug; *Ch* = Churn; *A-Ch* = Annular-Churn; *S-A* = Semi-Annular; *A+R* = Annular Ripple; *A* = Annular; *A+RW* = Annular Roll Wave; *A+D* = Annular Droplet.

3.1.2 Volume Fraction

An important correlation parameter in two-phase flow calculations is the phase volume fraction λ, defined as:

$$\lambda_l = \frac{Q_l}{Q_l + Q_g} = \frac{U_{sl}}{U_{sl} + U_{sg}} \tag{3.3}$$

$$\lambda_g = \frac{Q_g}{Q_l + Q_g} = \frac{U_{sg}}{U_{sl} + U_{sg}} \tag{3.4}$$

where Q_g and Q_l are the gas and liquid volumetric flow rates respectively.

Note that $\lambda_l + \lambda_g = 1$

3.1.3 Holdup and Actual Phase Velocities

When gas and liquid flow in a pipe, the local liquid volume fraction is greater than it is under non-flowing conditions, due to the effect of slip between the fluids. The lighter gas phase normally moves faster than the liquid phase; the liquid has the tendency to accumulate in horizontal and inclined pipe segments.

The liquid occupies a part A_l of the total cross-section. The liquid volume fraction measured under two-phase flow conditions is known as holdup, and defined as:

$$\alpha_l = \frac{A_l \cdot dx}{A \cdot dx} = \frac{A_l}{A} \tag{3.5}$$

While for gas flow the remaining part, A_g, is available:

$$\alpha_g = \frac{A_g \cdot dx}{A \cdot dx} = \frac{A_g}{A} \tag{3.6}$$

with $\alpha_g + \alpha_l = 1$

Due to the slip effect in horizontal and inclined pipe segments the liquid holdup α_l is larger than the liquid volume fraction λ_l:

$$\alpha_l \geq \lambda_l \tag{3.7}$$

The equality sign holds for the no-slip or homogeneous flow condition, when the two phases are well mixed and travel at equal velocities.

When the phase holdup is known it is possible to compute from the superficial velocities the actual phase velocities U_g and U_l in the pipe:

$$U_g = \frac{Q_g}{A_g} = \frac{Q_g}{A} \cdot \frac{A}{A_g} = \frac{U_{sg}}{\alpha_g} \tag{3.8}$$

$$U_l = \frac{Q_l}{A_l} = \frac{Q_l}{A} \cdot \frac{A}{A_l} = \frac{U_{sl}}{\alpha_l} \tag{3.9}$$

3.1.4 Friction factor

When fluid flows through pipes or channels, a certain amount of power is needed to overcome the wall friction. By a force balance, the wall shear stress τ_w in a fully developed pipe flow is related to the pressure drop by the following equation:

$$\tau_w = \frac{1}{2} f \rho U^2 \tag{3.10}$$

where the Fanning friction factor f is defined as:

$$f = \frac{D}{2\rho U^2}\left(\frac{dP}{dx}\right) \tag{3.11}$$

In annular two-phase flow, the turbulent processes in the liquid film have a negligible direct contribution to the pressure gradient. That is, most of the two-phase pressure gradient in annular-entrained flow is due to the gas flow and the interaction between the gas and liquid phases. Therefore, for annular two-phase flow, the Fanning friction factor is conventionally defined in terms of the density and superficial velocity of the gas as follows:

$$f = \frac{D}{2\rho_g U_{sg}^{\ 2}}\frac{dP}{dx} \tag{3.12}$$

where D is the pipe diameter, ρ_g is the gas density and dP/dx is the frictional pressure gradient.

3.1.5 Reynolds and Densimetric Froude Numbers

It has been demonstrated in the single-phase flow literature that for isothermal flow the shape and pressure distribution of the flow system is fully described by two dimensionless numbers, the Reynolds number and the Froude number. Similarly, these dimensionless numbers are extremely important for two-phase flow scaling.

By convention, in two-phase flow, the superficial Reynolds numbers are calculated as follows:

$$\mathrm{Re}_{sg} = \frac{D\rho_g U_{sg}}{\mu_g} \tag{3.13}$$

$$\mathrm{Re}_{sl} = \frac{D\rho_l U_{sl}}{\mu_l} \tag{3.14}$$

The densimetric liquid and gas Froude numbers are conventionally defined as:

$$F_l = \sqrt{\frac{\rho_l}{\rho_l - \rho_g}\frac{U_{sl}^{\ 2}}{gD}} \tag{3.15}$$

$$F_g = \sqrt{\frac{\rho_g}{\rho_l - \rho_g}\frac{U_{sg}^{\ 2}}{gD}} \tag{3.16}$$

3.2 Assumptions

The physical model for annular flow is given in Figure 3.2. Based on the two-fluid concept, the liquid at the wall is regarded as one phase and the gas plus droplets in the core as the other. The model is based on the following assumptions:

1. There is a steady-state, 1-D, upward and developed two-phase flow.

2. Axisymmetric flow (e.g. circumferentially uniform phase distribution) and mean velocity field.

3. The liquid and gas mass flow rates $\dot{m}_l$ and $\dot{m}_g$ (or superficial liquid and gas velocities U_{sl} and U_{sg}) are given.

4. The liquid droplets in the core travel at the gas speed (homogeneous flow).

5. The physical properties, i.e. the liquid and gas densities ρ_l and ρ_g, viscosities μ_l and μ_g and surface tension σ, are constant. Although the gas density changes along the pipe due to the pressure loss, the gas density is taken to be approximately equal to the one corresponding to the middle of the pipe. This assumption might not be a serious restriction in this case since the gas density only changes by 6%. Details regarding the calculation of the properties of the fluids are given in Appendix C.

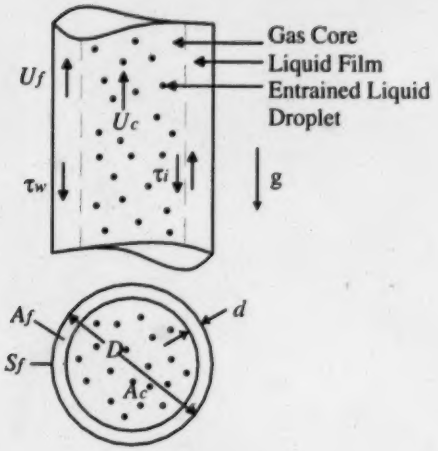

Figure 3.2: Physical Model for Annular Flow

3.3 The Pressure Gradient in the Model

Based on the generic fluid theory for flow in closed ducts (Panton, 1996), an expression for the pressure gradient is derived from the momentum equation. The momentum equation in i-direction for an inertial control volume CV is:

$$\frac{d}{dt}\int_{CV}\rho U_i dV = \int_{CV}\rho F_i dV + \int_{CS} R_i dS \tag{3.17}$$

The product ρU_i is the i-direction momentum per unit volume. Therefore, $\rho U_i dV$ is the i-direction momentum within the element dV. F_i stands for a body force per unit mass (e.g. gravity) and R_i stands for a surface force per unit area (e.g. pressure and viscous shear stress).

The left hand side of Equation 3.17 can be changed by using two fundamental theorems for a volume integral. Leibnitz's theorem can be used to move the time differentiation inside the integral:

$$\frac{d}{dt}\int_{CV}\rho U_i dV = \int_{CV}\frac{d}{dt}(\rho U_i)dV + \int_{CS} n_j U_j \rho U_i dS \tag{3.18}$$

Next, the theorem of Gauss changes the surface integral in Equation 3.18 into a volume integral:

$$\frac{d}{dt}\int_{CV}\rho U_i dV = \int_{CV}\frac{d}{dt}(\rho U_i)dV + \int_{CV}\frac{dU_j}{dj}\rho U_i dV \tag{3.19}$$

In indicial notation, Equation 3.19 can be written as:

$$\frac{d}{dt}\int_{CV}\rho U_i dV = \int_{CV}\partial_\circ \rho U_i dV + \int_{CV}\partial_j U_j \rho U_i dV \tag{3.20}$$

Substitution of Equation 3.20 into Equation 3.17 gives:

$$\int_{CV}\partial_\circ \rho U_i dV + \int_{CV}\partial_j(\rho U_j U_i)dV = \int_{CV}\rho F_i dV + \int_{CS} R_i dS \tag{3.21}$$

The dependence of the surface force R_i upon the outward unit normal vector n_j may be given by introducing a stress tensor T_{ji} that obeys the equation:

$$R_i = n_j T_{ji} \tag{3.22}$$

Substitution of the surface stress Equation 3.22 into Equation 3.21 and application of the Gauss's theorem to the surface force yields:

$$\int_{CV} \partial_* \rho U_i dV + \int_{CV} \partial_j (\rho U_j U_i) dV = \int_{CV} \rho F_i dV + \int_{CV} \partial_j T_{ji} dV \tag{3.23}$$

or

$$\int_{CV} [\partial_* (\rho U_i) + \partial_j (\rho U_j U_i) - \rho F_i - \partial_j T_{ji}] dV = 0 \tag{3.24}$$

Since the region of integration is arbitrary, the integrand must be zero everywhere. Hence,

$$\partial_* (\rho U_i) + \partial_j (\rho U_j U_i) = \rho F_i + \partial_j T_{ji} \tag{3.25}$$

The normal stress is the sum of pressure and normal viscous stress:

$$T_{ji} = -P_t \delta_{ji} + \tau_{ji} \tag{3.26}$$

where P_t is the thermodynamic pressure and τ_{ji} is the viscous stress tensor.

Substitution of Equation 3.26 into Equation 3.25 gives:

$$\partial_* (\rho U_i) + \partial_j (\rho U_j U_i) = -\partial_i P + \partial_j \tau_{ij} + \rho F_i \tag{3.27}$$

In symbolic notation, Equation 3.27 is of the form:

$$\frac{\partial}{\partial t}(\rho \vec{U}) + \nabla \cdot (\rho \vec{U} \vec{U}) = -\nabla P + \nabla \cdot \vec{\tau} + \rho \vec{F} \tag{3.28}$$

For steady ($\partial(\rho\vec{U})/\partial t = 0$), isothermal, single-phase pipe flow, Equation 3.28 becomes:

$$-\frac{dP}{dx} = \rho g + \tau_w \frac{S}{A} + \rho \frac{d}{dx} U_x^2 \qquad (3.29)$$

where dP/dx is the pressure loss per axial unit length, τ_w is the wall shear stress, S is the pipe perimeter and A is the cross-sectional area of the pipe.

Similarly, for two-phase annular flow, the pressure gradient can also be expressed as the sum of three components due to gravity, friction and acceleration. It is possible to calculate the three contributions to the pressure gradient by setting up a momentum balance to the whole-pipe contents:

$$-\frac{dP}{dx} = \left(\alpha_f \rho_l + \alpha_c \rho_c\right) g + \frac{\tau_w S}{A} + \frac{d}{dx}\left(\rho_l \frac{U_{sf}^2}{\alpha_f} + \rho_c \frac{U_{sc}^2}{\alpha_c} \right) \qquad (3.30)$$

where the subscripts f and c denote for film and core respectively.

3.4 Model Equations

In two-phase flow, the pressure gradient is strongly linked to entrainment. An entrainment fraction, E, is defined as the ratio of the flow rate of liquid drops to the total liquid flow. In order to incorporate E in the separated flow model, the gas and the entrained droplets are regarded as one phase, and the remaining liquid layer at the pipe wall as the other phase. It is assumed that there is no slip

between the droplets and the gas. The gas and liquid droplets are therefore lumped together and modified flow parameters are calculated as follows:

3.4.1 Film and Core Velocities

The superficial velocity of the liquid entrained U_{sle} is defined as:

$$U_{sle} = E \cdot U_{sl} \tag{3.31}$$

The superficial velocities of the core and film, U_{sc} and U_{sf}, are then given by:

$$U_{sc} = U_{sg} + E \cdot U_{sl} \tag{3.32}$$

$$U_{sf} = (1 - E) U_{sl} \tag{3.33}$$

3.4.2 Holdup

The total liquid holdup α_l follows from adding the volume fraction of liquid entrained to the film holdup:

$$\alpha_l = \alpha_f + (1 - \alpha_f) \frac{E \cdot U_{sl}}{U_{sg} + E \cdot U_{sl}} \tag{3.34}$$

The film holdup α_f is related to the film cross-section:

$$\alpha_f = \frac{A_f}{A} \tag{3.35}$$

The cross-sectional areas of the film and pipe, A_f and A, are given by:

$$A_f = \pi d\,(D-d) \tag{3.36}$$

where d is the film thickness

$$A = \frac{\pi}{4} D^2 \tag{3.37}$$

Substitution of Equation 3.36 and 3.37 into Equation 3.35 yields:

$$\alpha_f = \frac{4d}{D}\left(1-\frac{d}{D}\right) \tag{3.38}$$

3.4.3 Core Holdup

The core holdup α_c is related to the core cross-section:

$$\alpha_c = \frac{A_c}{A} \tag{3.39}$$

where the cross-sectional area of the core A_c is given by:

$$A_c = \frac{\pi}{4}(D-2d)^2 \tag{3.40}$$

By substituting Equation 3.37 and 3.40 into Equation 3.39, the core holdup is calculated as:

$$\alpha_c = \frac{(D-2d)^2}{D^2} \tag{3.41}$$

3.4.4 Core Density and Viscosity

The core average density ρ_c and viscosity μ_c are defined as:

$$\rho_c = \rho_g \lambda_c + \rho_l (1-\lambda_c) \tag{3.42}$$

$$\mu_c = \mu_g \lambda_c + \mu_l (1-\lambda_c) \tag{3.43}$$

where the gas void fraction in the core λ_c is given by:

$$\lambda_c = \frac{U_{sg}}{U_{sg} + EU_{sl}} \tag{3.44}$$

3.4.5 Wall Shear Stress

The shear stress at the wall is calculated as follows:

$$\tau_w = \frac{1}{2} f_f \rho_l U_f^{\,2} \tag{3.45}$$

The average film velocity U_f is defined as:

$$U_f = \frac{U_{sf}}{\alpha_f} \tag{3.46}$$

A convenient relationship for the calculation of the film Fanning friction factor f_f is that of Churchill (Oliemans, 2001):

$$f = 2\left[(8/\mathrm{Re})^{12} + 1/(a+b)^{3/2}\right]^{1/12} \tag{3.47}$$

where:

$$a = \left[2.547 \ln\left((7/\mathrm{Re})^{0.9} + 0.27\varepsilon/D\right)\right]^{16} \tag{3.48}$$

$$b = (37530/\mathrm{Re})^{16} \tag{3.49}$$

The Reynolds number for the liquid film is defined as:

$$\mathrm{Re}_f = \frac{\rho_l U_f D_f}{\mu_l} \tag{3.50}$$

The hydraulic diameter for the film D_f is assumed to result from:

$$D_f = \frac{4A_f}{S_f} = \alpha_f D \tag{3.51}$$

where the film perimeter S_f follows from:

$$S_f = \pi D \tag{3.52}$$

3.5 Calculation Methodology

The sequence followed to estimate the drag reduction is shown schematically in Figure 3.3. Starting from an educated estimate of entrainment fraction, the hydrostatic, frictional and acceleration contributions to the measured pressure gradient were determined iteratively using the following calculation steps:

1. The film holdup α_f is calculated from Equation 3.34 by using the experimentally determined value of liquid holdup.

2. The film thickness d is calculated using Equation 3.38.

3. The core holdup α_c, void fraction λ_c, density ρ_c and viscosity μ_c are calculated using Equations 3.41, 3.44, 3.42 and 3.43 respectively.

4. The superficial velocity of the liquid in the film U_{sf} is calculated using Equation 3.33. The average film velocity U_f is then determined from Equation 3.46 by using the calculated film holdup.

5. The film Fanning friction factor f_f is calculated using Churchill correlation (Equations 3.51, 3.50, 3.47, 3.48 and 3.49). A smooth pipe is assumed.

6. The wall shear stress is calculated using Equation 3.45.

7. The hydrostatic *Hyd*, frictional *Fr* and acceleration *Acc* components of the pressure gradient are calculated as they are defined in Equation 3.30. It is verify that the sum of all of them is equal to the measured pressure gradient. This one is taken as the slope of the linear regression line through the observed pressures along the pipe. A sample calculation of the pressure gradient from the measured pressures is given in Appendix A.

This procedure was repeated for the air-water-polymer data assuming suppression of droplet entrainment with the addition of DRA ($E = 0$). The effectiveness of the polymer was then evaluated and expressed in terms of the drag reduction (DR) as:

$$\%DR = \left(1 - \frac{f_{with\ DRA}}{f_{without\ DRA}}\right) \times 100 \tag{3.53}$$

where the two-phase friction factors $f_{withDRA}$ and $f_{withoutDRA}$ were calculated as defined in Equation 3.12.

Alternatively, drag reduction can be defined as:

$$\%DR = \left(1 - \frac{(dP/dx)_{with\ DRA}}{(dP/dx)_{without\ DRA}}\right) \times 100 \tag{3.54}$$

where $(dP/dx)_{withDRA}$ and $(dP/dx)_{withoutDRA}$ are the frictional pressure gradients occurring for pipe flow at a given flow rate, with and without the drag reducing additive respectively.

The two drag reduction definitions are quantitatively equivalent when the superficial gas velocity and gas density are identical with and without the DRA. However, in the present investigation, the gas density and superficial gas velocity changed slightly so Equation 3.53 was used.

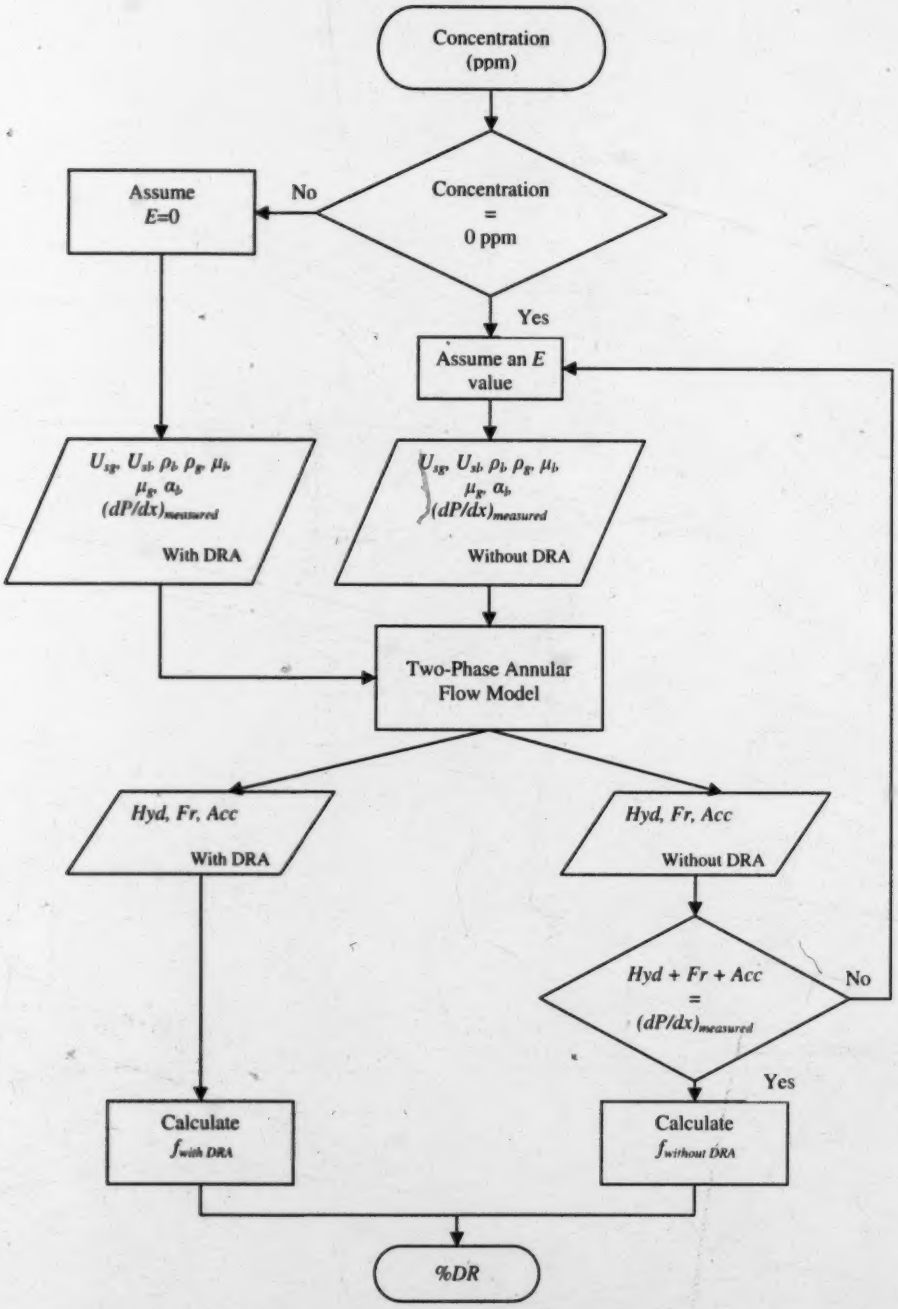

Figure 3.3: Schematic of calculation procedure to estimate drag reduction

4 Model Results

4.1 Effect of Polymer Concentration on the Drag Reduction

For given gas and liquid flow rates the pressure drop was measured as a function of the concentration of the polymer in the liquid phase. To minimize degradation effects discussed later in Section 4.5, "once-through" operation was used so that the drag reduced solution was discharged to drain after one pass through the apparatus. The influence of polymer concentration on the percent drag reduction is displayed in Figure 4.1. The drag reduction increased with increasing concentration and, eventually, reached a maximum value above which the effectiveness of the DRA decreased.

As can be seen in Figure 4.1, the maximum drag reduction was reached at a polymer concentration of 75 ppm. Further increases in polymer concentration had an intriguing effect not observed in previous studies with drag reducing polymers. It is seen from Figure 4.1 that the drag reduction follows no set trend for concentrations higher than 75 ppm. The drag reduction does not steadily decreases after reaching a maximum; instead, sudden changes are observed at high enough concentrations. In contrast, according to the work presented by Al-Sarkhi and Hanratty (2001a,b), the drag reduction eventually reaches a plateau and no further change is observed with increasing concentration. However, their

studies (Al-Sarkhi and Hanratty, 2001a,b) were conducted in horizontal pipes. Furthermore, they observed a change in flow regime to a stratified and annular pattern with no disturbance waves with the addition of the DRA. The sudden changes shown in Figure 4.1 at high enough concentrations could also be looked upon as an effect of a change in flow regime; unfortunately, no visual observations were done during the experiments.

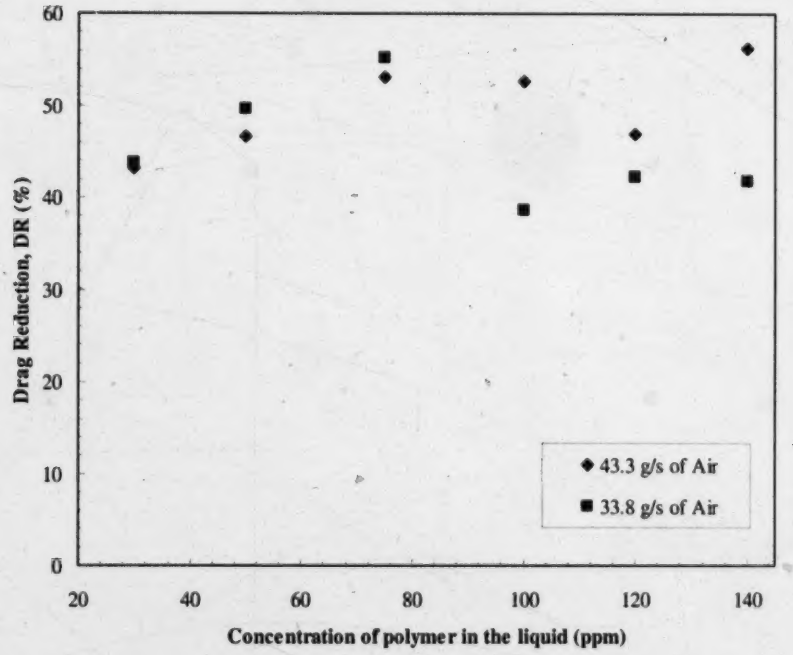

Figure 4.1: Variation of drag reduction with polymer concentration at a liquid mass flow rate of 145 g/s.

One way of helping characterize the discrepancies of these results was by identifying pressure fluctuations.

Table 4.1 shows the effect of pressure variations on the liquid holdup α_l and the overall pressure gradient *dP/dx* for given fixed gas and liquid flow rates of 43.3 g/s and 145 g/s respectively. The first pressure transducer located at the bottom of the test section (downstream the mixing tee) is indicated as 1 so that P_1 to P_6 correspond to the pressures measured from the bottom to the top of the vertical pipe. The pressure upstream the orifice plate in the air line is indicated as P_{up}.

As the DRA concentration was increased up to 75 ppm all pressures steadily decreased as did the pressure gradient; as a result, the drag reduction increased. Further increasing of DRA concentration to 120 ppm was accompanied by an increase in the measured pressures, e.g. the pressure measured right before the separator inlet P_6 increased from 345 kPa to 351 kPa. The pressure gradient *dP/dx* increased from 3436 Pa/m to 3697 Pa/m and the liquid holdup decreased from 0.100 to 0.096. This is due to the fact that degradation of the polymer occurred when all pressures in the system suddenly increased. The more concentrated the solution the larger the entanglements of polymer chains. However, those aggregates could have been irreversibly broken by the impingement of the gas on the polymer solution thus reducing its effectiveness to

47%. As the drag reducing effectiveness of the polymer decreased its capability to lift liquid (explained in more detail in Section 4.2.2) also decreased resulting in lower liquid holdups. At a polymer concentration of 140 ppm there was a sudden decrease in the measured pressures which led to a decrease in the pressure gradient and consequently, a sudden increase in drag reduction.

These results show that small changes in the pressures resulted in marked variations in the drag reduction. It is believed that variations in the back pressure are responsible for this behavior since the pressure in the separator was not controlled. Any variation in the back pressure could cause an undesired upstream pressure P_{up} and affect the rest of the pressures and the pressure gradient to some extent. It will be shown later that the results of the repeatability tests support this viewpoint.

Similarly, Table 4.2 gives an overview of the average pressures, liquid holdup and pressure gradient obtained for given fixed gas and liquid flow rates of 33.8 g/s and 145 g/s respectively at various polymer concentrations. It can be seen that all pressures decreased as the DRA concentration was increased up to 75 ppm. A decrease in all pressures resulted in a decrease in the overall pressure gradient and consequently the drag reduction increased. Further increasing DRA concentration to 100 ppm was accompanied by an increase in the measured pressures and pressure gradient. Therefore, the drag reduction decreased to

38.6 %. No sudden change was observed for concentrations of 120 ppm and 140 ppm.

Table 4.1: Summary of the results obtained at gas and liquid flow rates of 43.3 g/s and 145 g/s respectively and various polymer concentrations.

		30 ppm	50 ppm	75 ppm	100 ppm	120 ppm	140 ppm
$\dot{m}_g$	(g/s)	46.5	42.2	43.0	42.9	43.4	43.7
$\dot{m}_l$	(g/s)	144	145	142	146	146	147
P_1	(kPa)	441	394	388	390	397	384
P_2	(kPa)	433	387	380	382	389	377
P_3	(kPa)	424	378	373	374	381	369
P_4	(kPa)	414	370	365	366	372	361
P_5	(kPa)	405	361	357	358	364	353
P_6	(kPa)	392	349	345	347	351	341
P_{up}	(kPa)	473.4	422.2	416.2	419.4	427.6	412.2
dP/dx	(Pa/m)	3952	3619	3436	3462	3697	3413
a_l		0.093	0.100	0.100	0.103	0.096	0.104
ρ_l	(kg/m^3)	998	998	998	998	998	998
ρ_g	(kg/m^3)	4.97	4.44	4.37	4.39	4.47	4.33
U_{sg}	(m/s)	18.5	18.8	19.4	19.3	19.2	20.0
U_{sl}	(m/s)	0.284	0.288	0.280	0.289	0.288	0.290
Hyd	(Pa/m)	952	1020	1020	1048	976	1058
Fric	(Pa/m)	2776	2390	2202	2199	2501	2131
Acc	(Pa/m)	224	210	214	216	220	224
f		0.023	0.021	0.019	0.019	0.021	0.017
DR	(%)	43.2	46.6	53.0	52.6	47.0	56.2

Table 4.2: Summary of the results obtained at gas and liquid flow rates of 33.8 g/s and 145 g/s respectively and various polymer concentrations.

		30 ppm	50 ppm	75 ppm	100 ppm	120 ppm	140 ppm
$\dot{m}_g$	(g/s)	33.7	34.1	34.3	33.3	34.0	33.4
$\dot{m}_l$	(g/s)	143	143	145	145	145	145
P_1	(kPa)	338	330	319	328	329	317
P_2	(kPa)	331	323	312	321	321	310
P_3	(kPa)	323	315	305	313	313	302
P_4	(kPa)	315	308	297	304	305	293
P_5	(kPa)	307	300	290	296	296	285
P_6	(kPa)	295	288	279	284	284	273
P_{up}	(kPa)	365.5	355.9	343.7	358.1	357.5	344.4
dP/dx	(Pa/m)	3437	3312	3188	3606	3568	3593
a_l		0.108	0.108	0.112	0.100	0.102	0.101
ρ_l	(kg/m^3)	998	998	998	998	998	998
ρ_g	(kg/m^3)	3.78	3.69	3.57	3.66	3.66	3.52
U_{sg}	(m/s)	17.6	18.3	19.0	18.0	18.3	18.7
U_{sl}	(m/s)	0.282	0.282	0.286	0.288	0.288	0.286
Hyd	(Pa/m)	1087	1092	1124	1013	1030	1018
Fric	(Pa/m)	2182	2047	1885	2418	2360	2396
Acc	(Pa/m)	168	173	178	175	178	179
f		0.026	0.023	0.020	0.028	0.026	0.026
DR	(%)	43.8	49.6	55.1	38.6	42.2	41.8

4.2 Effect of System Parameters on the Flow Characteristics

To investigate more thoroughly the phenomenon of drag reduction, flow measurements were obtained by initially setting a liquid mass flow rate and systematically increasing the air mass flow rate to provide a data set. The experiments with the polymer solution were performed at a concentration of 75 ppm. Consequently, based on the previous results, drag reductions obtained at this concentration are considered as the maximum multiphase drag reduction that can be achieved under the particular flow conditions being tested.

The results reported are from "single pass" experiments where the DRA solution was passed once through the system. The experimental data are also presented in terms of the superficial gas Reynolds number Re_{sg} and the superficial velocities U_{sl} and U_{sg}. The effects of the various system parameters are discussed in the following sections.

4.2.1 Effect on Liquid Distribution

Most models for annular flow require a value of entrained fraction to calculate quantities such as the film thickness and the pressure drop (Oliemans et al., 1986; Ansari et al., 1994; Gomez et al., 1999; Manabe et al., 1996). Since the total pressure drop was determined experimentally, it was possible to get an

estimation of the entrainment fraction by an iteration procedure using the model equations presented in Section 3.4.

Figure 4.2 illustrates the behavior of the entrained liquid fraction with increasing the air mass flow rate. An increase in the superficial gas Reynolds number Re_{sg} corresponds to an increase in air flow rate. As observed in this plot, the fraction of liquid entrained E increases with increasing Re_{sg}. Similarly, the fraction of the liquid flow which is entrained appears to be higher for higher liquid flow rates. These results are also in line with an experimental assessment of such effects reported by Barbosa et al. (2002).

It is also important to mention that there is a high uncertainty associated with the values of entrainment presented in Figure 4.2. As shown in Appendix D, uncertainties in the range of ±31% to ±118 % were obtained when the liquid holdup and the pressure gradient were varied by ±5% to ±20%.

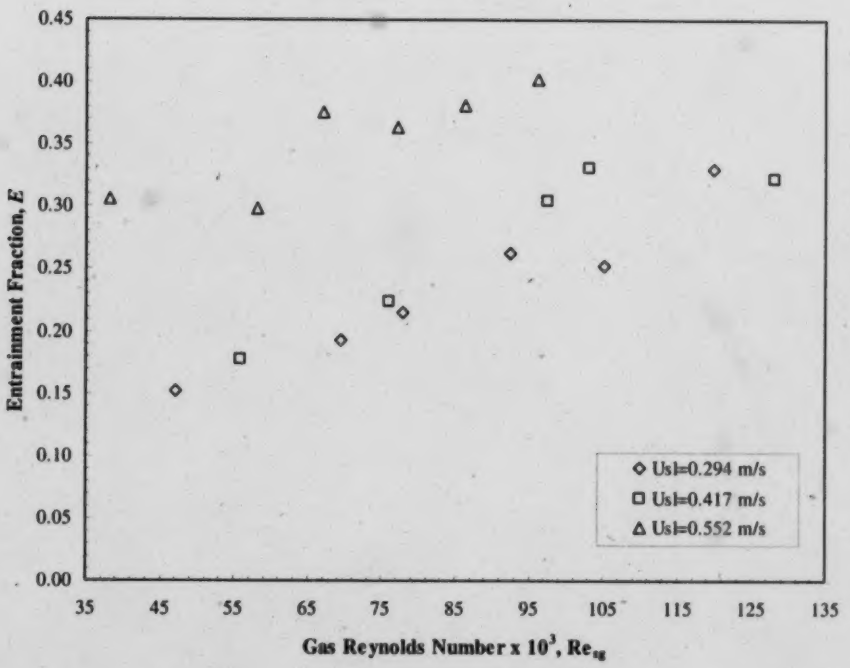

Figure 4.2: Liquid entrained fraction E as a function of superficial gas Reynolds number Re_{sg} and superficial liquid velocity U_{sl} for air-water only.

Figure 4.3 shows a comparison between entrained fraction determined by this approach and the calculated values using published correlations for vertical upward gas-liquid annular flow. This comparison was done for air-water only. The correlations used are the following:

Wallis (1969) suggested that:

$$E = 1 - \exp[-0.125\,(\phi - 1.5)] \tag{4.1}$$

where

$$\phi = 10^4 \frac{U_{sg}\mu_g}{\sigma}\left(\frac{\rho_g}{\rho_l}\right)^{1/2} \tag{4.2}$$

Ishii and Mishima (1989) proposed the following equation for fully developed flow:

$$E = \tanh\left(7.25 \cdot 10^{-7} We_l^{1.25} \mathrm{Re}_f^{0.25}\right) \tag{4.3}$$

where

$$We_l = We_g\left(\frac{\Delta\rho}{\rho_g}\right)^{1/3} \tag{4.4}$$

$$We_g = \frac{\rho_g U_{sg}^{\,2} D}{\sigma} \tag{4.5}$$

$$\Delta\rho = \rho_l - \rho_g \tag{4.6}$$

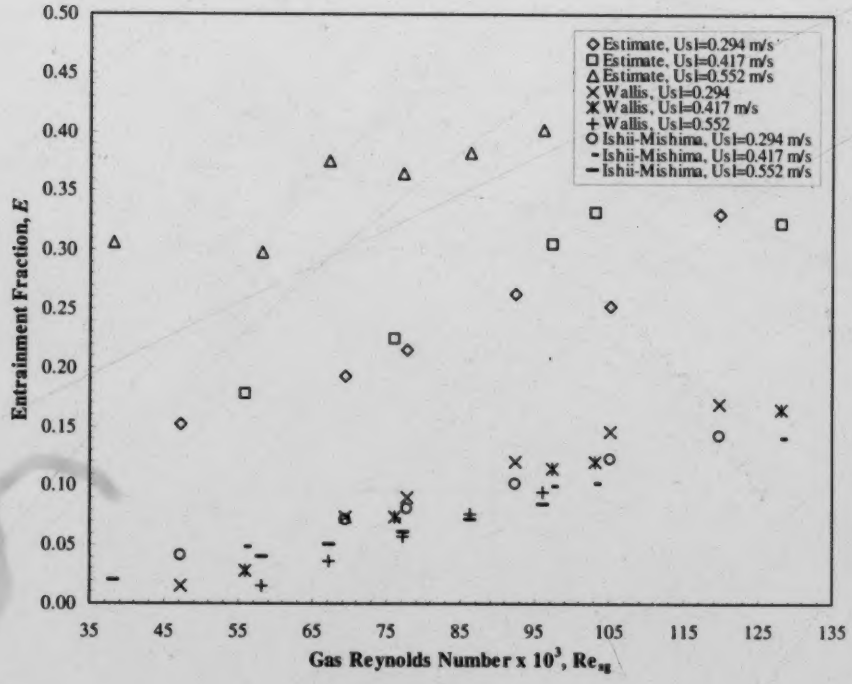

Figure 4.3: A comparison between entrained fraction estimated by the present approach and the predicted values using the correlations of Wallis (1969) and Ishii and Mishima (1989). These results were obtained for air-water only.

As can be seen in Figure 4.3, there are considerable differences between the estimated values and those calculated using the correlations above. The reason for the discrepancies observed could lie in the fact that the experimental conditions of the present investigation might not be within the application limits of Equations 4.1 and 4.3. According to Ishii and Mishima (1989), Equation 4.3 has been compared to many experimental data for air-water systems in the ranges of $1 < P < 4$ atm, $0.95 < D < 3.2$ cm, $370 < \mathrm{Re}_f < 6400$ and $U_{sg} < 100$ m/s, and the result has been shown to be satisfactory. In the present study, only the film Reynolds number Re_f was outside the limits above, ranging from 6329 to 9828. Therefore, Ishii and Mishima correlation might be restricted to $\mathrm{Re}_f < 6400$. No specific limits were given by Wallis (1969) however it is noted that Wallis correlation does not account for the effect of pipe diameter. In practice, no correlations can predict the entrainment fraction with the required accuracy over a wide range of system pressures and flow rates. As mentioned previously, there is also a high uncertainty associated with the values of entrainment obtained by the present approach. This might be the main reason for the significant differences between the estimated values and those given by the correlations.

As the gas flow rate is increased and the occurrence of disturbance waves starts, more droplets are entrained from the film into the gas core, thus decreasing film thickness. This trend can be observed in Figure 4.4 which shows the values of film thickness estimated, as explained in Section 3.5, for the various gas and

liquid superficial velocities. Flow with the polymer solution has a film thickness which is 1.1 to 1.4 times larger than what it was obtained for the air-water system. This can be ascribed to the assumption of suppression of entrainment after the addition of DRA. This assumption is reasonably consistent with previous work, for instance that of Al-Sarkhi and Hanratty (2001b). From visual observations, they concluded that an annular flow with disturbance waves changes to an annular flow with few, if any, disturbance waves after the addition of DRA.

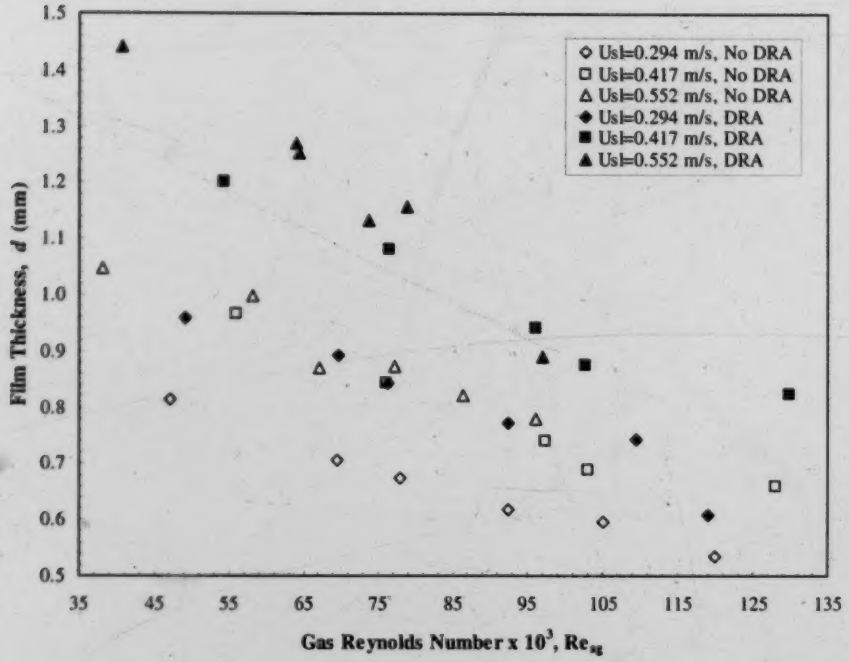

Figure 4.4: Film thickness *d* as a function of superficial gas Reynolds number Re_{sg} at various gas and liquid superficial velocities.

4.2.2 Effect on the Holdup

Figure 4.5 shows the experimentally determined values of the liquid holdup α_l as a function of the calculated superficial gas Reynolds numbers Re_{sg}. A total of 34 steady-state experiments, performed with air-water and air-water-polymer at various liquid and gas flow rates, are displayed in this figure.

An increase in the superficial liquid velocity leads to an increase in the holdup value. In contrast, lower holdup values were obtained as the superficial gas velocity was increased at constant superficial liquid velocity. This decrease is due to the higher drag exerted on the liquid phase at the interface by the faster moving gas.

The results in Figure 4.5 also show how the additive increases holdup by an average of 19%, 18% and 21% for superficial liquid velocities of 0.294 m/s, 0.417 m/s and 0.552 m/s, respectively. This is mainly due to less mixing and interaction between the phases with the addition of DRA. In gas-liquid annular flow, energy stored in the gas as pressure is transferred to the liquid phase as the gas expands along the pipe. This energy is then converted into kinetic, heat, or surface energy in the liquid phase. The drag reducing additive acts to impede the breakaway of droplets from the wavy sheared surface at the gas-liquid interface. This reduces the total fraction of surface energy developed, thus resulting in

more transfer of kinetic energy, and thus greater lift. The overall effect is a faster moving liquid phase covering a greater proportion of the pipe cross-section. These results show how well the DRA would perform in reducing liquid loading. This is useful information in assessing how polymer injection could extend the life of a liquid producing gas well by allowing for greater liquid lift.

In addition, the similarity of Figures 4.4 and 4.5 shows the strong relation between holdup and film thickness. It can be noted from Equations 3.34 and 3.38 that these two variables are strongly interrelated and directly affected by the entrainment.

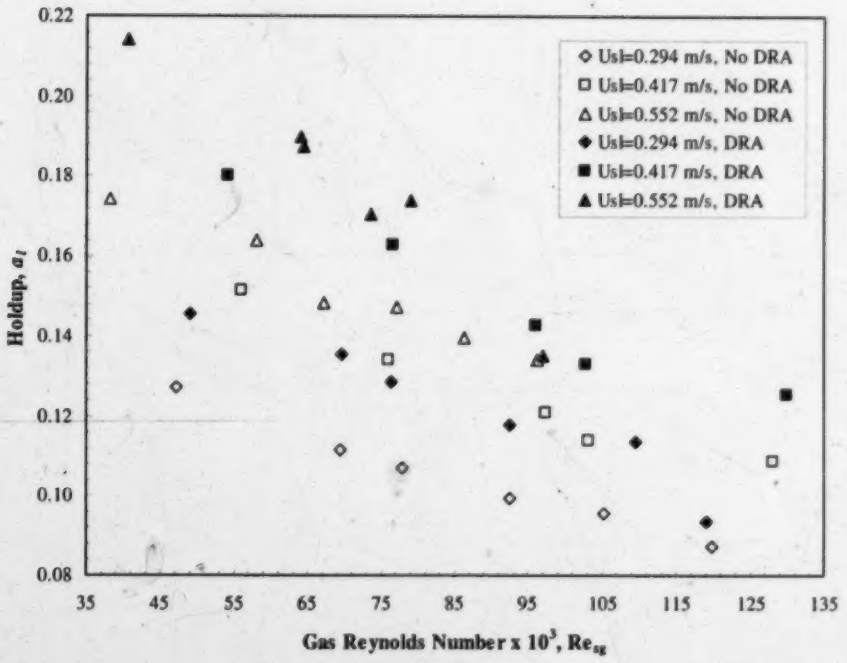

Figure 4.5: Measured values of liquid holdup α_l as a function of the superficial gas Reynolds number Re_{sg} at various gas and liquid superficial velocities.

Holdup data from air-water experiments were also compared with the holdup values predicted by using the modified Spedding-Chen correlation (Spedding et al. 2001):

$$\frac{\alpha_g}{\alpha_l} = [\,0.14 \ln U_{sl} + 1\,]\,[1 - \exp(-0.05 U_{sl} Q_g / Q_l)]\,[Q_g / Q_l]^{0.65} \qquad (4.7)$$

which was obtained from measured values of liquid holdup in a 0.026 I.D. +86.5° inclined pipe with co-current air-water flow.

In Figure 4.6, the experimentally determined values of the liquid holdup and the values calculated with Equation 4.7 have been plotted as a function of the superficial gas Reynolds number.

The measured values are about 26 – 48% lower than the predicted values with the modified Spedding-Chen correlation. This underprediction of the liquid holdup is partly explained by the fact that there is still some flow out of the line as it depressurizes after the valve is closed. An explanation for this remarkable difference might also lie in the application limits of Equation 4.7. According to Spedding et al. (2001), Equation 4.7 was found to predict the liquid holdup to within ±15% of the observed experimental value for gas flow rates ranging from 0.796 g/s – 21.2 g/s and liquid flow rates of 5.82, 33.3, 139 and 200 g/s. These flow rates are lower than those used in the present investigation; gas flow rates

ranging from 14.2 – 46.3 g/s and liquid flow rates of 148, 210 and 278 g/s were used.

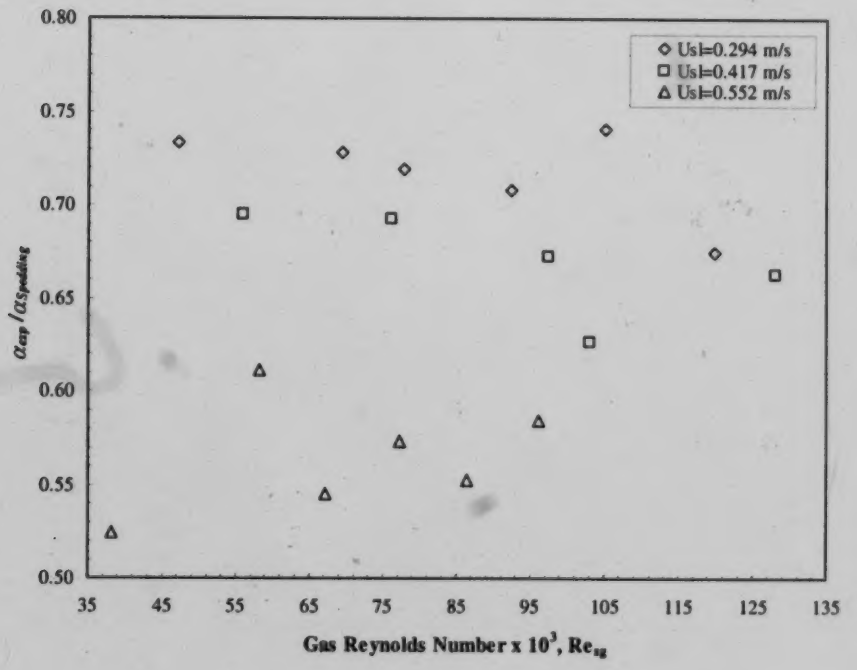

Figure 4.6: A comparison between the measured values of liquid holdup α_{exp} and the calculated values using Spedding's correlation $\alpha_{Spedding}$, for air-water only.

4.2.3 Effect on the Pressure Gradient

Figures 4.7, 4.8 and 4.9 show the average values for the measured pressure gradient and the calculated losses due to hydrostatic head, friction and acceleration.

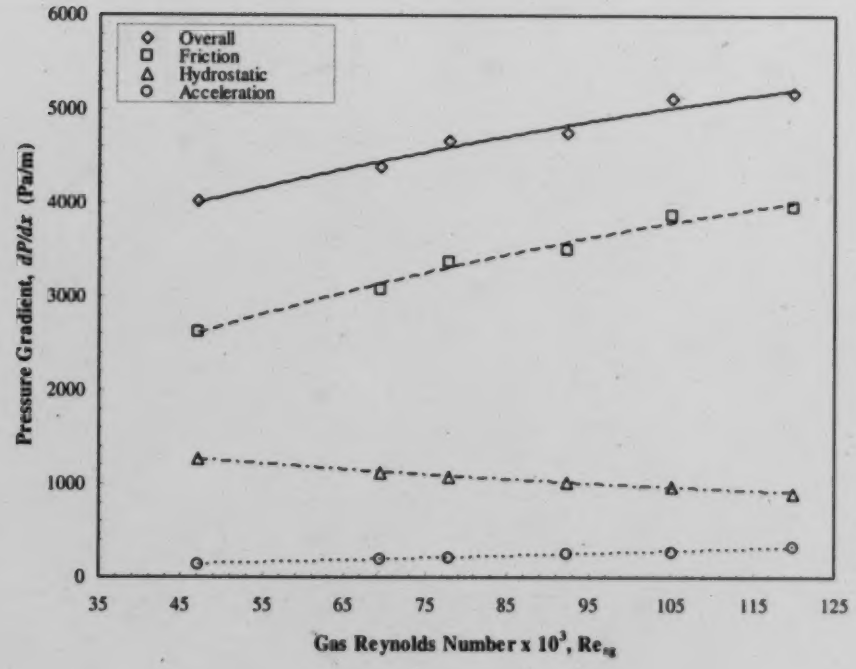

Figure 4.7: Two-phase pressure drop for air-water vertical flow at a superficial liquid velocity of 0.294 m/s and various superficial gas velocities. Also shown are the hydrostatic, frictional and acceleration components. The data points were fitted to a polynomial of second order.

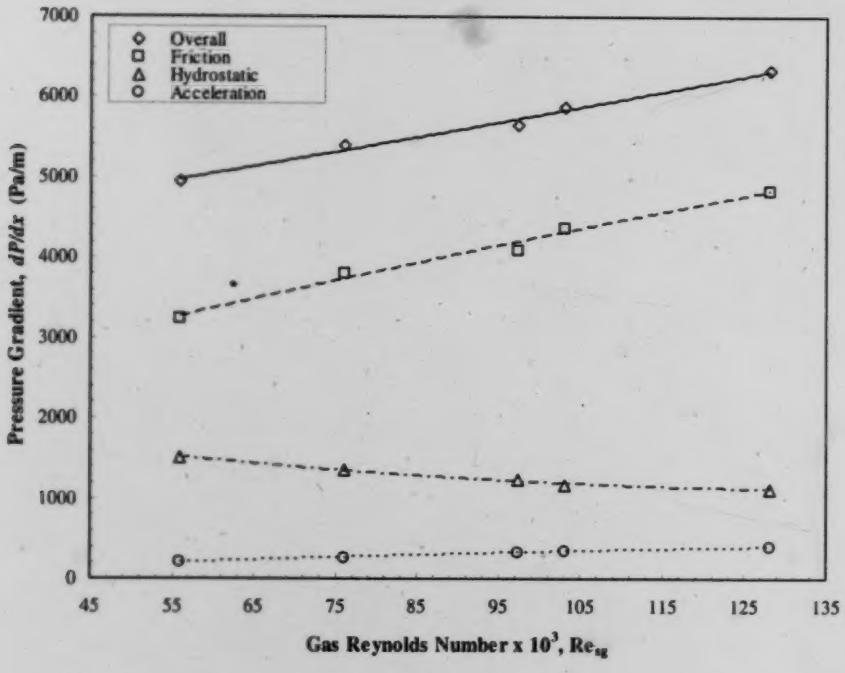

Figure 4.8: Two-phase pressure drop for air-water vertical flow at a superficial liquid velocity of 0.417 m/s and various superficial gas velocities. Also shown are the hydrostatic, frictional and acceleration components. The data points were fitted to a polynomial of second order.

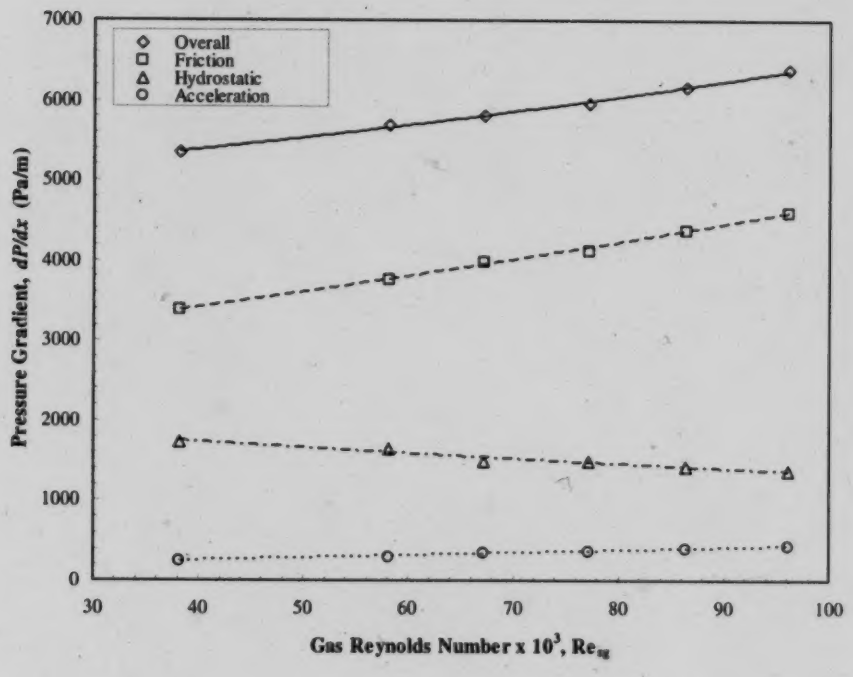

Figure 4.9: Two-phase pressure drop for air-water vertical flow at superficial liquid velocity of 0.552 m/s and various superficial gas velocities. Also shown are the hydrostatic, frictional and acceleration components. The data points were fitted to a polynomial of second order.

From these figures it is clear that the pressure drop in the air-water annular flow was mainly caused by friction. The acceleration component was found to be very small compared to the frictional and hydrostatic components. Thus the calculation of the frictional pressure drop by subtracting the two-phase head from the overall pressure drop would be within 3 – 7% error, as the effect of the flow acceleration along the pipe is ignored.

As the gas and liquid rates were increased the overall pressure gradient increased along with the gas density. A higher liquid rate introduces a higher shear stress at the wall leading to an increased frictional pressure gradient. An enhancement of the interfacial activity also contributes to this rise in the frictional component of pressure drop. As droplets are increasingly being formed, the rate of transfer of mechanical energy from the gas phase to the liquid phase increases resulting in a substantial increase of the overall pressure gradient. Furthermore, the weight of the entrained droplets as well as the weight of the gas and liquid film causes a hydrostatic pressure gradient. It was noted that, in general, the calculated hydrostatic pressure gradient paralleled changes in the liquid holdup. As the liquid flow rate increased the holdup increased as did the hydrostatic head.

When evaluating the significance of these competing effects it was found that the frictional term accounted for 70% of the total pressure gradient while the hydrostatic component contributed over 24%. This distribution changed

significantly when the polymer was added to the flow. As suggested by Figures 4.10, 4.11 and 4.12, at lower gas flow rates the hydrostatic head was the dominant contributor to the pressure gradient in the air-water-polymer flow. It represented about 56% of the overall pressure gradient. With the increase of gas flow rate, particularly beyond a Re_{sg} of $8x10^4$, the frictional component became larger than the hydrostatic pressure gradient which steadily reduced along with the holdup.

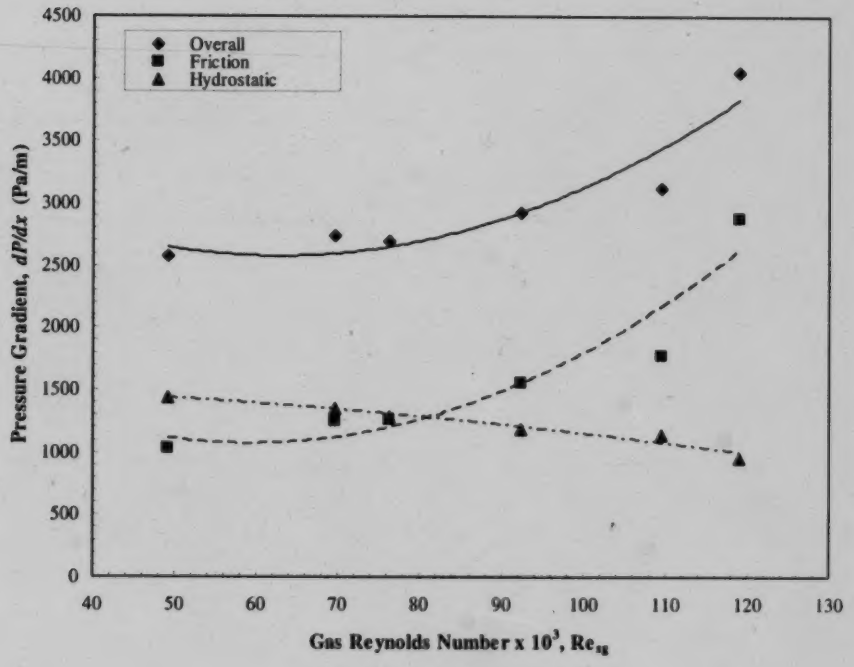

Figure 4.10: Two-phase pressure drop for air-water-polymer system at a superficial liquid velocity of 0.294 m/s and various superficial gas velocities. Also shown are the hydrostatic and frictional components. The data points were fitted to a polynomial of second order.

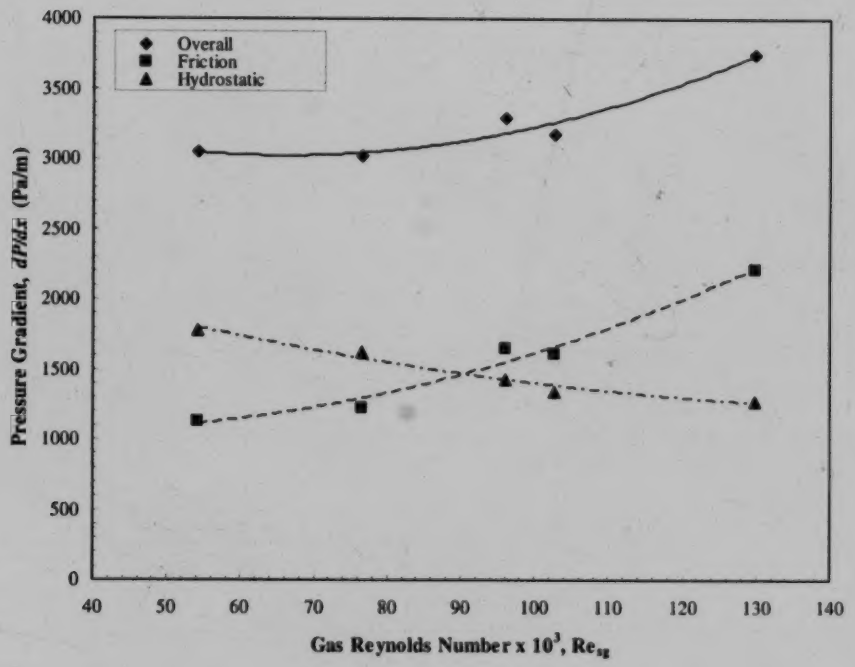

Figure 4.11: Two-phase pressure drop for air-water-polymer system at a superficial liquid velocity of 0.417 m/s and various superficial gas velocities. Also shown are the hydrostatic and frictional components. The data points were fitted to a polynomial of second order.

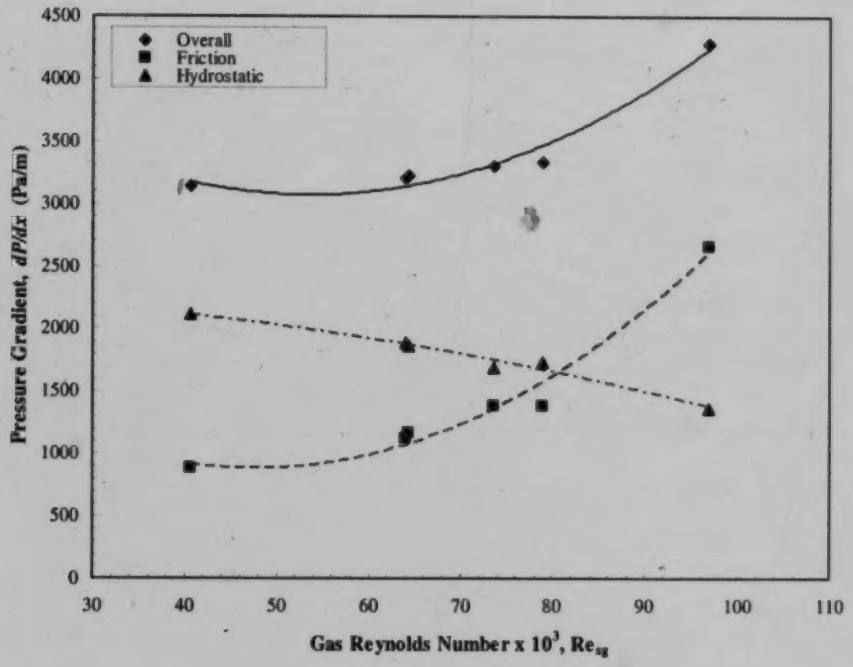

Figure 4.12: Two-phase pressure drop for air-water-polymer system at a superficial liquid velocity of 0.552 m/s and various superficial gas velocities. Also shown are the hydrostatic and frictional components. The data points were fitted to a polynomial of second order.

The overall effect of the DRA on the pressure gradient is shown in Figures 4.13 and 4.14. In these figures a comparison has been made between components of the pressure gradient obtained for the air-water system and air-water-polymer system.

The large reduction in the frictional component of the pressure gradient due to the presence of the polymer, as compared with the air-water flow, is clearly demonstrated in Figure 4.13. A decrease of about 63% in the frictional pressure gradient was obtained over the range of gas flow rates tested. A reverse effect, shown in Figure 4.14, was obtained on the hydrostatic component of the pressure gradient. The addition of DRA caused an increase of about 18% in the hydrostatic head.

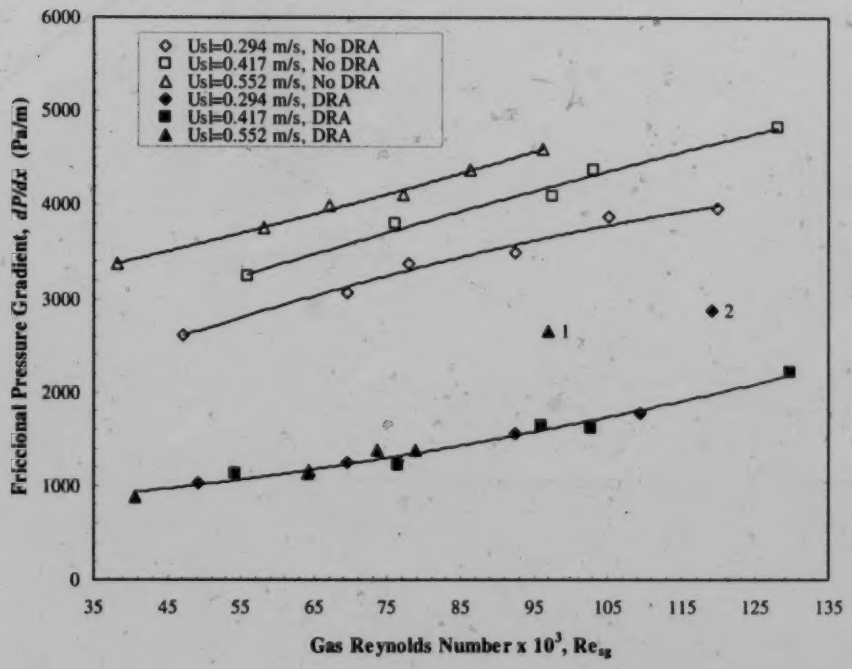

Figure 4.13: Effect of DRA on the frictional pressure gradient at various gas and liquid flow rates. The data points were fitted to a polynomial of second order.

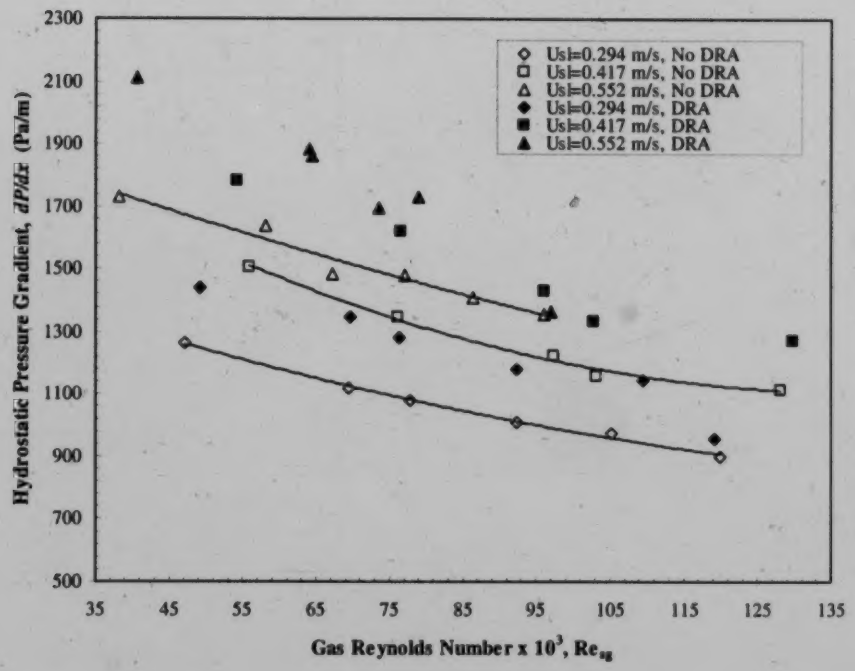

Figure 4.14: Effect of the DRA on the hydrostatic pressure gradient at various gas and liquid flow rates. The data points were fitted to a polynomial of second order.

Air-water-polymer data gave general average agreement with the trend followed by the air-water data, but showed a degree of scatter in the frictional component at gas Reynolds numbers equal to 9.69×10^4 and 11.9×10^4 and superficial liquid velocities of 0.552 m/s and 0.294 m/s respectively. These points are indicated in Figure 4.13 as "1" and "2" respectively. In fact, as shown in Figures 4.15, 4.16 and 4.17, there was an accentuated rise in pressure during the experiments at those flow rates. For instance, it can be observed in Figure 4.15 that P_6 steadily increased with increasing the gas flow rate, but changed suddenly at the last gas Reynolds numbers for superficial liquid velocities of 0.552 m/s and 0.294 m/s respectively. This disruption of the trend by those data points is indicated with a discontinuous line in the figures. However, this was not so for the pressures obtained at a superficial liquid velocity of 0.417 m/s, suggesting that abnormal behavior might have occurred at the highest gas flow rates for superficial liquid velocities of 0.552 m/s and 0.294 m/s. Also, a change in flow regime could have occurred at those conditions; unfortunately, no visual observations were done during the experiments.

The overprediction of the frictional pressure gradient for the air-water-polymer flow at those conditions appears to arise from fluctuations in the back pressure affecting the rest of the pressures and the measured pressure gradient to some extent. This confounding effect could have been avoided by controlling the

pressure in the separator. A possible explanation for this effect is presented in Section 4.3.

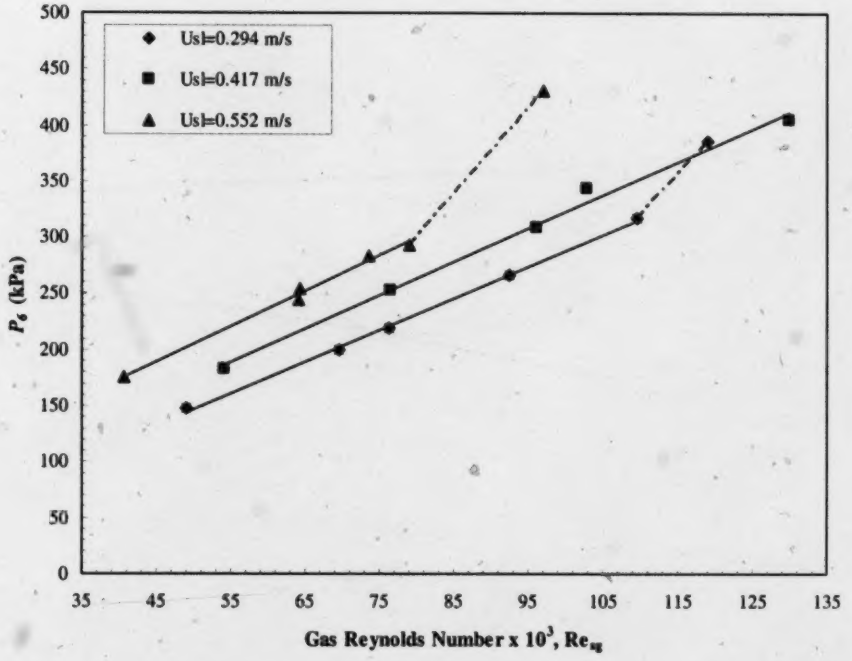

Figure 4.15: Variation of the measured pressure P_6 with the gas flow rate. The data points are connected by a linear fit.

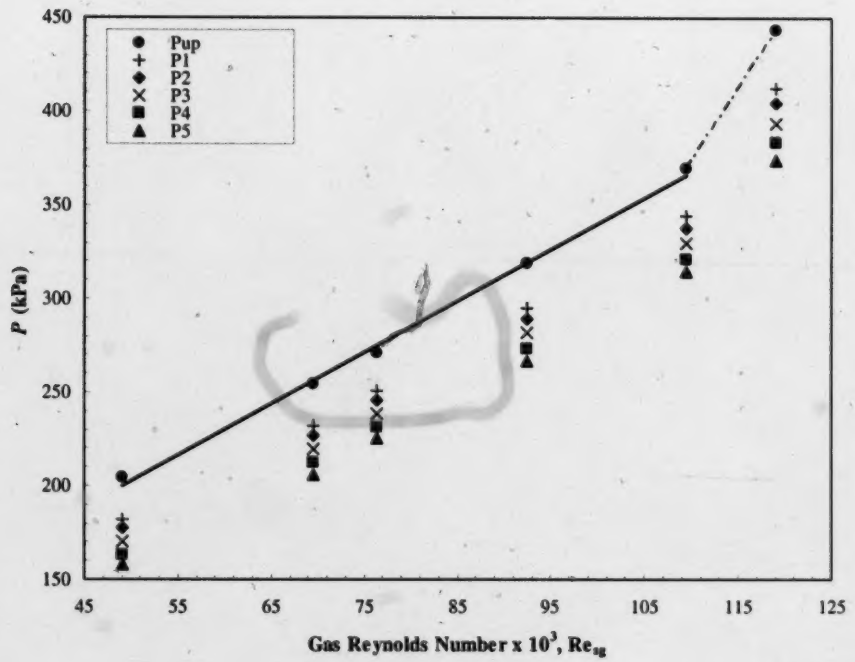

Figure 4.16: Variation of the measured pressures with the gas flow rate at a superficial liquid velocity of 0.294 m/s. The data points are connected by a linear fit.

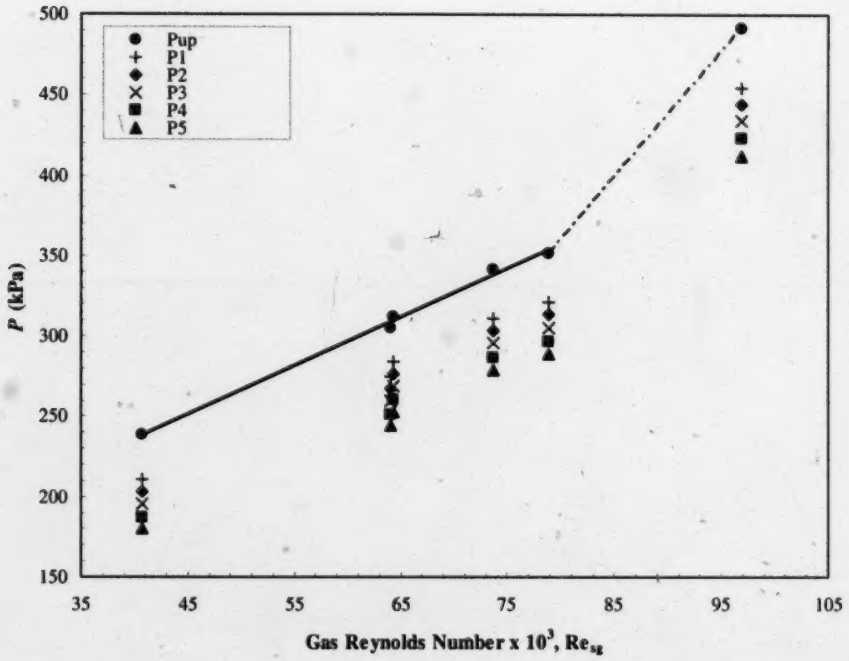

Figure 4.17: Variation of the measured pressures with the gas flow rate at a superficial liquid velocity of 0.552 m/s. The data points are connected by a linear fit.

4.2.4 Friction Factors

An understanding of the measurements of drag reduction can be obtained from a consideration of friction factors defined as in Equation 3.12:

$$f = \frac{D}{2\rho_g U_{sg}^{\ 2}} \frac{dP}{dx}$$

where *dP/dx* is the frictional pressure gradient calculated by subtracting the hydrostatic head from the overall pressure gradient. This holds for vertical annular two-phase flows where the acceleration term is negligible.

Figure 4.18 shows the friction factors obtained for the series of experiments with the air-water system and air-water-polymer system. For a fixed liquid flow rate, the *f* for the air-water flow decreases with increasing U_{sg}. This probably occurs because as the gas flow rate increases the entrained liquid, *E*, increases and the flow rate in the wall film decreases. The friction factor, therefore, decreases. Thus, these results indicate that *f* for the air-water system is primarily a function of the flow rate in the liquid film and, secondarily, a function of U_{sg}.

The friction factors obtained for the air-water-polymer system show a much smaller change with U_{sg} and U_{sl} than what is observed for the air-water system. However, a remarkable drop in *f* can be observed with the addition of the polymer. Reductions of up to 82% were thus obtained as shown in Figure 4.19.

These results clearly demonstrate the drag reducing effect of the polymer additive. In general, the drag reduction increased with increasing the liquid flow rate and decreased with increasing the gas flow rate. This result is consistent with the findings of Al-Sarkhi and Hanratti (2001a,b).

As discussed previously, fluctuations in the pressures during experiments are once again reflected in Figures 4.18 and 4.19 at gas Reynolds numbers equal to 9.69×10^4 and 11.9×10^4 and superficial liquid velocities of 0.552 m/s and 0.294 m/s respectively (the same two tests discussed before and indicated by "1" and "2").

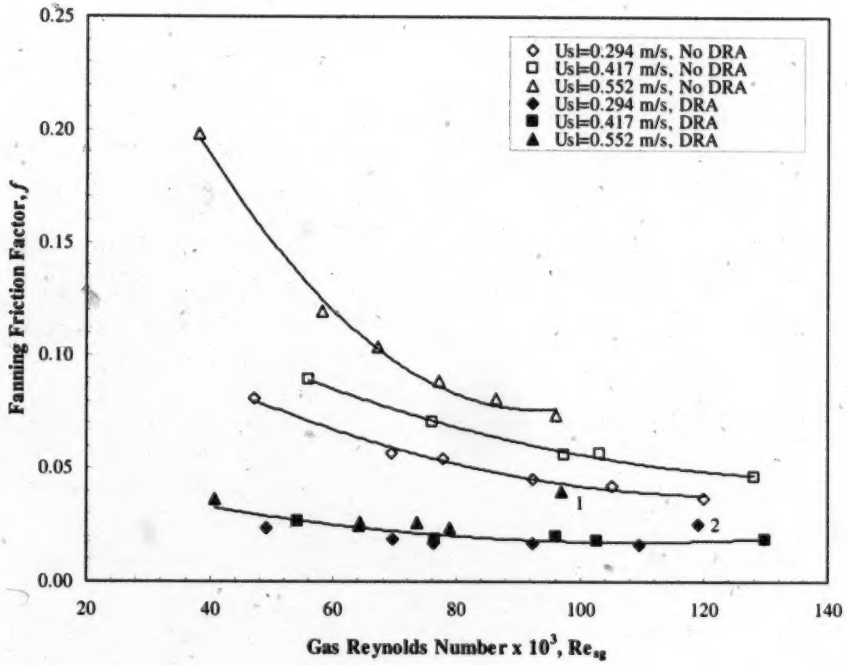

Figure 4.18: Comparison of friction factors obtained for the air-water system and air-water-polymer system. The data points were fitted to a polynomial of second order.

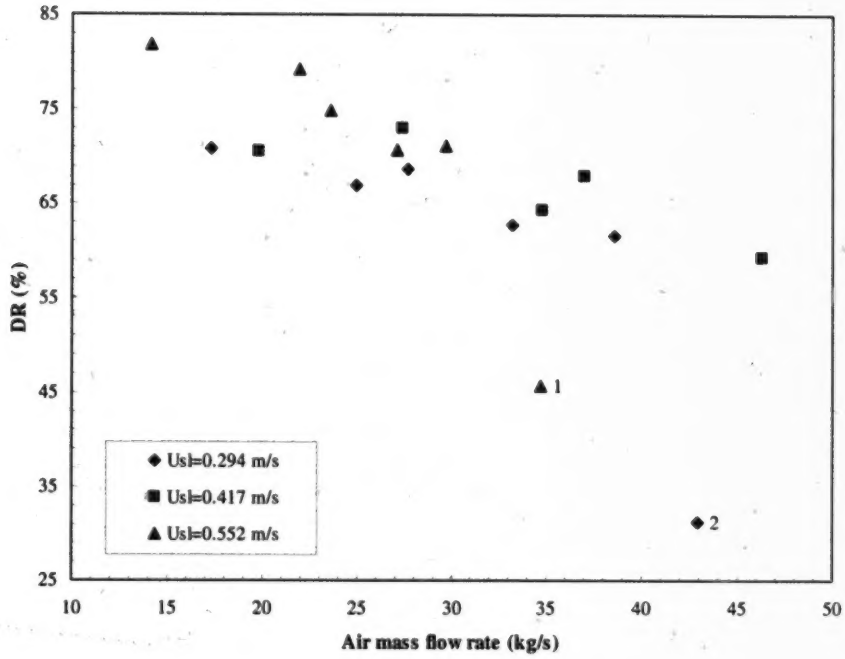

Figure 4.19: Effectiveness of DRA at various gas and liquid flow rates.

4.3 Uncertainty Considerations

An attempt for computing the uncertainty in the results was done by inserting perturbations of the measured parameters into the model equations and calculating the changes that ensue. In general, as shown in Tables 4.3 and 4.4, for the worst case scenario an uncertainty of ±20% in the liquid holdup resulted in a ±7% uncertainty in drag reduction. Similarly, a ±20% uncertainty in pressure gradient resulted in ±7% uncertainty in drag reduction. However, the uncertainty in the measured pressure gradient could not have realistically been more than ±5%. The effect of the perturbations in the calculated parameters is summarized in Appendix D. Useful equations for further careful evaluation of propagation of uncertainties into the results are also provided in Appendix D.

				Uncertainty		
α_l		NO DRA	0.127	± 5%	± 10%	± 20%
		DRA	0.145			
f		NO DRA	0.081	±2%	±5%	±9%
		DRA	0.024	±6%	±13%	±25%
DR	%		70.9	±2%	±3%	±7%
dP/dx	Pa/m	NO DRA	4018	± 5%	± 10%	± 20%
		DRA	2568			
f		NO DRA	0.081	±7%	±15%	±29%
		DRA	0.024	±11%	±23%	±45%
DR	%		70.9	±2%	±3%	±7%

Table 4.3: Uncertainty in the drag reduction by perturbation of the liquid holdup and pressure gradient for gas and liquid flow rates of 17.3 g/s and 148 g/s respectively.

				Uncertainty		
α_l		NO DRA	0.087	± 5%	± 10%	± 20%
		DRA	0.093			
f		NO DRA	0.037	±1%	±2%	±4%
		DRA	0.026	±1%	±3%	±6%
DR	%		31.2	±1%	±2%	±4%
dP/dx	Pa/m	NO DRA	5173	± 5%	± 10%	± 20%
		DRA	4053			
f		NO DRA	0.037	±6%	±12%	±24%
		DRA	0.026	±7%	±13%	±26%
DR	%		31.2	±1%	±2%	±5%

Table 4.4: Uncertainty in the drag reduction by perturbation of the liquid holdup and pressure gradient for gas and liquid flow rates of 42.9 g/s and 148 g/s respectively.

4.4 Repeatability Tests

An attempt was made to evaluate the reproducibility of the results by repeating two of the tests performed at different polymer concentrations. The results are shown in Table 4.5 and Table 4.6 for concentrations of 100 and 120 ppm respectively. The initial test is indicated as Run 0. The blank sections in the table indicate that the measurement was not performed by the corresponding pressure transducer.

It can be seen that the large variation in the results of these repeatability tests is due to the fact that test conditions were very difficult to reproduce. Even though the air and liquid flow rates varied by 2.8% and 1.2% respectively, larger differences in the measured pressures can be observed when comparing these tests. The use of a pressure regulator in the air line allowed for control of the air flow rate by adjusting the upstream pressure. However, this pressure notably changed between the tests as can be observed in Tables 4.5 and 4.6. As would be expected, differences are also noted in the rest of the pressures.

An explanation for such a behavior may be sought based on the mechanism of operation of the gas-liquid separator. This vertically oriented vessel features a side inlet and a gas outlet located on the top. As the two-phase mixture emerges from the test section it enters an inlet nozzle and hits a deflector plate located

right after the inlet. This inlet device controls the momentum by redirecting the inlet stream and dissipating the energy of the inlet fluid. The gas rises while the liquid falls into the bottom of the vessel. Liquid retention is provided in the bottom section of the separator; sizing of this section is based on the liquid retention time. Liquid level is maintained by a float actuated controlled valve. This is illustrated in Figure 4.20. A critical problem may arise when the liquid level gets too high in the retention section. The float moves up enough to hit the sphere of the named "ball scrubber valve" so closing the gas nozzle located at the top. The discharge of gas stops and the pressure then rises in the separator. Since the pressure in the separator was not controlled during the experiments, fluctuations of this pressure could have a significant impact on the flow measurements. A detailed illustration of the separator provided by the manufacturer is presented in Appendix B.

In spite of the large scatter in the data, there appears to be closeness of agreement between the results obtained for the three last runs and four last runs in Tables 4.5 and Table 4.6 respectively. These tests show a variation in the calculated drag reduction of about 3.3% and 2.5% respectively; this standard deviation could have been less if more than four repeatability tests had been done.

Table 4.5: Summary of the repeatability tests for a polymer concentration of 100 ppm.

		Run 0	Run 1	Run 2	Run 3	Run 4
$\dot{m}_g$	(g/s)	33.3	34.0	33.9	34.2	35.9
$\dot{m}_l$	(g/s)	145	143	142	146	144
P_1	(kPa)	328	349	305	295	311
P_2	(kPa)	321	340	299	289	305
P_3	(kPa)	313	331	291	282	298
P_4	(kPa)	304	320	283	274	290
P_5	(kPa)	296	311	277	267	283
P_6	(kPa)	284	----	----	----	----
P_{up}	(kPa)	358.1	380.8	328.2	319.2	332.2
P_{diff}	(kPa)	1.98	1.95	2.24	2.35	2.48
dP/dx	(Pa/m)	3606	3869	2944	2914	2915
a_l		0.100	0.096	0.115	0.118	0.116
ρ_l	(kg/m^3)	998	998	998	998	998
ρ_g	(kg/m^3)	3.66	3.87	3.42	3.31	3.49
U_{sg}	(m/s)	18.0	17.4	19.6	20.4	20.3
U_{sl}	(m/s)	0.288	0.282	0.281	0.288	0.285
Hyd	(Pa/m)	1013	975.9	1157	1184	1160
$Fric$	(Pa/m)	2418	2720	1610	1545	1564
f		0.028	0.032	0.017	0.016	0.016
DR	(%)	38.6	30.7	61.9	65.0	65.9

Table 4.6: Summary of the repeatability tests for a polymer concentration of 120 ppm.

		Run 0	Run 1	Run 2	Run 3	Run 4
$\dot{m}_g$	(kg/s)	43.4	42.6	43.0	42.1	42.7
$\dot{m}_l$	(kg/s)	146	143	143	143	143
P_1	(kPa)	397	348	364	359	358
P_2	(kPa)	389	343	358	353	354
P_3	(kPa)	381	334	349	345	345
P_4	(kPa)	372	326	341	336	337
P_5	(kPa)	364	318	334	329	330
P_6	(kPa)	----	----	----	----	----
P_{up}	(kPa)	427.6	374.8	388.9	384.9	382.6
P_{diff}	(kPa)	2.83	3.10	3.05	2.95	3.05
dP/dx	(Pa/m)	3697	3166	3148	3121	2989
α_l		0.096	0.108	0.105	0.107	0.107
ρ_l	(kg/m^3)	998	998	998	998	998
ρ_g	(kg/m^3)	4.47	3.92	4.10	4.05	4.05
U_{sg}	(m/s)	19.2	21.4	20.7	20.5	20.8
U_{sl}	(m/s)	0.288	0.283	0.284	0.282	0.283
Hyd	(Pa/m)	976	1090	1066	1084	1084
$Fric$	(Pa/m)	2501	1850	1859	1820	1683
f		0.021	0.015	0.015	0.015	0.014
DR	(%)	47.0	63.1	62.0	61.6	65.1

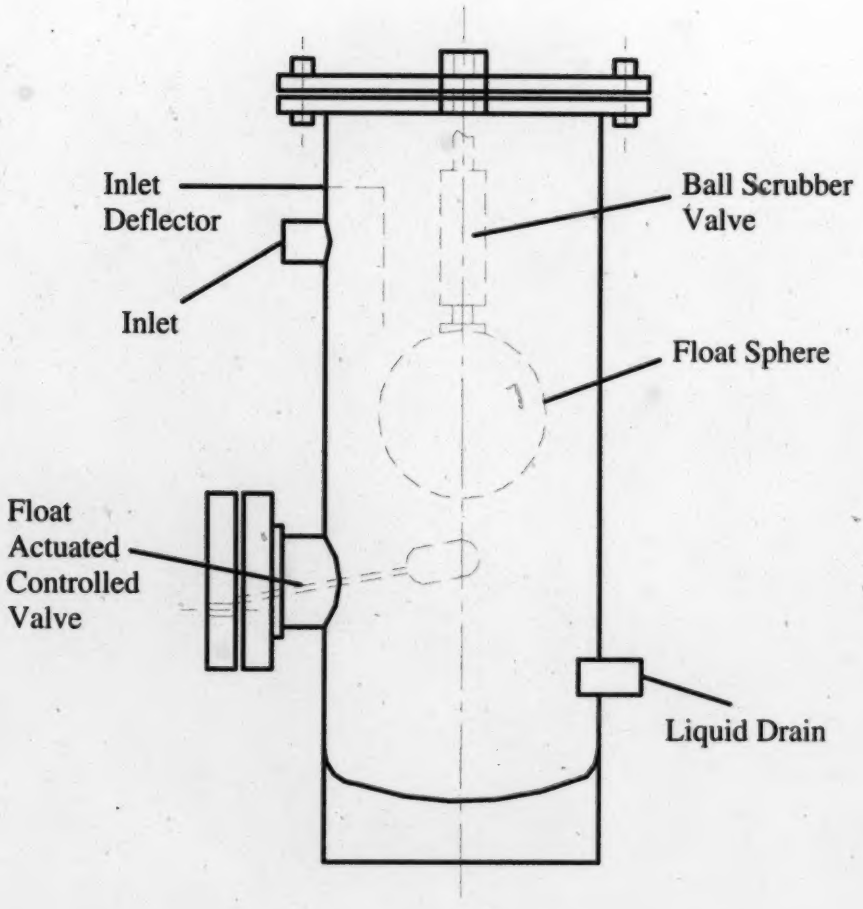

Figure 4.20: Schematic of the gas-liquid separator (not to scale)

4.5 DRA Polymer Degradation

Since the earliest work with polymeric DRAs, it has been known that their drag reduction effectiveness is reduced if mechanical energy is supplied to the polymers in solution (Manfield et al., 1999). Practically, this means that if a drag reduced liquid is passed through a pipe, pump, valve etc. then the drag reduction effect is diminished.

To determine the extent of degradation of the DRA, a number of tests were carried out using "flow-loop" operation in which the polymer solution was recirculated around the loop for approximately 50 minutes. Figure 4.21 describes the effectiveness of the degrading DRA solution as a decaying function of the time flowing through the system. These results were obtained at six gas and liquid flow rates with a polymer concentration of 60 ppm. The air flow rates used for these tests were higher than those presented previously due to the fact that no pressure regulator was installed in the air line yet. The pressure regulator introduced an additional pressure drop of about 83 kPa resulting in lower air flow rates.

The data points indicate similar trends in spite of the significant differences in the magnitudes of the observed DR. The initial 5-7 minutes witnesses a drop in DR and is due to the initial phase where steady flow is established and continuous

operation of the liquid/gas separator begins. After this, there tends to be a point of inflection followed by either a local maximum, or at least a clear peak in negative curvature (second derivative). This is when the flow has achieved steady state but the shear stresses acting on the fluid in the pump, tubing and separator have not begun to have a significant degradation on the long chain polymers in the DRA. From this point, it takes approximately 15 minutes for the DRA to be so degraded that it is completely ineffective.

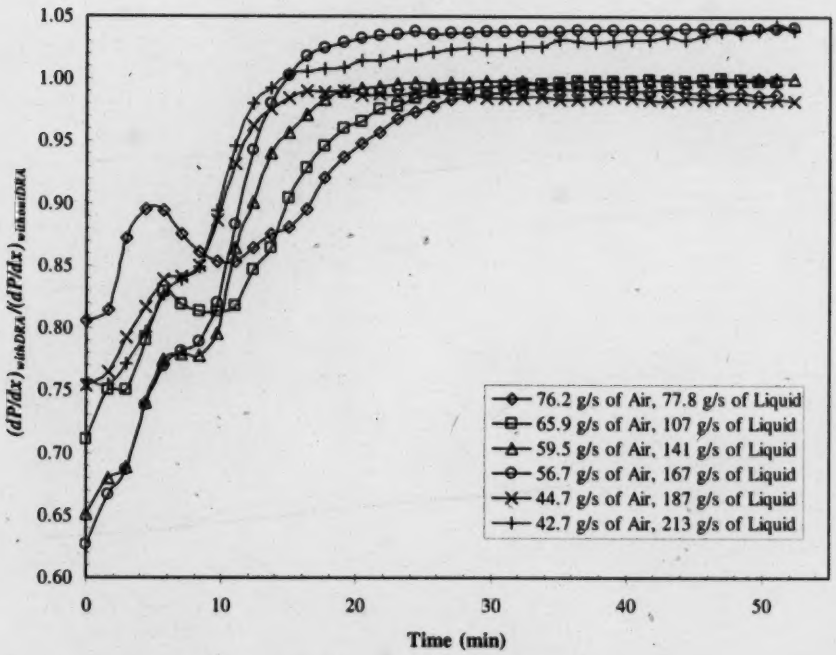

Figure 4.21: Ratio of the overall pressure gradients with and without DRA as a function of time for a polymer concentration of 60 ppm.

According to Manfield et al. (1999), the most rapid degradation of a DRA polymer takes place under the conditions of intense shear normally encountered in a centrifugal pump. It has been suggested that positive displacement pumps have a less severe effect (Manfield et al.,1999). Furthermore, the pump used in the experimental facility was a rotary vane positive displacement pump. The pumps of this type use a rotor with sliding vanes to draw the liquid in behind the vane, through the inlet port and into the pumping chamber. As the rotor turns, the liquid is transferred between the vanes to the outlet where it is discharged as the pumping chamber is squeezed down. This is illustrated in Figure 4.22. Vane contact with the chamber wall is maintained by three forces: centrifugal force from the rotor's rotation, push rods moving between opposing pairs of vanes, and liquid pressure entering through the vane grooves and acting on the rear of the vanes. This mechanism of operation and the sliding vane design minimize shear and agitation.

Therefore, it seems likely that appreciable degradation of the DRA took place in the separator. Given that the maximum pressure drop through the vertical pipe was found to be about 69 kPa between all the conditions being tested, the separator appears to be the last piece of equipment in the loop where the air might lose about 70% of its pressure before being vented to atmosphere. These high losses together with the mechanism of separation (explained previously in Section 4.4) could have had a significant degrading effect on the DRA.

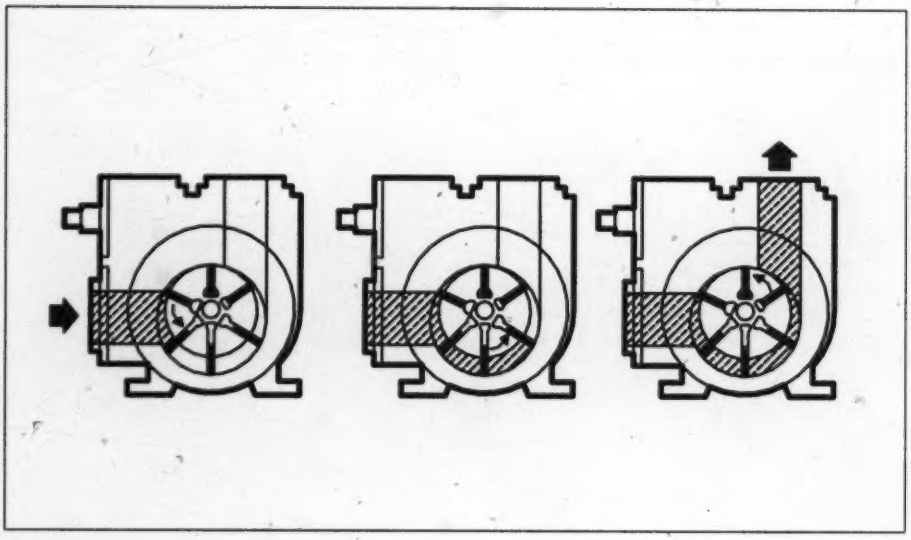

Figure 4.22: Mechanism of operation of a rotary vane pump

5 Conclusion

5.1 Conclusions

A study of the influence of a high molecular weight polymer on air-water annular flow in a vertical pipe has been presented. The main conclusions arising from this investigation are as follows:

1. Percol 727, a co-polymer of polyacrylamide and sodium-acrylate, has proved to be effective drag reducer for vertical annular air-water flow. Drag reductions between 31% – 82% were obtained at a polymer concentration of 75 ppm by mass in water.

2. Effectiveness of the DRA depends on the concentration of the polymer in the liquid phase so an optimum needs to be determined. Percol 727 showed to be effective at concentrations as low as 30 ppm. Maximum drag reductions were obtained for a polymer concentration of 75 ppm.

3. Drag reduction has been found to increase with increasing the liquid flow rate and decrease with increasing the gas flow rate. The latter effect suggests that the strong shearing action at the gas-liquid interface mechanically degrades the DRA.

4. For air-water flow, friction was found to be the dominant contributor to the pressure gradient at all air and water flow rates. Unfortunately, it was not possible to distinguish between the contributions from actual gas friction and friction from droplet deposition / entrainment. Gravity effects could not be ignored; in contrast, the accelerational pressure loss was found to be negligible.

5. Liquid holdup, film thickness and pressure loss are strongly interrelated and affected by the entrainment. Hence a good method for predicting liquid entrainment is necessary in order to develop reliable pressure drop predictions. Due to the high uncertainty associated with the values of entrainment obtained in this case for the air-water system, it was difficult to identify the most realistic results when comparing those values with the ones given by existing entrainment correlations.

6. The global effect of the DRA on the flow is a decrease in the frictional component of the pressure gradient and an increase in the holdup of liquid, which means there is potential in practical applications for lifting more liquid for a given bottom pressure, such as might be useful in liquid loaded gas wells.

7. The drag reduction effect has been shown to diminish over time as the additive degrades due to mechanical strain on the fluid. Since a rotary vane positive displacement pump was used, it is thought that degradation of the DRA mostly took place in the separator. Therefore, in commercial applications multiple injections are necessary if choke points occur in more than one pipeline segment.

5.2 Recommendations

Further recommended research work is as follows:

1. Future tests should be done with a more closely controlled back pressure to allow for better comparison between tests.

2. It is clear that the presence of small quantities of liquid has significant consequences for the operation of gas pipelines. Therefore, an accurate prediction of the liquid holdup is important in pipeline design, especially when "wet-gas" systems may be expected. It is recommended for further experiments the use of two quick-close valves in order to avoid an underestimation of the liquid holdup when only one valve is used.

3. In order to advance mechanistic models of multiphase drag reduction, experiments under a wide variety of conditions are needed. For the oil industry, vertical annular flow tests should be carried out in large diameter pipes (100 – 150 mm) at high pressure (5 – 10 MPa). Although in this industry often field data are available on pressure drop (e.g. gas wells), further characteristics such as liquid holdup, film thickness or liquid entrainment are much more difficult to obtain.

4. A fundamental understanding of the drag reduction phenomenon is a longer range endeavor. It will require advances in the understanding and modeling of turbulence as well as an understanding of the formation of molecular aggregates or molecular networks. Further experiments are also needed to investigate in more detail the phenomenon of suppression of entrainment with the addition of DRA.

5. Mechanistic models should be developed for the droplet entrainment / deposition process which can be implemented in two-fluid models for determining both the fraction of liquid entrained and the contribution of this process to the interface friction.

BIBLIOGRAPHY

Al-Sarkhi, A. and Hanratty, T. J., 2001a, "Effect of Drag-Reducing Polymers on Annular Gas-Liquid Flow in a Horizontal Pipe", International Journal of Multiphase Flow, 27, pp. 1151 – 1162.

Al-Sarkhi, A. and Hanratty, T. J., 2001b, "Effect of Pipe Diameter on the Performance of Drag-Reducing Polymers in Annular Gas-Liquid Flows", TransIChemE, 79.

Ansari, A. M., Sylvester, N. D., Sarica, C., Shoham, O. and Brill, J. P., 1994, "A Comprehensive Mechanistic Model for Upward Flow in Pipes", SPE Production & Facilities Journal, May, pp. 217 – 226.

Barbosa, J. R., Hewitt, G. F., König, G. and Richardson, S. M., 2002, "Liquid Entrainment, Droplet Concentration and Pressure Gradient at The Onset of Annular Flow in a Vertical Pipe", International Journal of Multiphase Flow 28, pp. 943 – 961.

Burger, E. D., Munk, W. R. and Wahl, Harry A., 1980, "Flow Increase in the Trans Alaska Pipeline using a Polymeric Drag Reducing Additive", Society of Petroleum Engineers, 55th Annual Fall Technical Conference and Exhibition, SPE 9419.

Foshee, W. C., Jennings, R. R. and West, T. J., 1976, "Preparation and Testing of Partially Hydrolyzed Polyacrylamide Solutions", Society of Petroleum Engineers, 51st Annual Fall Technical Conference and Exhibition, SPE 6202.

Gomez, L. E., Shoham, O., Schmidt, Z., Chokshi, R. N. and Brown, A., 1999, "A Unified Mechanistic Model for Steady-State Two-Phase Flow in Wellbores and Pipelines", Society of Petroleum Engineers, SPE 56520.

Ishii, M. and Mishima, K., 1989, "Droplet Entrainment Correlation in Annular Two-Phase Flow", Int. J. Heat Mass Transfer, 32(10), pp. 1835 – 1846.

Manabe, R., Tochikawa, T., Tsukuda, M. and Arihara, N., 1996, "Experimental and Modelling Studies of Two-Phase Flow in Pipelines", Society of Petroleum Engineers, SPE 37017.

Manfield, P. D., Lawrence, C. J. and Hewitt, G. F., 1999, "Drag Reduction with Additives in Multiphase Flow: A Literature Survey", Multiphase Science and Technology, 11, pp. 197 – 221.

Oliemans, R. V. A., Pots, B. F. M. and Trompé, N., 1986, "Modelling of Annular Dispersed Two-Phase Flow in Vertical Pipes", International Journal of Multiphase Flow, 12(5), pp. 711 – 732.

Oliemans, R. V. A., 2001, Applied Multiphase Flows, Delft University of Technology, Chap 4.

Panton, R. L., 1996, Incompressible Flow, John Wiley and Sons, New York, Chap 5.

Spedding P. L., Woods, G. S., Raghunathan, R. S. and Watterson, J. K., 2001, "Flow Regimes, Holdup and Pressure Loss for Two-Phase Flow Through Vertical and Near Vertical Tubes", Dev. Chem. Eng. Mineral Process., 9(3/4), pp. 371 – 388.

Sylvester, N. D. and Brill, J. P., 1976, "Drag Reduction in Two-Phase Annular-Mist Flow of Air and Water", AIChE J, 22, pp. 615 – 617.

Wallis, G. B., 1969, One-Dimensional Two-Phase Flow, McGraw-Hill, New York, NY.

White, F. M., 1994, Fluid Mechanics, McGraw-Hill, Chap 6.

Xueming, S. and Jianzhong, L., 2002, "Experimental Research on Drag Reduction by Polymer Additives", Canadian Journal of Chemical Engineering, 80(2), pp. 293 – 298.

A APPENDIX: Data Analysis

A.1 Spectral Analysis

It was possible to analyze a set of pressure data using discrete Fourier transform. Spectral analysis, based on discrete Fourier transform, was performed in order to detect the characteristic frequency of the noise not evident in time domain.

Each spectral coefficient was found based on:

$$a_k = \sum_{n=0}^{N-1} P(t_n) e^{\frac{2\pi k f_s t_n}{N} j} \qquad \text{(A.1)}$$

where

$P(t_n)$ is the set of regularly spaced pressure samples taken at times t_n (real numbers).

N is the total number of samples (chosen such that $N=2^m$ where m is some positive integer, thus allowing for "fast" transformation).

k is the index counter where $k = 0, 1, 2, \ldots N\text{-}1$

a_k is the set of complex coefficients.

f_s is the sample frequency (Hz)

$j = \sqrt{-1}$

The spectrum was then constructed using the norm of the complex coefficients. Figure A.1 shows the spectrum obtained from a set of pressures when only air was flowing along the pipe at a rate of 122 g/s. A peak of only 9.1 Hz was found to be the highest peak in the spectrum.

Low frequency noise is usually caused by a mechanical source or building vibrations. In order to determine whether or not the air compressor of the building was the source of the noise in the measured signal, a second set of data was recorded at static conditions. The spectrum obtained is shown in Figure A.2. Once again, a low frequency peak of approximately 9 Hz was obtained with no air or water flowing along the pipe. These results provided no evidence of noise coming from the compressor of the building.

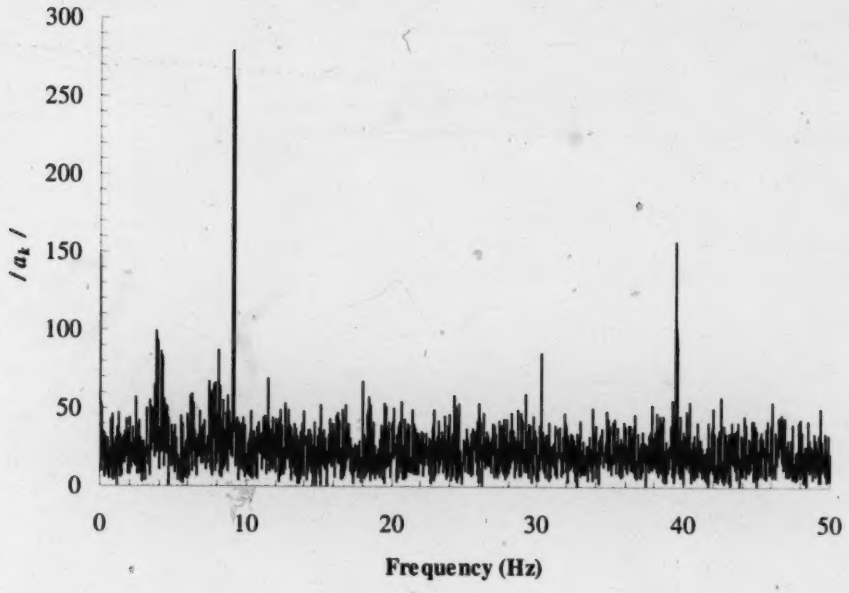

Figure A.1: Power spectrum corresponding to the recorded pressure signal P_1 when only air was flowing along the pipe at a rate of 122 g/s.

This Figure shows the first half of the norm of the complex coefficients obtained from the discrete Fourier transform of 4096 pressure measurements sampled at 100 Hz (sample duration of 40.96 seconds). The magnitude of the spectral coefficient associated with the 9 Hz peak was 8×10^{-2} % of the zero mode coefficient, and thus considered to have a negligible dynamic effect on flow behavior.

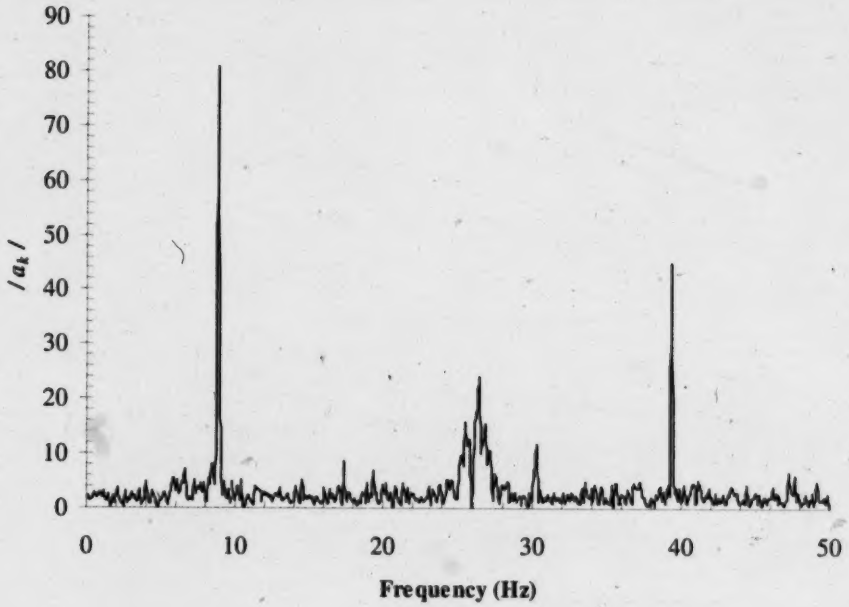

Figure A.2: Power spectrum corresponding to the recorded pressure signal P_1 at static conditions.

A.2 Calculation of the Air Flow Rate

An orifice plate was designed and constructed to measure the air flow rate. It had a hole diameter d_t of 20.3 mm and two pipe-wall taps at D upstream and ½ D downstream.

The equation of the orifice plate was derived from the general relation for a Bernoulli obstruction meter:

$$Q = C_d A_t \left[\frac{2(P_{up} - P_{down})/\rho}{1-\beta^4} \right]^{1/2} \qquad \text{(A.2)}$$

where:

Q	Volumetric flow rate
C_d	Dimensionless discharge coefficient
A_t	Area of the throat of the obstruction
P_{up}	Pressure upstream the orifice plate
P_{down}	Pressure downstream the orifice plate
ρ	Fluid density

The β ratio of the device was found to be 0.8 from the relation:

$$\beta = \frac{d_t}{D} \qquad \text{(A.3)}$$

The discharge coefficient C_d was determined as follows:

- An experimental run was performed with only air flowing at the maximum upstream pressure of 610.7 kPa. Sample data are shown in Table A.1. An

average differential pressure P_{diff} of 15.7 kPa was obtained across the orifice plate.

- The fluid density ρ was calculated by the ideal gas law:

$$\rho_g = \frac{P_{up}}{RT} \tag{A.4}$$

where the temperature T and the gas constant R were assumed to be 293.15 K and 287 J/kgK respectively.

- A velocity $U_{assumed}$ was first assumed.

- The Reynolds number Re_D was calculated as:

$$\mathrm{Re}_D = \frac{\rho U D}{\mu} \tag{A.5}$$

A viscosity of 1.8×10^{-5} Nm/s^2 was assumed.

- The discharge coefficient C_d was calculated by using the curve-fit formulas recommended by ASME (White, 1994). The basic form of the curve fit is:

$$C_d = f(\beta) + 91.71\beta^{2.5}\,\mathrm{Re}_D^{-0.75} + \frac{0.09\beta^4}{1-\beta^4}F_1 - 0.0337\beta^3 F_2 \tag{A.6}$$

where $f(\beta) = 0.5959 + 0.0312\beta^{2.1} - 0.184\beta^8$ (A.7)

The correlation factors F_1 and F_2 vary with tap position. For taps located at D upstream and ½ D downstream:

$F_1 = 0.4333 \qquad F_2 = 0.47$

- The area of the throat A_t was calculated as:

$$A_t = \frac{\pi}{4} d_t^{\,2} \tag{A.8}$$

- The volumetric flow rate Q was calculated from the Equation A.2 where $P_{up} - P_{down} = P_{diff}$; P_{diff} is the differential pressure across the orifice plate.

- The velocity is calculated as:

$$U_{calculated} = \frac{Q}{A} \tag{A.9}$$

where the area of the pipe A is given by:

$$A = \frac{\pi}{4} D^2 \tag{A.10}$$

- An iteration tool was used to do all the calculation steps described above by varying the input velocity value until $U_{assumed} = U_{calculated}$

Thus, the maximum velocity for air flowing alone in the pipe was found to be 33.27 m/s and the discharge coefficient was determined to be 0.607.

Then Equation A.2 becomes:

$$Q = 1.969 \cdot 10^{-4} \sqrt{\frac{972.2\, T\, P_{diff}}{P_{up}}} \tag{A.11}$$

The mass flow is related to Q by:

$$\dot{m} = \rho Q \tag{A.12}$$

Therefore, the mass air flow rate was calculated as:

$$\dot{m}_g = 1.969 \cdot 10^{-4} \sqrt{\frac{972.2\, T\, P_{diff}}{P_{up}}} \frac{P_{up}}{287\, T} \tag{A.13}$$

where P_{diff} and P_{up} are in Pascals and T in Kelvins.

Table A.1: Sample data and calculated flow rate for an air test at the maximum upstream pressure.

Date of the test	04/11/03
Room T (°C)	20
$\dot{m}_g$ (g/s)	122
$\dot{m}_l$ (g/s)	0
scan rate (scans/s)	100

Time (s)	P_1 (kPa)	P_2 (kPa)	P_3 (kPa)	P_4 (kPa)	P_5 (kPa)	P_6 (kPa)	P_{diff} (kPa)	P_{up} (kPa)	$\dot{m}_g$ (g/s)
1	587	583	577	572	567	559	15.7	611.1	122
2	587	583	577	572	566	559	15.7	611.1	122
3	587	583	577	571	566	559	15.8	611.0	123
4	587	583	577	571	566	559	15.7	611.0	122
5	587	582	578	571	566	559	15.7	611.1	122
6	587	582	577	571	566	559	15.7	611.0	122
7	587	582	577	572	567	559	15.7	610.9	122
8	587	583	577	571	566	559	15.7	611.0	123
9	587	583	577	571	566	559	15.7	610.8	122
10	587	582	577	571	566	559	15.7	610.8	122
11	587	582	577	571	566	558	15.8	610.7	123
12	587	582	577	571	566	559	15.8	610.7	123
13	587	582	577	571	566	558	15.8	610.7	123
14	587	582	577	570	565	559	15.7	610.6	122
15	587	582	577	571	566	558	15.7	610.8	122
16	586	582	578	571	565	558	15.6	610.5	122
17	586	582	576	571	565	559	15.7	610.2	122
18	586	582	576	570	565	558	15.6	610.1	122
19	586	582	576	570	565	558	15.6	610.1	122
20	586	581	576	570	565	558	15.7	610.0	122
Average	**587**	**582**	**577**	**571**	**566**	**559**	**15.7**	**610.7**	**122**
Stdev(±)	0.4	0.5	0.4	0.6	0.6	0.4	0.1	0.3	0.2

A.3 Calculation of the Liquid Flow Rate

The Annubar flow meter was calibrated by measuring the exact weight of water delivered for a given period of time. This was done for 12 flow rates (including 1 repeatability test) up to the maximum speed of the pump.

A chronometer was used to measure the time during which the sample was collected. The signal sensed by a Valydine pressure transducer was recorded in the form of voltage on the PC data acquisition system. The mass flow rate was then calculated by dividing the weight of the sample by the time of sampling. Table A.2 shows the data found during these tests and Figure A.3 shows the calibration curve of the liquid flow meter.

Table A.2: Annubar Calibration data

Weight of water (kg)	Test #	Time (s)	Flow Rate (kg/s)	Average voltage (V)	Stdev (±V)
8	1	254	3.15E-02	0.057	0.050
	2	176	4.56E-02	0.130	0.006
	3	130	6.16E-02	0.248	0.006
	4	103	7.73E-02	0.404	0.009
	5	86.9	9.21E-02	0.547	0.009
	6	72.9	1.10E-01	0.777	0.013
	7	53.0	1.51E-01	1.463	0.023
	8	47.8	1.68E-01	1.826	0.031
	9	42.6	1.88E-01	2.297	0.032
	10	37.9	2.11E-01	2.936	0.046
	11	32.4	2.46E-01	3.842	0.083

Repeatability uncertainties of ± 0.034 V and ± 2.16 g/s were obtained.

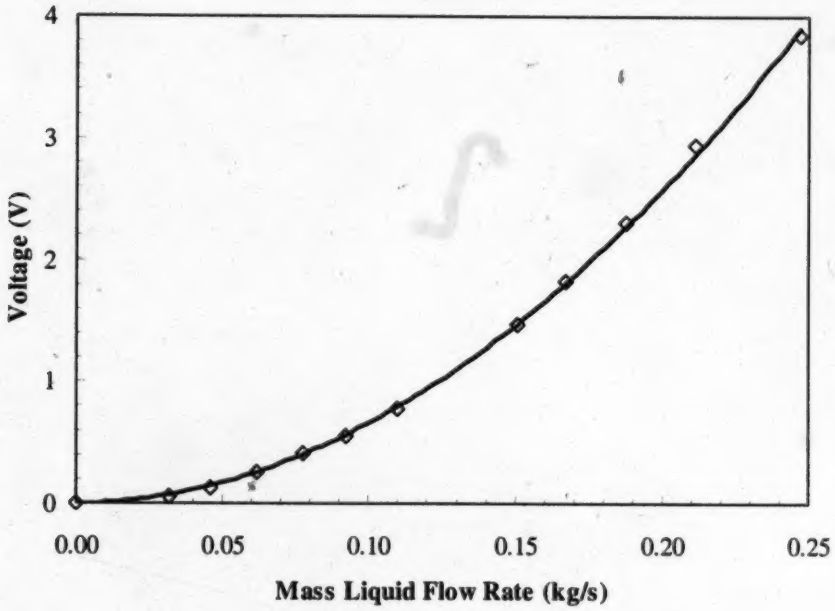

Figure A.3: Calibration Curve of the Liquid Flow Meter. The curve was fitted to a polynomial of second order.

The calibration curve obtained is of the form:

$$V = 62.395\dot{m}_l^{\,2} + 0.370\dot{m}_l \qquad \text{(A.14)}$$

where the voltage V is in volts (V) and the mass liquid flow rate $\dot{m}_l$ is in (kg/s).

From Equation A.14, the liquid flow rate can be written as:

$$\dot{m}_l = \frac{-0.370 + \sqrt{0.137 + 249.580\,V}}{124.790} \qquad \text{(A.15)}$$

where $V \geq 0$

Equation A.15 was then used to calculate the liquid flow rate for every run.

A.4 Single Phase Test

A single phase air test was performed to check the reliability of the data obtained in the constructed experimental setup.

Figure A.4 illustrates the measured pressures plotted as a function of the position along the pipe where zero is defined as the location of the first pressure transducer. The points in the plot correspond to the average pressures reported in Table A.1.

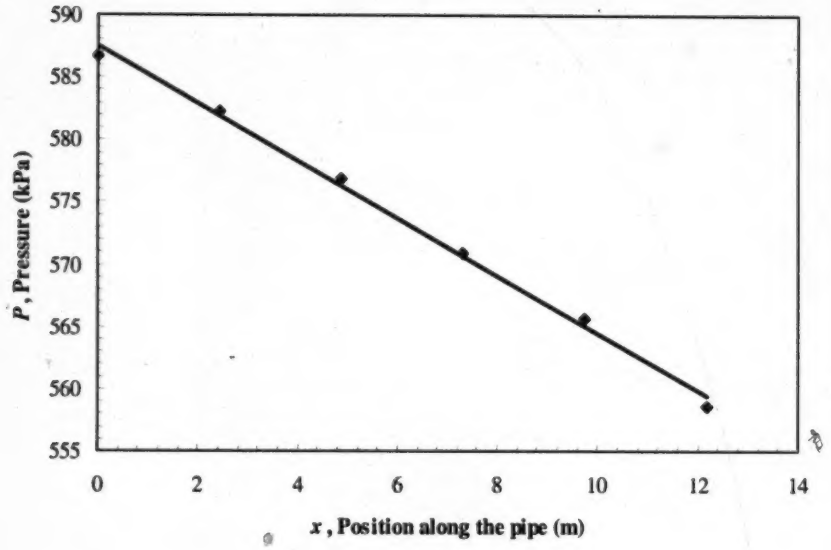

Figure A.4: Pressure as a function of the position along the pipe. The data points are connected with a linear fit.

The pressure gradient *dP/dx* was taken as the slope of the linear regression line through the data points:

$$P = -2.30x + 587.55 \qquad \text{(A.16)}$$

where P is in kPa and x is in m.

$$\frac{dP}{dx} = -2.30 \text{ (kPa/m)}$$

The friction factor was then calculated by using the Darcy-Weisbach equation:

$$f = \frac{2D}{\rho U^2}\left(\frac{dP}{dx}\right) \qquad \text{(A.17)}$$

where:

f friction factor

D Pipe diameter

ρ Fluid density

U Fluid velocity

$\left(\frac{dP}{dx}\right)$ Pressure gradient

The air velocity was given by:

$$U = \frac{\dot{m}_g}{\rho A} \qquad \text{(A.18)}$$

where A is the cross sectional area of the pipe.

The density of the air was calculated from Equation A.4 by using the measured pressure upstream the orifice plate. A value of 7.26 kg/m^3 was obtained.

From Equation A.17 the friction factor was found to be 0.015. This value was compared to the one given by the Moody chart for a pipe with smooth walls. An average deviation of 5% was obtained.

B APPENDIX: Equipment and Instrumentation

The following table presents the characteristics of the experimental equipment.

Table B.1: Equipment specifications

Designation	Model	Size	Specifications
Polycarbonate tubing		1" ID length of each section: 8'	1/8 wall thickness Max. pressure: 560 Psi
Pump	CB2507X PROCON Rotary brass vane model		Desired flowrate: 240GPH Positive displacement Pressure range: 151-250 Psi Setting for relief valve pressure: 170 Psi Variable frequency drive unit
Separator		10"OD and 29" height	Fuel gas scrubber with automatic drain
Pressure Transducers	OMEGA PX603 for connector		0.4% Accuracy Range: 0-100 Psig Full conditioned: 1-5V Output
Orifice Plate	Constructed at the U of A Mechanical Engineering Machine Shop	Line size: 25.4 mm ID Hole diameter: 20.3 mm	
Liquid Flow Meter	Annubar DNT/10S	Line size: 3/4" ID	
Data Acquisition System	National Instruments NI PCI-6070E		12 bits 16 single-ended or 8 differential (software-selectable per channel)

Designation	Model	Size	Specifications
Validynes connected to the orifice Plate			Upstream pressure Diaphragm: 0-5 V 0-100 Psi Differential pressure across the plate Diaphragm: 0-5 V 0-10 Psi
Validyne Connected to the Annubar			Diaphragm: 0-10 V 0-1 Psi
Validyne Demodulators	Model CD15 Carrier Demodulator		
Tensiometer	DuNouy Tensiometer	1" diameter ring	
Viscometer	Cone/Plate LVT Digital Viscometer Spindle used: CP-40	Cone radius: 2.4 cm Angle: 0.8°	Guaranteed to be accurate to within 1% of whatever full scale range is employed. Range for a cone CP-40 is presented in Table B.2

Table B.2: Range of viscosities for a spindle CP-40

Speed (RPM)	Shear rate (sec^{-1})	Cone # CP-40 μ (cps)
60	450	5.14
30	225	10.28
12	90	26
6	45	51
3	22.5	103
1.5	11.25	206
0.6	4.5	514
0.3	2.25	1,028

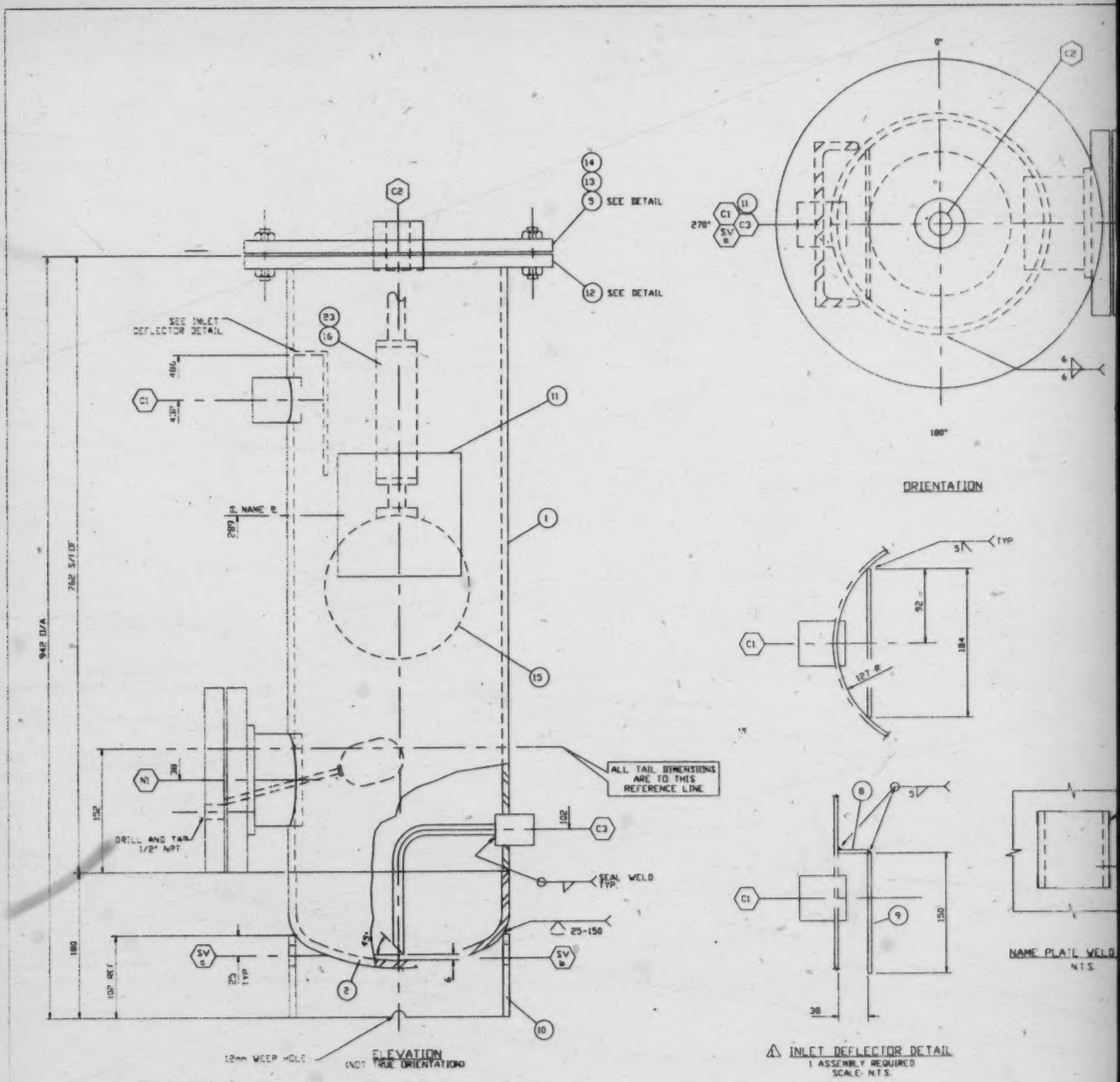

MARK	QTY	SERVICE	SIZE	RATING	TYPE	PIPE SCH WALL THK	REPAD	PROJ'N	O/S	WELD DETAIL	A	B	C	ITEM NO'S
SV a	2	SHUT VENT	1" Ø	HOLE										
23	1	SYPHON DRAIN	1/8"	6000#	CPLG	NPT		MIN	MAX	4	3/8"			6,7
22	1	OUTLET	11	6000#	CPLG	NPT		3/4"	MAX	SEE DTL	1/2"	1/2"		22
21	1	INLET	11	6000#	CPLG	NPT		MIN	MAX	4	3/8"			3
N1	1	CONT DRAIN	4"	1500	W/SOCKET	XH		MIN	3"	6.7	3/8"			17,18,19,20,21

NOZZLE SCHEDULE

NOTES:
1. ALL FLANGES ARE TO ANSI B16.5 AND ALL NPT TO ANSI B21.
2. UNLESS OTHERWISE NOTED ALL WELDMENTS TO STRADDLE THE NATURAL CENTERLINES OF THE VESSEL.
3. SHELL AND HEAD MUST NOT EXCEED 3/8" THK PER UW-16(F)(2)a)
4. SA-106-B MATL CAN BE REPLACED WITH SA-333-GR6
SA-105N MATL CAN BE REPLACED WITH SA-350-LF2
5. TACKWELDS AND ATTACHMENTS SEE CHART

CIRC SEAMS	LONG SEAMS	REINFORCED NOZZLES THRU SHELL OR HEAD	CPLG THRU SHELL OR HEAD
1	2	3	4
WPS SEE CHART	WPS	WPS	WPS SEE CHART
NDE NONE	NDE	NDE	NDE

Drawing 41907-[illegible] / Tag 1945 / User [illegible]

Figure B.1

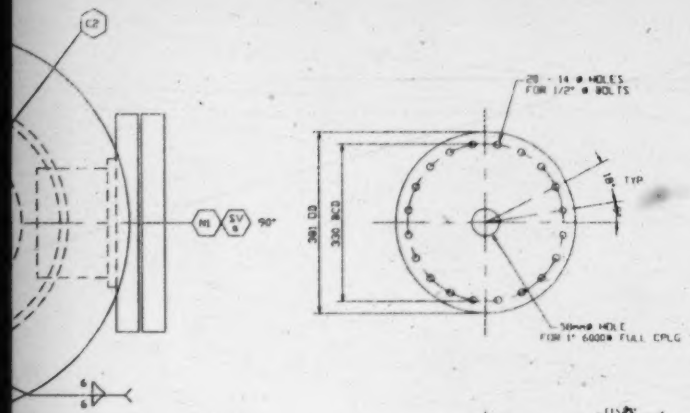

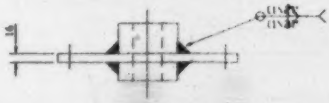

ITEM 5 DETAIL
1 REQUIRED
SCALE: N.T.S.

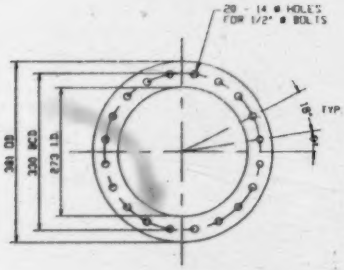

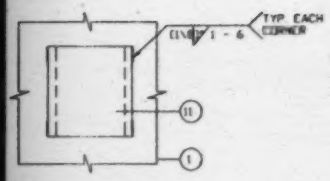

ITEM 12 DETAIL
1 REQUIRED
SCALE: N.T.S.

NAME PLATE WELD DETAIL
N.T.S.

MATERIAL LIST

ITEM	QTY	PART	DESCRIPTION	MATERIAL
1	1	2500100	10" STD SMLS PIPE x 752 LG.	SA-106-B
2	1	2500200	10" STD WELD CAP	SA-234-WPB
3	1	50710023	1" - 6000# F.S. FULL SCR'D CPLG. x 60 LG.	SA-105N
5	1	16106251	5/8" PL. x 381 O.D. - SEE DETAIL	SA-516-70
6	1	50704017	1/2" - 6000# F.S. FULL SCR'D CPLG. x 48 LG.	SA-105N
7	1	130200419	1/2" STD. SMLS PIPE x 305 LG.	
			- BEND TO SUIT	SA-106-B
8	1	16001875	3/16" PL. x 184 x 39	SA-516-70
9	1	16001875	3/16" PL. x 150 x 184	SA-516-70
10	1	13602512	10" SCH STD. PIPE X 102 LG.	SA-106-B
11	1	48726200	NATCO NAME PL.	SS
11	1	48726203	NATCO STD. NAME PL. BRACKET	SA-36
12	1	16106251	5/8" PL. x 381 O.D. x 273 I.D. - SEE DETAIL	SA-516-70
13	1	47701114	GASKET: 1/8" THK x 381 O.D.	
			c/w 20-14 DIA. HOLES ON 330 BCD	GB
14	20	2501400	STUD 1/2" X 2 1/2" LG.	SA 193 B7
14	40	65089299	NUT 1/2" DIA.	SA 194 2H
15	1	64334331	FLOAT BALL 8" SPHERE w/1/2" NPT	NIC PL.
16	1	45001520	INVALCO BALL, SCRUBBER VALVE	
17	1	13021439	4" XH SMLS PIPE x 105 LG.	SA-106-B
18	1	2501800	4"-150# RFSO FLG.	SA-105
19	1	47259016	4"-150# RF GASKET	316 SS
20	1	31320010	4"-150# RF BLIND FLG.	SA-105
21	8	2502100	5/8" DIA. STUD x 3 1/2" LG.	SA-193-B7
21	16	65089399	5/8" DIA. NUT	SA-194-2H
22	1	50710023	1" - 6000# F.S. FULL SCR'D CPLG. x 60 LG.	SA-105N
23	1	80000021	VLCD VALVE SCRUBBER IC-125	

DESIGN DATA

CODE: ASME SECTION VIII, DIV. 1, 98 EDITION X ADDENDA PARAGRAPH UG-12(c)

IMPACT TEST EXEMPTION PER UG-20(f) "UM" STAMP REQUIRED NO

C.R.N. N-3019.213 FROM DWG. RD-2510-00 SERIAL No. SEE STAMP-25

	D.P.	MAWP	M & C	HYDRO TEST
INTERNAL PRESSURE PSI/kPa.	150 / 1034			225 / 1551
EXTERNAL PRESSURE PSI/kPa.		-	-	-
TEMPERATURE °F/°C	200 / 93	-	-	60 / 16
M.D.M.T. °F/°C	-20 / -29	-	-	
LIMITED BY	DESIGN	-	-	

CORROSION ALLOWANCE INCH/mm	NONE	RADIOGRAPH	NONE
LONG JOINT EFFICIENCY	1.0	CIRC. JOINT EFFICIENCY	0.70
P.W.H.T. PER UCS-56	NONE	VOLUME	165 CuFT / 0.05 CuM
SHIPPING WEIGHT	90 lbs / 41 Kg		
HYDRO TEST WEIGHT	125 lbs / 58 Kg		

	MATERIAL	THICKNESS	TYPE
SHELL	SA-106-B	0.319" MIN. SEE NOTE #3	SMLS PIPE
FLANGE	SA-516-70	0.625"	FLANGE
BOTTOM HEAD	SA-234-WPB	0.319" MIN. SEE NOTE #3	WELD CAP
WELD PROCEDURES	327.2	SOURCE DRAWING	-

JOINT	WELD PROCEDURE
CIRC. SEAMS	AFC-10/M2 REV.4 M3 REV.5/M2 REV.3 AI REV.1
CPLG. THRU SHELL/HEAD	AFC-10/M2 REV.4 M2 REV.5/M2 REV.3
FLANGE TO PIPE	AFC-10/M2 REV.4 M3 REV.5/M2 REV.3 AI REV.1
TACKWELDS & ATTACHMENTS	M2 REV.3/M3 REV.5

REV	DATE			DESCRIPTION
5	07/28/97	LTV	-	UPDATE TO 1995 EDITION, A96 ADDENDA
4	11/27/96	[illegible]	BS	REVISED ITEM 14 & 21
3	11/18/96	[illegible]	BS	REV. VESSEL CORR. ALLOWANCE TO 0", REV. TOP ACCESS FLANGE
2	10/17/96	LJV	BS	ITEM #23 ADDED, VOLUME CORRECTED
1	09/12/96	FW	BS	ADDED 1" 6000# FULL CPLG TO BLIND FLANGE
6	FEB 9/99	GSN	-	REVISED & RELOCATED NAME PLATE (ITEM #11)

REVISIONS

This drawing is the property of NATCO CANADA Ltd. and is lent to the recipient for his confidential use only, in consideration of the loan of this drawing, the recipient promises and agrees that it shall not be used in any way detrimental to the interests of NATCO CANADA Ltd., that it shall be returned upon request, and that it shall not be reproduced, copied, lent or otherwise disposed of, directly or indirectly, without the written approval of NATCO CANADA Ltd.

REFERENCE DRAWINGS

	CPLG. THRU SHELL OR HEAD	CPLG THRU BLIND FLANGE	NOZZLE THRU SHELL OR HEAD	SLIP-ON FLANGE	FLANGE TO PIPE	
	4	5	6	7	8	9
WPS	SEE CHART	SEE CHART	SEE CHART	SEE CHART	SEE CHART	
NDE	-	-	-	-	-	

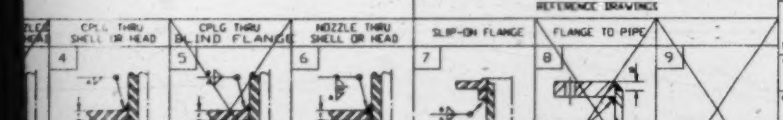

NATCO CANADA Ltd.

CALGARY ALBERTA CANADA

TITLE: FUEL GAS SCRUBBER
10 3/4"/273mm O.D. x 2'-5"/737mm S/S

CUSTOMER: NATCO STANDARD

LOCATION: -

DRAWN: FRANK V DATE: 07/24/96
CHK: - SCALE: 4"=1'-0"

CUST. REF. NO.: - SHOP ORDER NO.: SEE STAMP UNITS: - DRWG. NO.: 41907-25 REV: 6

CALGARY REF. DRAWING SD2510001.DWG

C APPENDIX: Test Conditions and Fluid Properties

C.1 Test Conditions

The experimental conditions are summarized in Table C.1.

Table C.1: Experimental conditions

D (mm)	25.4
A (mm^2)	506.7
L (m)	12.2
P_{sep} (kPa)	200 - 576
T (°C)	20
$\dot{m}_g$ (g/s)	14.2 – 46.3
$\dot{m}_l$ (g/s)	148 - 278
U_{sg} (m/s)	8.58 -20.1
U_{sl} (m/s)	0.294 - 0.552

C.2 Physical Properties of the Fluid Systems

The thermophysical properties of the fluids used are listed in Table C.2.

Table C.2: Properties of the fluids used at 20 °C

Property	Fluid			Comments
	Air	Water	Polymer Solution	
ρ (kg/m^3)	2.6 - 5.8	998	998	
σ (N/m)		0.073	Function of concentration of the polymer	Measured values are presented in Section C.2.2
μ (Nm/s^2)	1.8E-05	1E-03	Function of shear rate and concentration of the polymer	Measured values are presented in Section C.2.3

C.2.1 Density

For the liquid phase, the density of the water was taken as the tabulated value at standard conditions (P=101.3 kPa and T=20°C).

Since experiments with the air-polymer solution system were done at low polymer concentrations, the density of the polymer solution was assumed to be the same as for water.

For the gas phase, the density was assumed as the density of the air in the middle of the test section. The density of the air at each position in the pipe was calculated by using the ideal gas law (Equation A.4):

$$\rho_{air} = \frac{P}{RT}$$

where the gas constant R has a value of 287 J/kgK for air.

The calculated values were plotted as a function of the position along the pipe. The density of the air at the midpoint was then estimated by using the equation of the linear regression line through the data points.

C.2.2 Surface Tension

For the air-water system, the surface tension was taken as the tabulated value for water at standard conditions.

For the air-polymer solution system, the surface tension of the polymer solution was measured at different concentrations by using a DuNouy Tensiometer. All the measurements were done at atmospheric conditions and the results are presented in Table C.3. It is noted that the surface tension of the polymer solution has a negligible variation with concentration over the range of polymer concentrations studied.

Table C.3: Surface tension of the polymer solution at standard conditions

Sample #	Concentration (ppm)	Surface tension (N/m)
1	30	0.0679 ± 0.0005
2	50	0.0680 ± 0.0005
3	75	0.0677 ± 0.0005
4	100	0.0675 ± 0.0005
5	120	0.0675 ± 0.0005
6	140	0.0670 ± 0.0005

A repeatability uncertainty of ±0.0003 N/m was obtained.

C.2.3 Viscosity

The viscosities of the air and water were taken as the tabulated values at standard pressure and temperature.

A Brookfield Cone/Plate LVT Digital Viscometer was used to measure viscosities of the polymer solution at different concentrations. The viscometer rotates a conical spindle at a precise speed and measures the torque necessary to overcome the viscous resistance to the induced movement caused by the presence of sample fluid between the spindle and a stationary flat plate. All the measurements were made at 20°C. A range of polymer concentrations of 30 – 140 ppm was studied.

Figures C.1 to C.6 show the measured viscosities as a function of shear rate for two samples taken from different batches of polymer solution at the same concentration. These measurements were made to assess consistency in solution viscosity when performing tests with the polymer solution.

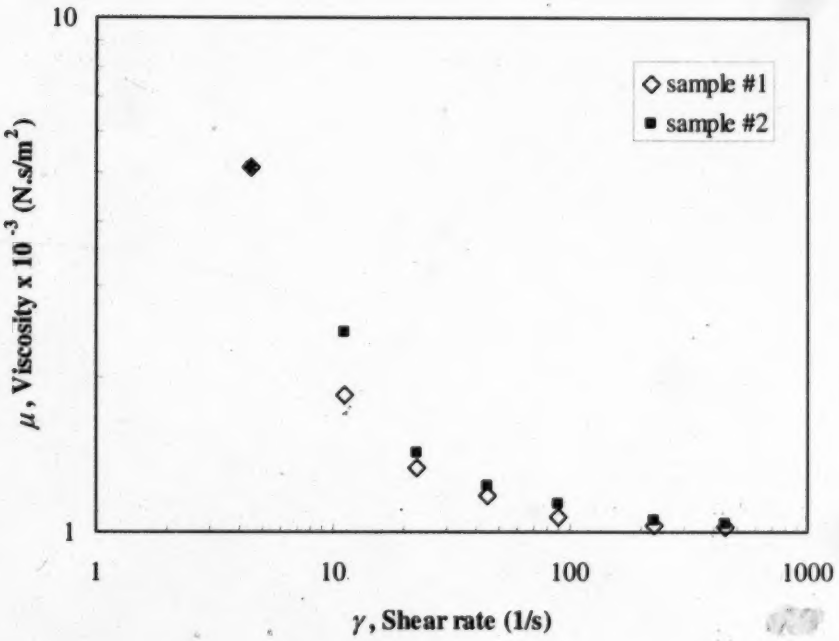

Figure C.1: Viscosity μ as a function of the shear rate γ for two samples taken from different batches of polymer solution at a concentration of 30 ppm.

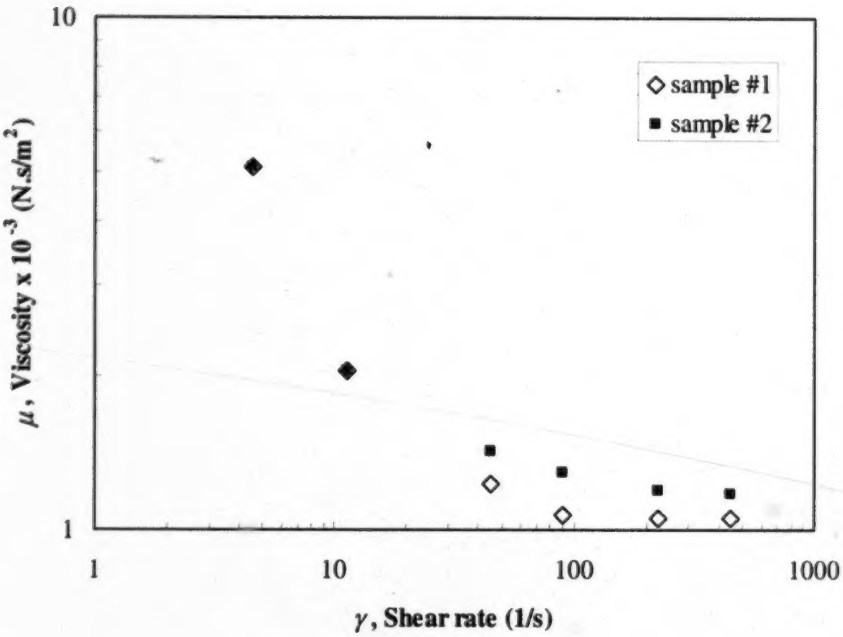

Figure C.2: Viscosity μ as a function of the shear rate γ for two samples taken from different batches of polymer solution at a concentration of 50 ppm.

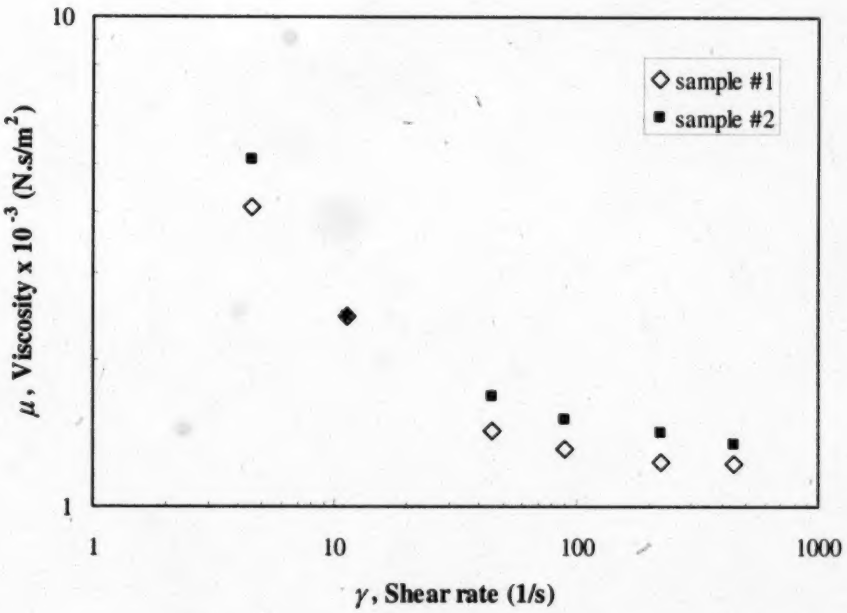

Figure C.3: Viscosity μ as a function of the shear rate γ for two samples taken from different batches of polymer solution at a concentration of 75 ppm.

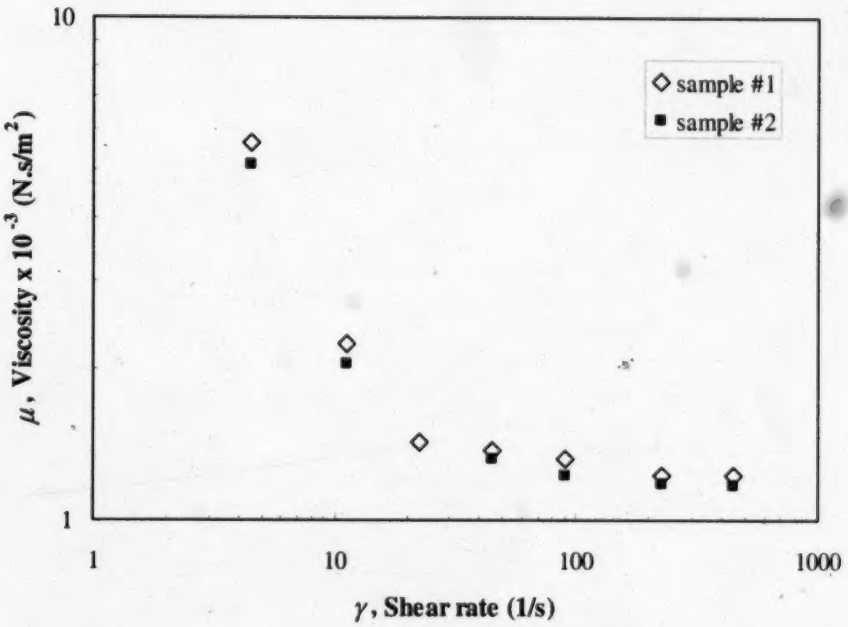

Figure C.4: Viscosity μ as a function of the shear rate γ for two samples taken from different batches of polymer solution at a concentration of 100 ppm.

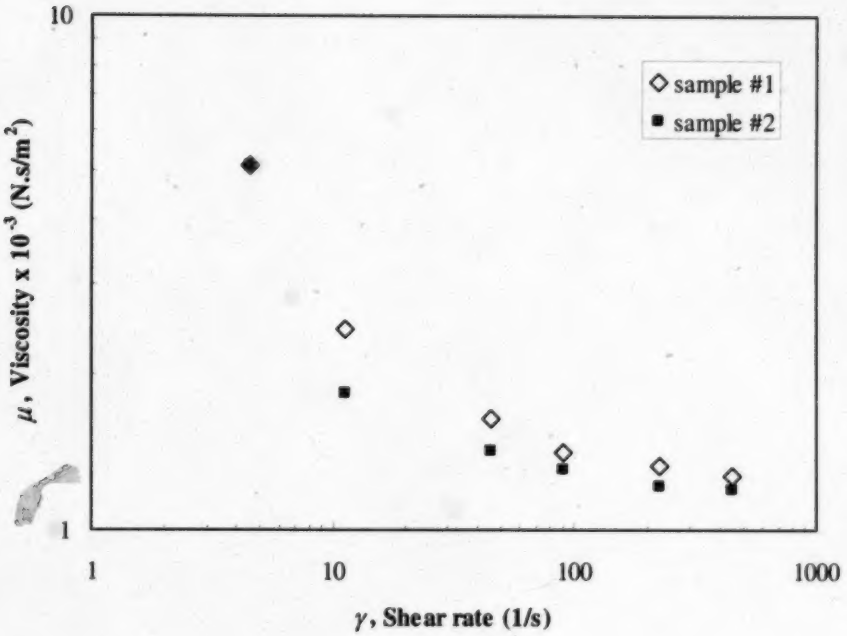

Figure C.5: Viscosity μ as a function of the shear rate γ for two samples taken from different batches of polymer solution at a concentration of 120 ppm.

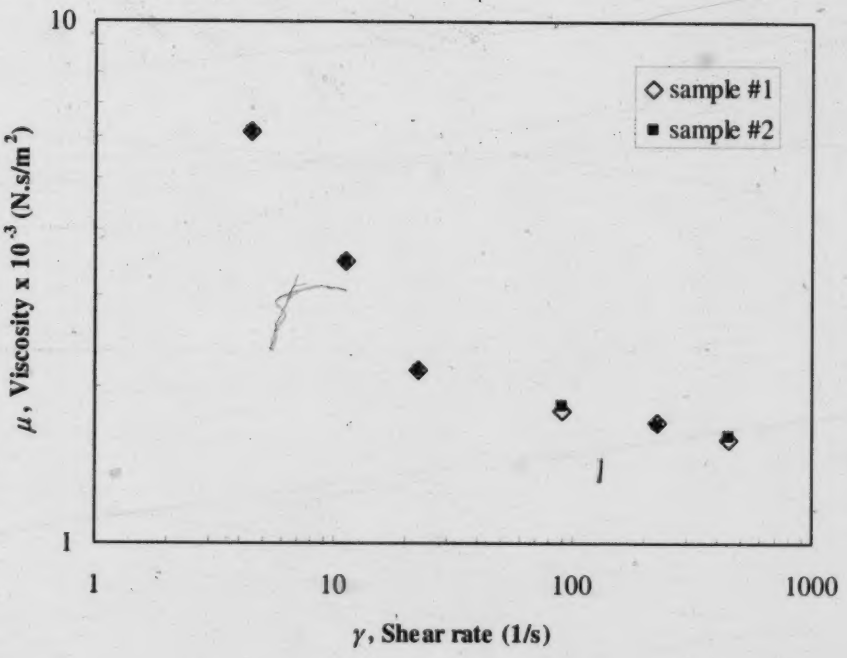

Figure C.6: Viscosity μ as a function of the shear rate γ for two samples taken from different batches of polymer solution at a concentration of 140 ppm.

D APPENDIX: Uncertainty Analysis

The uncertainties in the results were evaluated by perturbation; the results for the worst case scenarios are presented in the following tables.

Useful equations for a further analysis of propagation of uncertainty into the results were also developed and presented in Section D.1.

Table D.1: Uncertainty in the calculated parameters by perturbation of the liquid holdup for air and water at flow rates of 17.3 g/s and 148 g/s respectively.

			Uncertainty		
Measured Parameters:					
$\dot{m}_g$	g/s	16.9			
$\dot{m}_l$	g/s	149			
P_1	kPa	242			
P_2	kPa	232			
P_3	kPa	222			
P_4	kPa	212			
P_5	kPa	203			
P_6	kPa	----			
P_{up}	kPa	273.9			
P_{diff}	kPa	0.671			
dP/dx	Pa/m	4018			
α_l		0.127	± 5%	± 10%	± 20%
Calculated Parameters:					
ρ_g	kg/m^3	2.58	± 0%	± 0%	± 0%
U_{sg}	m/s	12.9	± 0%	± 0%	± 0%
U_{sl}	m/s	0.294	± 0%	± 0%	± 0%
E		0.152	± 31%	± 68%	± 118%
α_f		0.124	± 6%	± 12%	± 23%
d	mm	0.813	± 6%	± 13%	± 24%
U_f	m/s	2.01	± 0%	± 0%	± 1%
U_{sf}	m/s	0.250	± 6%	± 12%	± 23%
U_{sc}	m/s	13.0	± 0%	± 0%	± 0%
λ_c		0.997	± 0%	± 0%	± 0%
ρ_c	kg/m^3	6.00	± 18%	± 38%	± 74%
μ_c	N.s/m^2	2.1E-05	± 5%	± 11%	± 20%
α_c		0.876	± 1%	± 2%	± 3%
Hyd	Pa/m	1264	± 5%	± 10%	± 19%
Acc	Pa/m	136	± 10%	± 22%	± 43%
Fr	Pa/m	2618	± 2%	± 4%	± 7%
f		0.081	± 2%	± 5%	± 9%

Table D.2: Uncertainty in the calculated parameters by perturbation of the liquid holdup for air and polymer solution at flow rates of 17.3 g/s and 148 g/s respectively.

			Uncertainty		
Measured Parameters:					
$\dot{m}_g$	g/s	17.6			
$\dot{m}_l$	g/s	146			
P_1	kPa	182			
P_2	kPa	177			
P_3	kPa	170			
P_4	kPa	163			
P_5	kPa	158			
P_6	kPa	----			
P_{up}	kPa	204.1			
P_{diff}	kPa	0.975			
dP/dx	Pa/m	2568			
α_l		0.145	±5%	±10%	±20%
Calculated Parameters:					
ρ_g	kg/m^3	1.99	±0	±0	±0
U_{sg}	m/s	17.5	±0	±0	±0
U_{sl}	m/s	0.289	±0	±0	±0
E		0	±0	±0	±0
α_f		0.145	±5	±10	±20
d	mm	0.959	±5	±10	±21
U_f	m/s	1.99	±5	±10	±21
U_{sf}	m/s	0.289	±0	±0	±0
U_{sc}	m/s	17.5	±0	±0	±0
λ_c		1	±0	±0	±0
ρ_c	kg/m^3	1.99	±0	±0	±0
μ_c	N.s/m^2	1.8E-05	±0	±0	±0
α_c		0.855	±1	±2	±3
Hyd	Pa/m	1438	±5	±10	±20
Acc	Pa/m	105	±2	±4	±7
Fr	Pa/m	1024	±7	±13	±27
f_{DRA}		0.024	±6	±13	±25

Table D.3: Uncertainty in the calculated parameters by perturbation of the pressure gradient for air and water at flow rates of 17.3 g/s and 148 g/s respectively.

			Uncertainty		
Measured Parameters:					
$\dot{m}_g$	g/s	**16.9**			
$\dot{m}_l$	g/s	**149**			
P_1	kPa	**242**			
P_2	kPa	**232**			
P_3	kPa	**222**			
P_4	kPa	**212**			
P_5	kPa	**203**			
P_6	kPa	**----**			
P_{up}	kPa	**273.9**			
P_{diff}	kPa	**0.671**			
dP/dx	Pa/m	**4018**	± 5%	± 10%	± 20%
α_l		**0.127**			
Calculated Parameters:					
ρ_g	kg/m^3	**2.58**	± 0%	± 0%	± 0%
U_{sg}	m/s	**12.9**	± 0%	± 0%	± 0%
U_{sl}	m/s	**0.294**	± 0%	± 0%	± 0%
E		**0.152**	± 32%	± 64%	± 117%
α_f		**0.124**	± 1%	± 2%	± 3%
d	mm	**0.813**	± 1%	± 2%	± 3%
U_f	m/s	**2.01**	± 5%	± 10%	± 20%
U_{sf}	m/s	**0.250**	± 6%	± 11%	± 23%
U_{sc}	m/s	**13.0**	± 0%	± 0%	± 0%
λ_c		**0.997**	± 0%	± 0%	± 0%
ρ_c	kg/m^3	**6.00**	± 18%	± 36%	± 73%
μ_c	N.s/m^2	**2.1E-05**	± 5%	± 10%	± 20%
α_c		**0.876**	± 0%	± 0%	± 0%
Hyd	Pa/m	**1264**	± 0%	± 0%	± 0%
$A\varepsilon c$	Pa/m	**136**	± 9%	± 19%	± 38%
Fr	Pa/m	**2618**	± 8%	± 16%	± 33%
f		**0.081**	± 7%	± 15%	± 29%

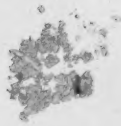

Table D.4: Uncertainty in the calculated parameters by perturbation of the pressure gradient for air and polymer solution at flow rates of 17.3 g/s and 148 g/s respectively.

			Uncertainty		
Measured Parameters:					
$\dot{m}_g$	g/s	17.6			
$\dot{m}_l$	g/s	146			
P_1	kPa	182			
P_2	kPa	177			
P_3	kPa	170			
P_4	kPa	163			
P_5	kPa	158			
P_6	kPa	----			
P_{up}	kPa	204.1			
P_{diff}	kPa	0.975			
dP/dx	Pa/m	2568	± 5%	± 10%	± 20%
α_l		0.145			
Calculated Parameters:					
ρ_g	kg/m^3	1.99	± 0%	± 0%	± 0%
U_{sg}	m/s	17.5	± 0%	± 0%	± 0%
U_{sl}	m/s	0.289	± 0%	± 0%	± 0%
E		0	± 0%	± 0%	± 0%
α_f		0.145	± 0%	± 0%	± 0%
d	mm	0.959	± 0%	± 0%	± 0%
U_f	m/s	1.99	± 0%	± 0%	± 0%
U_{sf}	m/s	0.289	± 0%	± 0%	± 0%
U_{sc}	m/s	17.5	± 0%	± 0%	± 0%
λ_c		1	± 0%	± 0%	± 0%
ρ_c	kg/m^3	1.99	± 0%	± 0%	± 0%
μ_c	N.s/m^2	1.8E-05	± 0%	± 0%	± 0%
α_c		0.855	± 0%	± 0%	± 0%
Hyd	Pa/m	1438	± 0%	± 0%	± 0%
Acc	Pa/m	105	± 0%	± 0%	± 0%
Fr	Pa/m	1024	± 13%	± 25%	± 50%
f_{DRA}		0.024	± 11%	± 23%	± 45%

Table D.5: Uncertainty in the calculated parameters by perturbation of the liquid holdup for air and water at flow rates of 42.9 g/s and 148 g/s respectively.

			Uncertainty		
Measured Parameters:					
$\dot{m}_g$	g/s	**43.0**			
$\dot{m}_l$	g/s	**148**			
P_1	kPa	**446**			
P_2	kPa	**435**			
P_3	kPa	**421**			
P_4	kPa	**408**			
P_5	kPa	**396**			
P_6	kPa	**----**			
P_{up}	kPa	**490.4**			
P_{diff}	kPa	**2.421**			
dP/dx	Pa/m	**5173**			
α_l		**0.087**	± 5%	± 10%	± 20%
Calculated Parameters:					
ρ_g	kg/m^3	**4.93**	± 0%	± 0%	± 0%
U_{sg}	m/s	**17.2**	± 0%	± 0%	± 0%
U_{sl}	m/s	**0.293**	± 0%	± 0%	± 0%
E		**0.330**	± 15%	± 27%	± 56%
α_f		**0.082**	± 6%	± 12%	± 25%
d	mm	**0.534**	± 7%	± 12%	± 25%
U_f	m/s	**2.39**	± 1%	± 1%	± 3%
U_{sf}	m/s	**0.196**	± 7%	± 14%	± 28%
U_{sc}	m/s	**17.3**	± 0%	± 0%	± 0%
λ_c		**0.994**	± 0%	± 0%	± 0%
ρ_c	kg/m^3	**10.48**	± 8%	± 14%	± 30%
μ_c	N.s/m^2	**2.3E-05**	± 3%	± 6%	± 13%
α_c		**0.918**	± 1%	± 1%	± 2%
Hyd	Pa/m	**899**	± 5%	± 9%	± 19%
Acc	Pa/m	**319**	± 5%	± 10%	± 21%
Fr	Pa/m	**3955**	± 1%	± 1%	± 3%
f		**0.037**	± 1%	± 2%	± 4%

Table D.6: Uncertainty in the calculated parameters by perturbation of the liquid holdup for air and polymer solution at flow rates of 42.9 g/s and 148 g/s respectively.

			Uncertainty		
Measured Parameters:					
$\dot{m}_g$	g/s	42.8			
$\dot{m}_l$	g/s	149			
P_1	kPa	413			
P_2	kPa	404			
P_3	kPa	394			
P_4	kPa	383			
P_5	kPa	374			
P_6	kPa				
P_{up}	kPa	443.4			
P_{diff}	kPa	2.642			
dP/dx	Pa/m	4053			
α_l		0.093	± 5%	± 10%	± 20%
Calculated Parameters:					
ρ_g	kg/m^3	4.62	± 0%	± 0%	± 0%
U_{sg}	m/s	18.3	± 0%	± 0%	± 0%
U_{sl}	m/s	0.296	± 0%	± 0%	± 0%
E		0	± 0%	± 0%	± 0%
α_f		0.093	± 5%	± 10%	± 20%
d	mm	0.608	± 5%	± 10%	± 20%
U_f	m/s	3.16	± 5%	± 10%	± 21%
U_{sf}	m/s	0.296	± 0%	± 0%	± 0%
U_{sc}	m/s	18.3	± 0%	± 0%	± 0%
λ_c		1	± 0%	± 0%	± 0%
ρ_c	kg/m^3	4.62	± 0%	± 0%	± 0%
μ_c	N.s/m^2	1.8E-05	± 0%	± 0%	± 0%
α_c		0.907	± 0%	± 1%	± 2%
Hyd	Pa/m	955	± 5%	± 10%	± 19%
Acc	Pa/m	216	± 1%	± 3%	± 6%
Fr	Pa/m	2882	± 1%	± 3%	± 6%
f_{DRA}		0.026	± 1%	± 3%	± 6%

Table D.7: Uncertainty in the calculated parameters by perturbation of the pressure gradient for air and water at flow rates of 42.9 g/s and 148 g/s respectively.

			Uncertainty		
Measured Parameters:					
m^*_g	g/s	43.0			
m^*_l	g/s	148			
P_1	kPa	446			
P_2	kPa	435			
P_3	kPa	421			
P_4	kPa	408			
P_5	kPa	396			
P_6	kPa	----			
P_{up}	kPa	490.4			
P_{diff}	kPa	2.421			
dP/dx	Pa/m	5173	± 5%	± 10%	± 20%
α_l		0.087			
Calculated Parameters:					
ρ_g	kg/m^3	4.93	± 0%	± 0%	± 0%
U_{sg}	m/s	17.2	± 0%	± 0%	± 0%
U_{sl}	m/s	0.293	± 0%	± 0%	± 0%
E		0.330	± 10%	± 19%	± 39%
α_f		0.082	± 1%	± 1%	± 2%
d	mm	0.534	± 1%	± 1%	± 2%
U_f	m/s	2.39	± 4%	± 8%	± 17%
U_{sf}	m/s	0.196	± 5%	± 9%	± 19%
U_{sc}	m/s	17.3	± 0%	± 0%	± 0%
λ_c		0.994	± 0%	± 0%	± 0%
ρ_c	kg/m^3	10.48	± 5%	± 10%	± 20%
μ_c	N.s/m^2	2.3E-05	± 2%	± 4%	± 9%
α_c		0.918	± 0%	± 0%	± 0%
Hyd	Pa/m	899	± 0%	± 0%	± 0%
Acc	Pa/m	319	± 3%	± 7%	± 14%
Fr	Pa/m	3955	± 7%	± 14%	± 27%
f		0.037	± 6%	± 12%	± 24%

Table D.8: Uncertainty in the calculated parameters by perturbation of the pressure gradient for air and polymer solution at flow rates of 42.9 g/s and 148 g/s respectively.

			Uncertainty		
Measured Parameters:					
m^*_g	g/s	42.8			
m^*_l	g/s	149			
P_1	kPa	413			
P_2	kPa	404			
P_3	kPa	394			
P_4	kPa	383			
P_5	kPa	374			
P_6	kPa				
P_{up}	kPa	443.4			
P_{diff}	kPa	2.642			
dP/dx	Pa/m	4053	± 5%	± 10%	± 20%
α_l		0.093			
Calculated Parameters:					
ρ_g	kg/m^3	4.62	± 0%	± 0%	± 0%
U_{sg}	m/s	18.3	± 0%	± 0%	± 0%
U_{sl}	m/s	0.296	± 0%	± 0%	± 0%
E		0	± 0%	± 0%	± 0%
α_f		0.093	± 0%	± 0%	± 0%
d	mm	0.608	± 0%	± 0%	± 0%
U_f	m/s	3.16	± 0%	± 0%	± 0%
U_{sf}	m/s	0.296	± 0%	± 0%	± 0%
U_{sc}	m/s	18.3	± 0%	± 0%	± 0%
λ_c		1	± 0%	± 0%	± 0%
ρ_c	kg/m^3	4.62	± 0%	± 0%	± 0%
μ_c	N.s/m^2	1.8E-05	± 0%	± 0%	± 0%
α_c		0.907	± 0%	± 0%	± 0%
Hyd	Pa/m	955	± 0%	± 0%	± 0%
Acc	Pa/m	216	± 0%	± 0%	± 0%
Fr	Pa/m	2882	± 7%	± 14%	± 28%
f_{DRA}		0.026	± 7%	± 13%	± 26%

D.1 Equations

Superficial Gas Velocity U_{sg}

$$U_{sg} = \frac{4\dot{m}_g}{\pi \rho_g D^2} \tag{D.1}$$

$$dU_{sg} = \left(\frac{\partial U_{sg}}{\partial \dot{m}_g}\right) d\dot{m}_g + \left(\frac{\partial U_{sg}}{\partial \rho_g}\right) d\rho_g \tag{D.2}$$

$$\left(\frac{dU_{sg}}{U_{sg}}\right)^2 = \frac{1}{U_{sg}^{\ 2}}\left(\frac{\partial U_{sg}}{\partial \dot{m}_g}\right)^2 d\dot{m}_g^{\ 2} + \frac{1}{U_{sg}^{\ 2}}\left(\frac{\partial U_{sg}}{\partial \rho_g}\right)^2 d\rho_g^{\ 2} \tag{D.3}$$

$$\left(\frac{dU_{sg}}{U_{sg}}\right) = \sqrt{\frac{1}{U_{sg}^{\ 2}}\left(\frac{\partial U_{sg}}{\partial \dot{m}_g}\right)^2 d\dot{m}_g^{\ 2} + \frac{1}{U_{sg}^{\ 2}}\left(\frac{\partial U_{sg}}{\partial \rho_g}\right)^2 d\rho_g^{\ 2}} \tag{D.4}$$

$$\left(\frac{dU_{sg}}{U_{sg}}\right) = \sqrt{\frac{\pi^2 \rho_g^{\ 2} D^4}{16\dot{m}_g^{\ 2}}\left(\frac{4}{\pi \rho_g D^2}\right)^2 d\dot{m}_g^{\ 2} + \frac{\pi^2 \rho_g^{\ 2} D^4}{16\dot{m}_g^{\ 2}}\left(\frac{-4\dot{m}_g}{\pi D^2 \rho_g^{\ 2}}\right)^2 d\rho_g^{\ 2}} \tag{D.5}$$

Simplifying terms:

$$\left(\frac{dU_{sg}}{U_{sg}}\right) = \sqrt{\frac{d\dot{m}_g^{\ 2}}{\dot{m}_g^{\ 2}} + \frac{d\rho_g^{\ 2}}{\rho_g^{\ 2}}} \tag{D.6}$$

Superficial Liquid Velocity U_{sl}

$$U_{sl} = \frac{4\dot{m}_l}{\pi D^2 \rho_l} \tag{D.7}$$

$$dU_{sl} = \left(\frac{\partial U_{sl}}{\partial \dot{m}_l} \right) d\dot{m}_l \tag{D.8}$$

$$\frac{dU_{sl}}{U_{sl}} = \frac{1}{U_{sl}} \left(\frac{\partial U_{sl}}{\partial \dot{m}_l} \right) d\dot{m}_l \tag{D.9}$$

$$\frac{dU_{sl}}{U_{sl}} = \frac{\pi D^2 \rho_l}{4\dot{m}_l} \left(\frac{4}{\pi D^2 \rho_l} \right) d\dot{m}_l \tag{D.10}$$

Simplifying terms:

$$\frac{dU_{sl}}{U_{sl}} = \frac{d\dot{m}_l}{\dot{m}_l} \tag{D.11}$$

Liquid Volume Fraction λ_l:

$$\lambda_l = \frac{U_{sl}}{U_{sl} + U_{sg}} \tag{D.12}$$

$$d\lambda_l = \left(\frac{\partial \lambda_l}{\partial U_{sl}} \right) dU_{sl} + \left(\frac{\partial \lambda_l}{\partial U_{sg}} \right) dU_{sg} \tag{D.13}$$

$$\left(\frac{d\lambda_l}{\lambda_l} \right)^2 = \frac{1}{\lambda_l^2} \left(\frac{\partial \lambda_l}{\partial U_{sl}} \right)^2 dU_{sl}^2 + \frac{1}{\lambda_l^2} \left(\frac{\partial \lambda_l}{\partial U_{sg}} \right)^2 dU_{sg}^2 \tag{D.14}$$

$$\left(\frac{d\lambda_l}{\lambda_l} \right) = \sqrt{\frac{1}{\lambda_l^2} \left(\frac{\partial \lambda_l}{\partial U_{sl}} \right)^2 dU_{sl}^2 + \frac{1}{\lambda_l^2} \left(\frac{\partial \lambda_l}{\partial U_{sg}} \right)^2 dU_{sg}^2} \tag{D.15}$$

$$\left(\frac{d\lambda_l}{\lambda_l} \right) = \sqrt{\frac{(U_{sl} + U_{sg})^2}{U_{sl}^2} \left(\frac{U_{sg}}{(U_{sl} + U_{sg})^2} \right)^2 dU_{sl}^2} \tag{D.16}$$

$$+\sqrt{\frac{(U_{sl}+U_{sg})^2}{U_{sl}^{\ 2}}\left(\frac{U_{sl}}{(U_{sl}+U_{sg})^2}\right)^2 dU_{sg}^{\ 2}}$$

Simplifying terms:

$$\left(\frac{d\lambda_l}{\lambda_l}\right)=\frac{1}{(U_{sl}+U_{sg})}\sqrt{\frac{U_{sg}^{\ 2}}{U_{sl}^{\ 2}}dU_{sl}^{\ 2}+dU_{sg}^{\ 2}} \qquad \text{(D.17)}$$

Gas Volume Fraction λ_g:

$$\lambda_g=\frac{U_{sg}}{U_{sl}+U_{sg}} \qquad \text{(D.18)}$$

$$d\lambda_g=\left(\frac{\partial\lambda_g}{\partial U_{sl}}\right)dU_{sl}+\left(\frac{\partial\lambda_g}{\partial U_{sg}}\right)dU_{sg} \qquad \text{(D.19)}$$

$$\left(\frac{d\lambda_g}{\lambda_g}\right)^2=\frac{1}{\lambda_g^{\ 2}}\left(\frac{\partial\lambda_g}{\partial U_{sl}}\right)^2 dU_{sl}^{\ 2}+\frac{1}{\lambda_g^{\ 2}}\left(\frac{\partial\lambda_g}{\partial U_{sg}}\right)^2 dU_{sg}^{\ 2} \qquad \text{(D.20)}$$

$$\left(\frac{d\lambda_g}{\lambda_g}\right)=\sqrt{\frac{1}{\lambda_g^{\ 2}}\left(\frac{\partial\lambda_g}{\partial U_{sl}}\right)^2 dU_{sl}^{\ 2}+\frac{1}{\lambda_g^{\ 2}}\left(\frac{\partial\lambda_g}{\partial U_{sg}}\right)^2 dU_{sg}^{\ 2}} \qquad \text{(D.21)}$$

$$\left(\frac{d\lambda_g}{\lambda_g}\right)=\sqrt{\frac{(U_{sl}+U_{sg})^2}{U_{sg}^{\ 2}}\left(\frac{U_{sg}}{(U_{sl}+U_{sg})^2}\right)^2 dU_{sl}^{\ 2}} \qquad \text{(D.22)}$$

$$+\sqrt{\frac{(U_{sl}+U_{sg})^2}{U_{sg}^{\ 2}}\left(\frac{U_{sl}}{(U_{sl}+U_{sg})^2}\right)^2 dU_{sg}^{\ 2}}$$

Simplifying terms:

$$\left(\frac{d\lambda_g}{\lambda_g}\right)=\frac{1}{(U_{sl}+U_{sg})}\sqrt{dU_{sl}^{\,2}+\frac{U_{sl}^{\,2}}{U_{sg}^{\,2}}dU_{sg}^{\,2}} \tag{D.23}$$

Gas Holdup α_g:

$$\alpha_g=1-\alpha_l \tag{D.24}$$

$$d\alpha_g=\left(\frac{\partial\alpha_g}{\partial\alpha_l}\right)d\alpha_l \tag{D.25}$$

$$\left(\frac{d\alpha_g}{\alpha_g}\right)^2=\frac{1}{\alpha_g^{\,2}}\left(\frac{\partial\alpha_g}{\partial\alpha_l}\right)^2 d\alpha_l^{\,2} \tag{D.26}$$

$$\left(\frac{d\alpha_g}{\alpha_g}\right)=\sqrt{\frac{1}{\alpha_g^{\,2}}\left(\frac{\partial\alpha_g}{\partial\alpha_l}\right)^2 d\alpha_l^{\,2}} \tag{D.27}$$

$$\left(\frac{d\alpha_g}{\alpha_g}\right)=\frac{1}{(1-\alpha_l)}d\alpha_l \tag{D.28}$$

Film Holdup α_f:

$$\alpha_f=\alpha_l+E\frac{U_{sl}}{U_{sg}}(\alpha_l-1) \tag{D.29}$$

$$d\alpha_f=\left(\frac{\partial\alpha_f}{\partial\alpha_l}\right)d\alpha_l+\left(\frac{\partial\alpha_f}{\partial U_{sl}}\right)dU_{sl}+\left(\frac{\partial\alpha_f}{\partial U_{sg}}\right)dU_{sg}+\left(\frac{\partial\alpha_f}{\partial E}\right)dE \tag{D.30}$$

$$\left(\frac{d\alpha_f}{\alpha_f}\right)^2=\frac{1}{\alpha_f^{\,2}}\left(\frac{\partial\alpha_f}{\partial\alpha_l}\right)^2 d\alpha_l^{\,2}+\frac{1}{\alpha_f^{\,2}}\left(\frac{\partial\alpha_f}{\partial U_{sl}}\right)^2 dU_{sl}^{\,2}+\frac{1}{\alpha_f^{\,2}}\left(\frac{\partial\alpha_f}{\partial U_{sg}}\right)^2 dU_{sg}^{\,2}$$

$$+\frac{1}{\alpha_f^{\,2}}\left(\frac{\partial \alpha_f}{\partial E}\right)^2 dE^2 \qquad \text{(D.31)}$$

$$\left(\frac{d\alpha_f}{\alpha_f}\right)=\sqrt{\frac{1}{\alpha_f^{\,2}}\left(\frac{\partial \alpha_f}{\partial \alpha_l}\right)^2 d\alpha_l^{\,2}+\frac{1}{\alpha_f^{\,2}}\left(\frac{\partial \alpha_f}{\partial U_{sl}}\right)^2 dU_{sl}^{\,2}+\frac{1}{\alpha_f^{\,2}}\left(\frac{\partial \alpha_f}{\partial U_{sg}}\right)^2 dU_{sg}^{\,2}}$$

$$+\sqrt{\frac{1}{\alpha_f^{\,2}}\left(\frac{\partial \alpha_f}{\partial E}\right)^2 dE^2} \qquad \text{(D.32)}$$

$$\frac{1}{\alpha_f^{\,2}}\left(\frac{\partial \alpha_f}{\partial \alpha_l}\right)^2=\frac{U_{sg}^{\,2}}{\left(\alpha_l U_{sg}+E\alpha_l U_{sl}-EU_{sl}\right)^2}\frac{\left(U_{sg}+EU_{sl}\right)^2}{U_{sg}^{\,2}}$$

$$=\frac{\left(U_{sg}+EU_{sl}\right)^2}{\left[\alpha_l\left(U_{sg}+EU_{sl}\right)-EU_{sl}\right]^2} \qquad \text{(D.33)}$$

$$\frac{1}{\alpha_f^{\,2}}\left(\frac{\partial \alpha_f}{\partial U_{sl}}\right)^2=\frac{U_{sg}^{\,2}}{\left[\alpha_l U_{sg}+EU_{sl}(\alpha_l-1)\right]^2}\frac{E^2(\alpha_l-1)^2}{U_{sg}^{\,2}}$$

$$=\frac{E^2(\alpha_l-1)^2}{\left[\alpha_l U_{sg}+EU_{sl}(\alpha_l-1)\right]^2} \qquad \text{(D.34)}$$

$$\frac{1}{\alpha_f^{\,2}}\left(\frac{\partial \alpha_f}{\partial U_{sg}}\right)^2=\frac{U_{sg}^{\,2}}{\left[\alpha_l U_{sg}+EU_{sl}(\alpha_l-1)\right]^2}\frac{E^2\,U_{sl}^{\,2}(1-\alpha_l)^2}{U_{sg}^{\,4}}$$

$$=\frac{E^2U_{sl}^{\,2}(1-\alpha_l)^2}{U_{sg}^{\,2}\left[\alpha_l U_{sg}+EU_{sl}(\alpha_l-1)\right]^2} \qquad \text{(D.35)}$$

$$\frac{1}{\alpha_f^{\,2}}\left(\frac{\partial \alpha_f}{\partial E}\right)^2=\frac{U_{sg}^{\,2}}{\left[\alpha_l U_{sg}+EU_{sl}(\alpha_l-1)\right]^2}\frac{U_{sl}^{\,2}(\alpha_l-1)^2}{U_{sg}^{\,2}}$$

$$= \frac{U_{sl}^{\,2}(\alpha_l - 1)^2}{\left[\alpha_l U_{sg} + EU_{sl}(\alpha_l - 1)\right]^2} \tag{D.36}$$

Substituting Equations D.33, D.34, D.35 and D.36 into Equation D.32:

$$\frac{d\alpha_f}{\alpha_f} = \frac{1}{\left[\alpha_l\left(U_{sg} + EU_{sl}\right) - EU_{sl}\right]}\sqrt{\left(U_{sg} + EU_{sl}\right)^2 d\alpha_l^{\,2} + E^2(\alpha_l - 1)^2 dU_{sl}^{\,2}} \tag{D.37}$$

$$+ \frac{1}{\left[\alpha_l\left(U_{sg} + EU_{sl}\right) - EU_{sl}\right]}\sqrt{\frac{E^2 U_{sl}^{\,2}(1-\alpha_l)^2}{U_{sg}^{\,2}} dU_{sg}^{\,2} + U_{sl}^{\,2}(\alpha_l - 1)^2 dE^2}$$

Film Thickness d:

$$d = \frac{D\left(1 - \sqrt{1-\alpha_f}\right)}{2} \tag{D.38}$$

$$d(d) = \left(\frac{\partial d}{\partial \alpha_f}\right) d\alpha_f \tag{D.39}$$

$$\frac{d(d)}{d} = \frac{1}{d}\left(\frac{\partial d}{\partial \alpha_f}\right) d\alpha_f \tag{D.40}$$

$$\frac{d(d)}{d} = \frac{2}{D\left(1 - \sqrt{1-\alpha_f}\right)}\left(\frac{1}{2} D \frac{1}{2\sqrt{1-\alpha_f}}\right) d\alpha_f \tag{D.41}$$

$$\frac{d(d)}{d} = \frac{d\alpha_f}{2\sqrt{1-\alpha_f}\left(1 - \sqrt{1-\alpha_f}\right)} \tag{D.42}$$

Core Holdup α_c:

$$\alpha_c = \frac{(D-2d)^2}{D^2} \tag{D.43}$$

$$d\alpha_c = \left(\frac{\partial \alpha_c}{\partial d}\right) d(d) \tag{D.44}$$

$$\left(\frac{d\alpha_c}{\alpha_c}\right)^2 = \frac{1}{\alpha_c^{\,2}}\left(\frac{\partial \alpha_c}{\partial d}\right)^2 d(d)^2 \tag{D.45}$$

$$\left(\frac{d\alpha_c}{\alpha_c}\right) = \sqrt{\frac{1}{\alpha_c^{\,2}}\left(\frac{\partial \alpha_c}{\partial d}\right)^2 d(d)^2} \tag{D.46}$$

$$\left(\frac{d\alpha_c}{\alpha_c}\right) = \sqrt{\frac{D^4}{(D-2d)^4}\frac{16(D-2d)^2}{D^4} d(d)^2} \tag{D.47}$$

Simplifying terms:

$$\left(\frac{d\alpha_c}{\alpha_c}\right) = \frac{4d(d)}{(D-2d)} \tag{D.48}$$

Gas Void Fraction in the Core λ_c:

$$\lambda_c = \frac{U_{sg}}{U_{sg} + EU_{sl}} \tag{D.49}$$

$$d\lambda_c = \left(\frac{\partial \lambda_c}{\partial U_{sg}}\right) dU_{sg} + \left(\frac{\partial \lambda_c}{\partial U_{sl}}\right) dU_{sl} + \left(\frac{\partial \lambda_c}{\partial E}\right) dE \tag{D.50}$$

$$\left(\frac{d\lambda_c}{\lambda_c}\right)^2 = \frac{1}{\lambda_c^{\,2}}\left(\frac{\partial \lambda_c}{\partial U_{sg}}\right)^2 dU_{sg}^{\,2} + \frac{1}{\lambda_c^{\,2}}\left(\frac{\partial \lambda_c}{\partial U_{sl}}\right)^2 dU_{sl}^{\,2} + \frac{1}{\lambda_c^{\,2}}\left(\frac{\partial \lambda_c}{\partial E}\right)^2 dE^2 \tag{D.51}$$

$$\frac{d\lambda_c}{\lambda_c} = \sqrt{\frac{1}{\lambda_c^{\,2}}\left(\frac{\partial \lambda_c}{\partial U_{sg}}\right)^2 dU_{sg}^{\,2} + \frac{1}{\lambda_c^{\,2}}\left(\frac{\partial \lambda_c}{\partial U_{sl}}\right)^2 dU_{sl}^{\,2} + \frac{1}{\lambda_c^{\,2}}\left(\frac{\partial \lambda_c}{\partial E}\right)^2 dE^2} \qquad \text{(D.52)}$$

$$\frac{1}{\lambda_c^{\,2}}\left(\frac{\partial \lambda_c}{\partial U_{sg}}\right)^2 = \frac{(U_{sg}+EU_{sl})^2}{U_{sg}^{\,2}}\left[\frac{U_{sg}+EU_{sl}-U_{sg}}{(U_{sg}+EU_{sl})^2}\right]^2$$

$$= \frac{(U_{sg}+EU_{sl})^2}{U_{sg}^{\,2}}\frac{E^2U_{sl}^{\,2}}{(U_{sg}+EU_{sl})^4}$$

$$= \frac{E^2U_{sl}^{\,2}}{U_{sg}^{\,2}(U_{sg}+EU_{sl})^2} \qquad \text{(D.53)}$$

$$\frac{1}{\lambda_c^{\,2}}\left(\frac{\partial \lambda_c}{\partial U_{sl}}\right)^2 = \frac{(U_{sg}+EU_{sl})^2}{U_{sg}^{\,2}}\left[\frac{-EU_{sg}}{(U_{sg}+EU_{sl})^2}\right]^2$$

$$= \frac{(U_{sg}+EU_{sl})^2}{U_{sg}^{\,2}}\frac{E^2U_{sg}^{\,2}}{(U_{sg}+EU_{sl})^4}$$

$$= \frac{E^2}{(U_{sg}+EU_{sl})^2} \qquad \text{(D.54)}$$

$$\frac{1}{\lambda_c^{\,2}}\left(\frac{\partial \lambda_c}{\partial E}\right)^2 = \frac{(U_{sg}+EU_{sl})^2}{U_{sg}^{\,2}}\left[\frac{-U_{sg}U_{sl}}{(U_{sg}+EU_{sl})^2}\right]^2$$

$$= \frac{(U_{sg}+EU_{sl})^2}{U_{sg}^{\,2}}\frac{U_{sg}^{\,2}U_{sl}^{\,2}}{(U_{sg}+EU_{sl})^4}$$

$$= \frac{U_{sl}^{\,2}}{(U_{sg}+EU_{sl})^2} \qquad \text{(D.55)}$$

Substituting Equations D.53, D.54 and D.55 into Equation D.52 and simplifying terms:

$$\frac{d\lambda_c}{\lambda_c} = \frac{1}{\left(U_{sg} + EU_{sl}\right)}\sqrt{\frac{E^2 U_{sl}^{\ 2}}{U_{sg}^{\ 2}} dU_{sg}^{\ 2} + E^2 dU_{sl}^{\ 2} + U_{sl_c}^{\ 2} dE^2} \tag{D.56}$$

Core Density ρ_c:

$$\rho_c = \rho_g \lambda_c + \rho_l (1 - \lambda_c) \tag{D.57}$$

$$d\rho_c = \left(\frac{\partial \rho_c}{\partial \rho_g}\right) d\rho_g + \left(\frac{\partial \rho_c}{\partial \lambda_c}\right) d\lambda_c \tag{D.58}$$

$$\left(\frac{d\rho_c}{\rho_c}\right)^2 = \frac{1}{\rho_c^{\ 2}}\left(\frac{\partial \rho_c}{\partial \rho_g}\right)^2 d\rho_g^{\ 2} + \frac{1}{\rho_c^{\ 2}}\left(\frac{\partial \rho_c}{\partial \lambda_c}\right)^2 d\lambda_c^{\ 2} \tag{D.59}$$

$$\frac{d\rho_c}{\rho_c} = \sqrt{\frac{1}{\rho_c^{\ 2}}\left(\frac{\partial \rho_c}{\partial \rho_g}\right)^2 d\rho_g^{\ 2} + \frac{1}{\rho_c^{\ 2}}\left(\frac{\partial \rho_c}{\partial \lambda_c}\right)^2 d\lambda_c^{\ 2}} \tag{D.60}$$

$$\frac{d\rho_c}{\rho_c} = \sqrt{\frac{\lambda_c^{\ 2} d\rho_g^{\ 2}}{\left[\rho_g \lambda_c + \rho_l (1 - \lambda_c)\right]^2} + \frac{(\rho_g - \rho_l)^2 d\lambda_c^{\ 2}}{\left[\rho_g \lambda_c + \rho_l (1 - \lambda_c)\right]^2}} \tag{D.61}$$

$$\frac{d\rho_c}{\rho_c} = \frac{1}{\rho_g \lambda_c + \rho_l (1 - \lambda_c)}\sqrt{\lambda_c^{\ 2} d\rho_g^{\ 2} + (\rho_g - \rho_l)^2 d\lambda_c^{\ 2}} \tag{D.62}$$

Core Viscosity μ_c:

$$\mu_c = \mu_g \lambda_c + \mu_l (1 - \lambda_c) \tag{D.63}$$

$$d\mu_c = \left(\frac{\partial \mu_c}{\partial \lambda_c}\right) d\lambda_c \tag{D.64}$$

$$\left(\frac{d\mu_c}{\mu_c}\right)^2 = \frac{1}{\mu_c{}^2}\left(\frac{\partial \mu_c}{\partial \lambda_c}\right)^2 d\lambda_c{}^2 \tag{D.65}$$

$$\frac{d\mu_c}{\mu_c} = \sqrt{\frac{(\mu_g - \mu_l)^2 d\lambda_c{}^2}{[\mu_g \lambda_c + \mu_l(1-\lambda_c)]^2}} \tag{D.66}$$

Core Superficial Velocity U_{sc}:

$$U_{sc} = U_{sg} + EU_{sl} \tag{D.67}$$

$$dU_{sc} = \left(\frac{\partial U_{sc}}{\partial U_{sg}}\right) dU_{sg} + \left(\frac{\partial U_{sc}}{\partial U_{sl}}\right) dU_{sl} + \left(\frac{\partial U_{sc}}{\partial E}\right) dE \tag{D.68}$$

$$\left(\frac{dU_{sc}}{U_{sc}}\right)^2 = \frac{1}{U_{sc}{}^2}\left(\frac{\partial U_{sc}}{\partial U_{sg}}\right)^2 dU_{sg}{}^2 + \frac{1}{U_{sc}{}^2}\left(\frac{\partial U_{sc}}{\partial U_{sl}}\right)^2 dU_{sl}{}^2 + \frac{1}{U_{sc}{}^2}\left(\frac{\partial U_{sc}}{\partial E}\right)^2 dE^2 \tag{D.69}$$

$$\frac{dU_{sc}}{U_{sc}} = \sqrt{\frac{1}{U_{sc}{}^2}\left(\frac{\partial U_{sc}}{\partial U_{sg}}\right)^2 dU_{sg}{}^2 + \frac{1}{U_{sc}{}^2}\left(\frac{\partial U_{sc}}{\partial U_{sl}}\right)^2 dU_{sl}{}^2 + \frac{1}{U_{sc}{}^2}\left(\frac{\partial U_{sc}}{\partial E}\right)^2 dE^2} \tag{D.70}$$

$$\frac{dU_{sc}}{U_{sc}} = \sqrt{\frac{dU_{sg}{}^2}{(U_{sg} + EU_{sl})^2} + \frac{E^2 dU_{sl}{}^2}{(U_{sg} + EU_{sl})^2} + \frac{U_{sl}{}^2 dE^2}{(U_{sg} + EU_{sl})^2}} \tag{D.71}$$

$$\frac{dU_{sc}}{U_{sc}} = \frac{1}{(U_{sg} + EU_{sl})}\sqrt{dU_{sg}{}^2 + E^2 dU_{sl}{}^2 + U_{sl}{}^2 dE^2} \tag{D.72}$$

Film Superficial Velocity U_{sf}:

$$U_{sf} = (1-E)U_{sl} \tag{D.73}$$

$$dU_{sf} = \left(\frac{\partial U_{sf}}{\partial U_{sl}}\right) dU_{sl} + \left(\frac{\partial U_{sf}}{\partial E}\right) dE \tag{D.74}$$

$$\left(\frac{dU_{sf}}{U_{sf}}\right)^2 = \frac{1}{U_{sf}^{\,2}}\left(\frac{\partial U_{sf}}{\partial U_{sl}}\right)^2 dU_{sl}^{\,2} + \frac{1}{U_{sf}^{\,2}}\left(\frac{\partial U_{sf}}{\partial E}\right)^2 dE^2 \tag{D.75}$$

$$\frac{dU_{sf}}{U_{sf}} = \sqrt{\frac{1}{U_{sf}^{\,2}}\left(\frac{\partial U_{sf}}{\partial U_{sl}}\right)^2 dU_{sl}^{\,2} + \frac{1}{U_{sf}^{\,2}}\left(\frac{\partial U_{sf}}{\partial E}\right)^2 dE^2} \tag{D.76}$$

$$\frac{dU_{sf}}{U_{sf}} = \sqrt{\frac{1}{U_{sl}^{\,2}(1-E)^2}(1-E)^2\, dU_{sl}^{\,2} + \frac{1}{U_{sl}^{\,2}(1-E)^2} U_{sl}^{\,2}\, dE^2} \tag{D.77}$$

Simplifying terms:

$$\frac{dU_{sf}}{U_{sf}} = \sqrt{\frac{dU_{sl}^{\,2}}{U_{sl}^{\,2}} + \frac{dE^2}{(1-E)^2}} \tag{D.78}$$

Average Film Velocity U_f:

$$U_f = \frac{U_{sf}}{\alpha_f} \tag{D.79}$$

$$dU_f = \left(\frac{\partial U_f}{\partial \alpha_f}\right) d\alpha_f + \left(\frac{\partial U_f}{\partial U_{sf}}\right) dU_{sf} \tag{D.80}$$

$$\left(\frac{dU_f}{U_f}\right)^2 = \frac{1}{U_f^{\,2}}\left(\frac{\partial U_f}{\partial \alpha_f}\right)^2 d\alpha_f^{\,2} + \frac{1}{U_f^{\,2}}\left(\frac{\partial U_f}{\partial U_{sf}}\right)^2 dU_{sf}^{\,2} \tag{D.81}$$

$$\frac{dU_f}{U_f} = \sqrt{\frac{1}{U_f^2}\left(\frac{\partial U_f}{\partial \alpha_f}\right)^2 d\alpha_f^2 + \frac{1}{U_f^2}\left(\frac{\partial U_f}{\partial U_{sf}}\right)^2 dU_{sf}^2} \tag{D.82}$$

$$\frac{dU_f}{U_f} = \sqrt{\frac{\alpha_f^2}{U_{sf}^2}\left(\frac{-U_{sf}}{\alpha_f^2}\right)^2 d\alpha_f^2 + \frac{\alpha_f^2}{U_{sf}^2}\left(\frac{1}{\alpha_f}\right)^2 dU_{sf}^2} \tag{D.83}$$

Simplifying terms:

$$\frac{dU_f}{U_f} = \sqrt{\frac{d\alpha_f^2}{\alpha_f^2} + \frac{dU_{sf}^2}{U_{sf}^2}} \tag{D.84}$$

Reynolds Number for the Liquid Film Re_f:

$$\mathrm{Re}_f = \frac{\rho_l U_f \alpha_f D}{\mu_l} \tag{D.85}$$

$$d\,\mathrm{Re}_f = \left(\frac{\partial \mathrm{Re}_f}{\partial \alpha_f}\right) d\alpha_f + \left(\frac{\partial \mathrm{Re}_f}{\partial U_f}\right) dU_f \tag{D.86}$$

$$\left(\frac{d\,\mathrm{Re}_f}{\mathrm{Re}_f}\right)^2 = \frac{1}{\mathrm{Re}_f^2}\left(\frac{\partial \mathrm{Re}_f}{\partial \alpha_f}\right)^2 d\alpha_f^2 + \frac{1}{\mathrm{Re}_f^2}\left(\frac{\partial \mathrm{Re}_f}{\partial U_f}\right)^2 dU_f^2 \tag{D.87}$$

$$\frac{d\,\mathrm{Re}_f}{\mathrm{Re}_f} = \sqrt{\frac{1}{\mathrm{Re}_f^2}\left(\frac{\partial \mathrm{Re}_f}{\partial \alpha_f}\right)^2 d\alpha_f^2 + \frac{1}{\mathrm{Re}_f^2}\left(\frac{\partial \mathrm{Re}_f}{\partial U_f}\right)^2 dU_f^2} \tag{D.88}$$

$$\frac{d\,\mathrm{Re}_f}{\mathrm{Re}_f} = \sqrt{\frac{\mu_l^2 \rho_l^2 U_f^2 D^2 d\alpha_f^2}{\rho_l^2 U_f^2 \alpha_f^2 D^2 \mu_l^2} + \frac{\mu_l^2 \rho_l^2 \alpha_f^2 D^2 dU_f^2}{\rho_l^2 U_f^2 \alpha_f^2 D^2 \mu_l^2}} \tag{D.89}$$

Simplifying terms:

$$\frac{d\,\mathrm{Re}_f}{\mathrm{Re}_f} = \sqrt{\frac{d\alpha_f^{\,2}}{\alpha_f^{\,2}} + \frac{dU_f^{\,2}}{U_f^{\,2}}} \tag{D.90}$$

Friction Factor for the Liquid Film f_f:

$$f_f = 2\left[\left(8/\mathrm{Re}_f\right)^{12} + 1/(a+b)^{3/2}\right]^{1/12} \tag{D.91}$$

$$df_f = \left(\frac{\partial f_f}{\partial \mathrm{Re}_f}\right) d\,\mathrm{Re}_f + \left(\frac{\partial f_f}{\partial a}\right) da + \left(\frac{\partial f_f}{\partial b}\right) db \tag{D.92}$$

$$\left(\frac{df_f}{f_f}\right)^2 = \frac{1}{f_f^{\,2}}\left(\frac{\partial f_f}{\partial \mathrm{Re}_f}\right)^2 d\,\mathrm{Re}_f^{\,2} + \frac{1}{f_f^{\,2}}\left(\frac{\partial f_f}{\partial a}\right)^2 da^2 + \frac{1}{f_f^{\,2}}\left(\frac{\partial f_f}{\partial b}\right)^2 db^2 \tag{D.93}$$

$$\frac{df_f}{f_f} = \sqrt{\frac{1}{f_f^{\,2}}\left(\frac{\partial f_f}{\partial \mathrm{Re}_f}\right)^2 d\,\mathrm{Re}_f^{\,2} + \frac{1}{f_f^{\,2}}\left(\frac{\partial f_f}{\partial a}\right)^2 da^2 + \frac{1}{f_f^{\,2}}\left(\frac{\partial f_f}{\partial b}\right)^2 db^2} \tag{D.94}$$

$$\frac{1}{f_f^{\,2}}\left(\frac{\partial f_f}{\partial \mathrm{Re}_f}\right)^2 = \frac{8^{24}}{\mathrm{Re}_f^{\,26}\left[\left(8/\mathrm{Re}_f\right)^{12} + 1/(a+b)^{3/2}\right]^2} \tag{D.95}$$

$$\frac{1}{f_f^{\,2}}\left(\frac{\partial f_f}{\partial a}\right)^2 = \frac{1}{64\left[\left(8/\mathrm{Re}_f\right)^{12} + 1/(a+b)^{3/2}\right]^2 (a+b)^5} \tag{D.96}$$

$$\frac{1}{f_f^{\,2}}\left(\frac{\partial f_f}{\partial b}\right)^2 = \frac{1}{64\left[\left(8/\mathrm{Re}_f\right)^{12} + 1/(a+b)^{3/2}\right]^2 (a+b)^5} \tag{D.97}$$

Substituting Equations D.95, D.96 and D.97 into Equation D.94 and rearranging terms:

$$\frac{df_f}{f_f} = \frac{1}{\left[(8/\mathrm{Re}_f)^{12} + 1/(a+b)^{3/2}\right]} \sqrt{\frac{8^{24}\, d\mathrm{Re}_f^{\,2}}{\mathrm{Re}_f^{\,26}} + \frac{da^2}{64(a+b)^5} + \frac{db^2}{64(a+b)^5}} \qquad \text{(D.98)}$$

$$a = \left[2.547 \ln\left((7/\mathrm{Re}_f)^{0.9} + 0.27\varepsilon/D\right)\right]^{16} \qquad \text{(D.99)}$$

$$da = \left(\frac{\partial a}{\partial \mathrm{Re}_f}\right) d\mathrm{Re}_f \qquad \text{(D.100)}$$

$$\left(\frac{da}{a}\right)^2 = \frac{1}{a^2}\left(\frac{\partial a}{\partial \mathrm{Re}_f}\right)^2 d\mathrm{Re}_f^{\,2} \qquad \text{(D.101)}$$

$$\frac{da}{a} = \sqrt{\frac{1}{a^2}\left(\frac{\partial a}{\partial \mathrm{Re}_f}\right)^2 d\mathrm{Re}_f^{\,2}} \qquad \text{(D.102)}$$

$$\frac{da}{a} = \sqrt{\frac{(16)^2 (2.547)^2 (0.9)^2 7^{3.8}\, d\mathrm{Re}_f^{\,2}}{\left[2.547 \ln\left((7/\mathrm{Re}_f)^{0.9} + 0.27\varepsilon/D\right)\right]^2 \left[(7/\mathrm{Re}_f)^{0.9} + 0.27\varepsilon/D\right]^2 \mathrm{Re}^{3.8}}} \qquad \text{(D.103)}$$

$$\frac{da}{a} = \frac{36.7 d\mathrm{Re}_f^{\,2}}{\left[2.547 \ln\left((7/\mathrm{Re}_f)^{0.9} + 0.27\varepsilon/D\right)\right]\left[(7/\mathrm{Re}_f)^{0.9} + 0.27\varepsilon/D\right]} \left(\frac{7}{\mathrm{Re}_f}\right)^{1.9} \qquad \text{(D.104)}$$

$$b = (37530/\mathrm{Re}_f)^{16} \qquad \text{(D.105)}$$

$$db = \left(\frac{\partial b}{\partial \mathrm{Re}_f}\right) d\mathrm{Re}_f \qquad \text{(D.106)}$$

$$\frac{db}{b} = \sqrt{\frac{1}{b^2}\left(\frac{\partial b}{\partial \mathrm{Re}_f}\right)^2 d\mathrm{Re}_f{}^2} \tag{D.107}$$

$$\frac{db}{b} = \sqrt{\left(\frac{\mathrm{Re}_f}{37530}\right)^{32}\left[16\left(\frac{37530}{\mathrm{Re}_f}\right)^{15}\left(-\frac{37530}{\mathrm{Re}_f{}^2}\right)\right]^2 d\mathrm{Re}_f{}^2} \tag{D.108}$$

Simplifying terms:

$$\frac{db}{b} = \frac{16}{\mathrm{Re}_f} d\mathrm{Re}_f \tag{D.109}$$

Hydrostatic Component *Hyd*:

$$Hyd = \left(\alpha_f \rho_l + \alpha_c \rho_c\right) g \tag{D.110}$$

$$dHyd = \left(\frac{\partial Hyd}{\partial \alpha_f}\right) d\alpha_f + \left(\frac{\partial Hyd}{\partial \alpha_c}\right) d\alpha_c + \left(\frac{\partial Hyd}{\partial \rho_c}\right) d\rho_c \tag{D.111}$$

$$\frac{dHyd}{Hyd} = \sqrt{\frac{1}{Hyd^2}\left(\frac{\partial Hyd}{\partial \alpha_f}\right)^2 d\alpha_f{}^2 + \frac{1}{Hyd^2}\left(\frac{\partial Hyd}{\partial \alpha_c}\right)^2 d\alpha_c{}^2 + \frac{1}{Hyd^2}\left(\frac{\partial Hyd}{\partial \rho_c}\right)^2 d\rho_c{}^2} \tag{D.112}$$

$$\frac{dHyd}{Hyd} = \sqrt{\frac{\rho_l{}^2 g^2 d\alpha_f{}^2}{\left(\alpha_f \rho_l + \alpha_c \rho_c\right)^2 g^2} + \frac{\rho_c{}^2 g^2 d\alpha_c{}^2}{\left(\alpha_f \rho_l + \alpha_c \rho_c\right)^2 g^2} + \frac{\alpha_c{}^2 g^2 d\rho_c{}^2}{\left(\alpha_f \rho_l + \alpha_c \rho_c\right)^2 g^2}} \tag{D.113}$$

Simplifying terms:

$$\frac{dHyd}{Hyd} = \frac{1}{\left(\alpha_f \rho_l + \alpha_c \rho_c\right)} \sqrt{\rho_l{}^2 d\alpha_f{}^2 + \rho_c{}^2 d\alpha_c{}^2 + \alpha_c{}^2 d\rho_c{}^2} \tag{D.114}$$

Frictional Component *Fr*:

$$Fr = \left(\frac{dP}{dx}\right)_{measured} - Hyd \tag{D.115}$$

$$dFr = \left(\frac{\partial Fr}{\partial(dP/dx)}\right) d(dP/dx) + \left(\frac{\partial Fr}{\partial Hyd}\right) dHyd \tag{D.116}$$

$$\frac{dFr}{Fr} = \sqrt{\frac{1}{Fr^2}\left(\frac{\partial Fr}{\partial(dP/dx)}\right)^2 d(dP/dx)^2 + \frac{1}{Fr^2}\left(\frac{\partial Fr}{\partial Hyd}\right)^2 dHyd^2} \tag{D.117}$$

$$\frac{dFr}{Fr} = \sqrt{\frac{1}{Fr^2} d(dP/dx)^2 + \frac{1}{Fr^2} dHyd^2} \tag{D.118}$$

Friction Factor:

$$f = \frac{D}{2\rho_g U_{sg}^{\ 2}} Fr \tag{D.119}$$

$$df = \left(\frac{\partial f}{\partial \rho_g}\right) d\rho_g + \left(\frac{\partial f}{\partial U_{sg}}\right) dU_{sg} + \left(\frac{\partial f}{\partial Fr}\right) dFr \tag{D.120}$$

$$\frac{df}{f} = \sqrt{\frac{1}{f^2}\left(\frac{\partial f}{\partial \rho_g}\right)^2 d\rho_g^{\ 2} + \frac{1}{f^2}\left(\frac{\partial f}{\partial U_{sg}}\right)^2 dU_{sg}^{\ 2} + \frac{1}{f^2}\left(\frac{\partial f}{\partial Fr}\right)^2 dFr^2} \tag{D.121}$$

$$\frac{1}{f^2}\left(\frac{\partial f}{\partial \rho_g}\right)^2 = \frac{4\rho_g^{\ 2} U_{sg}^{\ 4}}{D^2 Fr^2} \frac{D^2 Fr^2}{4U_{sg}^{\ 4}} = \rho_g^{\ 2} \tag{D.122}$$

$$\frac{1}{f^2}\left(\frac{\partial f}{\partial U_{sg}}\right)^2 = \frac{4\rho_g^{\ 2} U_{sg}^{\ 4}}{D^2 Fr^2} \frac{D^2 Fr^2 \rho_g^{\ 2} U_{sg}^{\ 2}}{\rho_g^{\ 4} U_{sg}^{\ 8}} = \frac{4}{U_{sg}^{\ 2}} \tag{D.123}$$

$$\frac{1}{f^2}\left(\frac{\partial f}{\partial Fr}\right)^2 = \frac{4\rho_g^{\ 2} U_{sg}^{\ 4}}{D^2 Fr^2} \frac{D^2}{4\rho_g^{\ 2} U_{sg}^{\ 4}} = \frac{1}{Fr^2} \tag{D.124}$$

Substituting Equations D.122, D.123 and D.124 into Equation D.121:

$$\frac{df}{f} = \sqrt{\rho_g{}^2\, d\rho_g{}^2 + \frac{4}{U_{sg}{}^2}\, dU_{sg}{}^2 + \frac{1}{Fr^2}\, dFr^2} \tag{D.125}$$

Drag Reduction DR:

$$DR = \left(\frac{f_{without} - f_{DRA}}{f_{without}} \right) 100 \tag{D.126}$$

$$dDR = \left(\frac{\partial DR}{\partial f_{DRA}} \right) df_{DRA} + \left(\frac{\partial DR}{\partial f_{without}} \right) df_{without} \tag{D.127}$$

$$\frac{dDR}{DR} = \sqrt{\frac{1}{DR^2}\left(\frac{\partial DR}{\partial f_{DRA}} \right)^2 df_{DRA}{}^2 + \frac{1}{DR^2}\left(\frac{\partial DR}{\partial f_{without}} \right)^2 df_{without}{}^2} \tag{D.128}$$

$$\frac{dDR}{DR} = \sqrt{\frac{df_{DRA}{}^2}{(f_{without} - f_{DRA})^2} + \frac{f_{DRA}{}^2 df_{without}{}^2}{f_{without}{}^2 (f_{without} - f_{DRA})^2}} \tag{D.129}$$

$$\frac{dDR}{DR} = \frac{1}{(f_{without} - f_{DRA})} \sqrt{df_{DRA}{}^2 + \frac{f_{DRA}{}^2}{f_{without}{}^2} df_{without}{}^2} \tag{D.130}$$